Terahertz Metasurfaces for Wave Manipulation, Detection, and Spectral Analysis

by

Sakib Quader

B. Sc. (Electrical and Electronics Engineering),
United International University, Bangladesh, 2017

M. Sc. (Electronic Science and Technology)
Shanghai Jiao Tong University, China, 2021

Thesis submitted for the degree of

Doctor of Philosophy

in

School of Electrical and Mechanical Engineering
College of Engineering and Information Technology
Adelaide University

26 March 2026

Principal Supervisor:
Prof. Withawat Withayachumnankul, Terahertz Engineering Laboratory, School of Electrical and Mechanical Engineering, Adelaide University

Co-Supervisors:
Prof. Christophe Fumeaux, School of Electrical Engineering and Computer Science, The University of Queensland

Dr. Xiaolong You, Terahertz Engineering Laboratory, School of Electrical and Mechanical Engineering, Adelaide University

© 2026
Sakib Quader
All Rights Reserved

Contents

Contents iii

Abstract vii

Statement of Impact ix

Originality Declaration xi

Acknowledgments xiii

Publications xv

List of Figures xvii

List of Tables xix

Chapter 1. Introduction 1

1.1 Introduction to the terahertz waves 3
1.2 From conventional devices to metasurfaces 9
1.3 Terahertz metasurfaces 11
1.3.1 Terahertz wave manipulation 14
1.3.2 Terahertz wave detection 16
1.3.3 Terahertz spectral analysis and spectrometer 18
1.4 Thesis outline and summary of original contributions 19

Chapter 2. Mechanically Reconfigurable Polarisation Converter 23

2.1 Introduction 25
2.2 Design 26
2.3 Fabrication and measurement 30
2.4 Results 33
2.4.1 Quarter-wave plate 33
2.4.2 Half-wave plate 36
2.5 Conclusion 40

Chapter 3. Antenna-coupled Electromechanical Bolometer 41

3.1 Introduction . . . 43

3.2 Device architecture and characterisation approach . . . 46

3.2.1 Device design and materials . . . 46

3.2.2 Numerical modelling . . . 49

3.3 Experiments and results . . . 52

3.3.1 Fabrication . . . 52

3.3.2 Terahertz response . . . 54

3.3.3 Mechanical response . . . 56

3.4 Conclusion . . . 62

Chapter 4. Compact Terahertz Spectrometer 63

4.1 Introduction . . . 65

4.2 Metasurface design . . . 67

4.2.1 Unit cell design and results . . . 69

4.2.2 Array-level design and results . . . 72

4.3 Lens design . . . 74

4.3.1 Zemax simulation and results . . . 74

4.3.2 Fabrication and measurement . . . 77

4.4 Conclusion . . . 80

Chapter 5. Terahertz Frequency Analyser 83

5.1 Introduction . . . 85

5.2 Methodology . . . 86

5.3 Experiment and results . . . 88

5.3.1 Continuous-wave measurement . . . 88

5.3.2 Training and validation using continuous-wave data . . . 90

5.3.3 Finite-bandwidth measurement . . . 93

5.3.4 Validation using finite-bandwidth data . . . 94

5.4 Conclusion . . . 97

Chapter 6. Thesis Summary 99

6.1 Thesis conclusion 101
6.2 Outlook 101
6.3 Concluding remarks 103

Appendix A. Bolometer Material Selection **105**

Appendix B. Calibration of INO MICROXCAM-384i Terahertz Camera **109**

Bibliography **111**

Abstract

The terahertz frequency spectrum offers unique features such as strong material penetration, low scattering, non-ionising behaviour, relatively high spatial resolution, and high data transmission rates. These properties confer significant prospects in numerous applications, including imaging, sensing, and high-speed wireless communications. Despite these advantages and potential, the terahertz band is still practically underutilised. This underutilisation is linked to the lack of efficient terahertz power generation and the high atmospheric attenuation in this band. Recently, significant efforts have led to advancements in terahertz power generation. However, the full utilisation of this band requires various efficient functional devices to manipulate, detect, and analyse terahertz waves. Hence, there is an urgent need to develop efficient, practical, and functional terahertz devices.

Firstly, one of the most common wave manipulation techniques, namely polarisation conversion, is explored. Multiple polarisation states of terahertz waves enable a broad range of applications and enhance system performance. The proposed mechanically reconfigurable polarisation converter can efficiently convert a linearly polarised incident wave into its orthogonal linear polarisation state or into a circularly polarised wave with simple mechanical reconfigurability. The device is designed, analysed using an equivalent circuit model, fabricated, and measured as a part of the original contribution to this thesis.

Secondly, a terahertz bolometric detector is designed for detection at the centre frequency of the WR-3.4 band (220–330 GHz), i.e., around 275 GHz. The frequency range around the WR-3.4 band is one of the most usable ranges in the whole terahertz band. However, effective room temperature bolometric detectors at this band are scarce. An antenna-coupled room temperature bolometric detector is designed by unifying a terahertz absorber, thermal transducer, and mechanical resonator into a single spiral structure to elevate the transduction efficiency. The device is designed, fabricated, and measured as a part of the original contribution to this thesis.

Thirdly, an effort to turn an incoherent terahertz camera into a spectrometer is explored. A frequency spreading metasurface based on eight distinct phase shift unit cells is designed to create frequency-dependent spatial spreading of the terahertz wave from

270 GHz to 330 GHz. The spatially spread frequency components are then focused to specific points on the camera pixels using a lens. The design of the metasurface and the lens, along with the 3D printing of the lens, is a part of the original contribution to this thesis.

Lastly, a system to analyse terahertz frequency is implemented as a part of the original contribution to this thesis. The extremely narrow channels for terahertz wireless communications require real-time and effective channel estimation techniques, especially for channel monitoring. A system incorporating a pseudo-random metasurface for high-resolution frequency discrimination paired with a machine-learning algorithm is used for instantaneous estimation of channel frequency. The device is designed, 3D-printed, measured, and the machine-learning model is trained to implement the frequency discrimination system.

Overall, this thesis showcases research efforts to efficiently manipulate, detect, and analyse terahertz waves, especially within the WR-3.4 band, through the development of compact device architectures. A systematic design workflow is used that is established on physics-based modelling, numerical simulation, fabrication, experimental measurement, and detailed result analysis to validate the claims of the proposed terahertz devices. The complex wave manipulation and processing of the devices are achieved by involving tunability, frequency diversity, and multi-physics.

Statement of Impact

The outcomes of this thesis have important implications in terahertz wireless communications, detection, and imaging. In communications, the reconfigurable polarisation converter provides adaptive polarisation control, improving channel conditions such as link reliability and robustness, and enabling multiplexing for channel capacity enhancement, while promoting flexibility through reconfigurable performance. The pseudo-random metasurface system for frequency analysis enables real-time spectrum monitoring and channel identification as a compact and passive device to complement coherent front-end receivers, where conventional frequency analysers are difficult to implement. In detection, the spiral bolometer provides a viable pathway toward efficient terahertz detection at room-temperature with high responsivity via antenna-coupled monolithic design. In imaging, the frequency-spreading metasurface combined with a 3D-printed focusing lens enables a portable add-on that can be installed with a terahertz camera to effectively transform it into a compact spectrometer or combined spectral characterisation and imaging.

Originality Declaration

I certify that this work contains no material which has been accepted for the award of any other degree or diploma in my name, in any university or other tertiary institution and, to the best of my knowledge and belief, contains no material previously published or written by another person, except where due reference has been made in the text. In addition, I certify that no part of this work will, in the future, be used in a submission in my name, for any other degree or diploma in any university or other tertiary institution without the prior approval of Adelaide University and where applicable, any partner institution responsible for the joint award of this degree. The author acknowledges that copyright of published works contained within the thesis resides with the copyright holder(s) of those works.

I give permission for the digital version of my thesis to be made available online via the University's digital research repository, the Library Search and also through web search engines, unless permission has been granted by the University to restrict access for a period of time.

This research was supported by an Australian Government Research Training Program (RTP) Scholarship DOI: 10.82133/C42F-K220.

Sakib Quader

Signed

26/03/2026

Date

In this work, ChatGPT was used solely for grammar checking and minor language refinement during the preparation of this thesis. All technical content, analysis, and conclusions were produced by the author.

Acknowledgments

The completion of this thesis was made possible by the support and guidance of my supervisors, colleagues, family, and friends, to whom I am deeply grateful. I extend my sincere thanks to Prof. Withawat Withayachumnankul, Prof. Christophe Fumeaux, and Dr. Xiaolong You for their invaluable guidance and support throughout my doctoral candidature.

My principal supervisor, Prof. Withawat Withayachumnankul, has guided me consistently since my PhD scholarship application in 2021. He has been an exceptionally supportive and dedicated mentor. His intellectual leadership, technical insight, constant encouragement, and extensive expertise in terahertz technology shaped not only this research but also my growth as a researcher throughout my PhD journey. I have always admired his remarkable attention to detail and ability to identify even subtle inconsistencies, which significantly improved the clarity and logical depth of my work. Dear Withawat, I am truly grateful for your mentorship, and unwavering support. I sincerely cherish every moment of this journey working under your mentorship. Your kindness, generosity, and sincere care for your students are qualities I will always remember and deeply appreciate.

To my co-supervisor, Prof. Christophe Fumeaux, you have been a constant source of inspiration throughout my PhD journey. Your profound expertise in electromagnetics and research insight significantly shaped many aspects of my research and strengthened both the theoretical depth and the practical direction of my work. I always valued our weekly meetings, which were intellectually stimulating and highly productive. I sincerely appreciate your dedication to reviewing my manuscripts with great care despite your demanding schedule. Your commitment, professionalism, and genuine support have left a lasting impact on my academic growth.

To Dr. Xiaolong You, thank you for your valuable insights into measurement setups and for the many insightful discussions on metasurfaces and simulation techniques. Your willingness to share research files and technical knowledge greatly supported my progress. You have been more than a co-supervisor to me; you have been both a mentor and a friend, and I deeply appreciate your support and encouragement.

I gratefully acknowledge the Terahertz Engineering Laboratory at Adelaide University for providing a supportive and collaborative research environment. I sincerely thank my colleagues, Dr. Daniel Headland, Dr. Mingxiang (Stephen) Li, Ms. Linxi Chen, Ms. Mariam Abdullah, Mr. Miantong Sun, Mr. Chung Yin Tam, Ms. Komal Iqbal, Mr. Amit Haldar, Mr. Junwei Liang, Ms. Nontiwat Amnuayphol, Mr. Adib Mohammed, and Mr. Taegyun Noh for their technical assistance and valuable discussions. Special thanks to Dr. Panisa Dechwechprasit for laboratory inductions, and to Dr. Harrison Lees and Mr. Bryce Chung for their assistance with measurement setups and troubleshooting.

My sincere thanks go to Prof. Sharath Sriram, Dr. Rajour Tanyi Ako, and Prof. Madhu Bhaskaran from the Functional Materials and Microsystems Research Group and the Micro-Nano Research Facility at RMIT University, Melbourne, for their support in metasurface fabrication. I also acknowledge the Australian National Fabrication Facility - South Australian (ANFF-SA) and OptoFab nodes for their fabrication support. At Adelaide University, I thank Mr. Danny Di Giacomo and Mr. Brandon Pullen for their technical support. I also sincerely appreciate the Acoustics and Vibration Laboratory, Adelaide University, particularly Dr. Benjamin Cazzolato and Dr. Tingyuan Yin, for providing access to the laser Doppler vibrometer, with special thanks to Dr. Tingyuan Yin for her guidance and troubleshooting support during measurements.

I gratefully acknowledge the financial support provided by the Adelaide University Research Scholarship, which made my PhD studies possible. I am also sincerely thankful to the School of Electrical and Mechanical Engineering for supporting my participation in international conferences. In addition, I acknowledge the support of the IEEE Antennas and Propagation Society through the 2024 IEEE AP-S Research Fellowship Award.

Finally, I extend my sincere gratitude to my close friends Dr. A. B. Siddik and Mr. M. Hossain for their encouragement and moral support. Above all, I offer my deepest and most heartfelt appreciation to my family for their unconditional love and constant belief in me. To my mother, Razia, and my late father, Sohail, whose values and sacrifices continue to inspire me everyday, this achievement is deeply rooted in everything you taught me. To my elder sister, Sumayra, my younger sister, Fatima, my brother-in-law, Mojahid, and my beloved nephew, Ahmad, thank you for your love and encouragement during the most demanding moments of my journey.

Publications

Journals

QUADER-S., FUMEAUX-C., AND WITHAYACHUMNANKUL-W. (2026). Antenna-coupled terahertz electromechanical bolometer, *APL Engineering Physics*, **1**(1), art. no. 016104. (**Invited, Featured**)

QUADER-S., ABDULLAH-M., HE-E., FUMEAUX-C., AND WITHAYACHUMNANKUL-W. (2025). 3D-printed frequency-diverse metasurface for camera-based terahertz frequency analyzer, *IEEE Microwave and Wireless Technology Letters*, **35**(12), pp. 2105–2108. (**Selected by the committee for Special Issue on Asia-Pacific Microwave Conference 2025**)

QUADER-S., AKO-R. T., SRIRAM-S., FUMEAUX-C., AND WITHAYACHUMNANKUL-W. (2024). Mechanically reconfigurable polarization converter for terahertz waves, *IEEE Transactions on Terahertz Science and Technology*, **14**(4), pp. 502–509.

Conferences

QUADER-S., LV-X., YOU-X., AKO-R. T., BHASKARAN-M., SRIRAM-S., FUMEAUX-C., AND WITHAYACHUMNANKUL-W. (2024). Mechanically reconfigurable terahertz quasi-optical components for spectral filtering and polarization control, *IEEE Microwaves, Antennas and Propagation Conference (MAPCON)*, Hyderabad, India, pp. 1–4. (**Invited**)

QUADER-S., FUMEAUX-C., AND WITHAYACHUMNANKUL-W. (2024). Antenna-coupled micro-electromechanical bolometer for terahertz detection, *IEEE Asia-Pacific Microwave Conference (APMC)*, Bali, Indonesia, pp. 802–804.

List of Figures

1.1 Electromagnetic spectrum . . . 3
1.2 Fibre-coupled THz-TDS system (TERA K15) from Menlo Systems . . . 6
1.3 Frequency dependent atmospheric attenuation of terahertz waves . . . 8
1.4 Examples of exceptional electromagnetic responses enabled by metamaterial unit cell design . . . 10
1.5 Equivalent circuit interpretation of metasurface unit cell geometries . . . 13

2.1 Metasurface structure . . . 27
2.2 Circuit representation of metallic layers . . . 28
2.3 Circuit representation at 0 µm separation . . . 29
2.4 Circuit representation at 150 µm separation . . . 29
2.5 Metasurface sample and setup . . . 31
2.6 Quarter-wave plate simulated and measured transmission . . . 34
2.7 Quarter-wave plate performance . . . 35
2.8 Angular stability of the quarter-wave plate under oblique incidence . . . 36
2.9 Half-wave plate simulated and measured transmission . . . 37
2.10 Half-wave plate performance . . . 38
2.11 Angular stability of the half-wave plate under oblique incidence . . . 39

3.1 MEMS bolometer device layout . . . 48
3.2 Electromagnetic simulation results . . . 50
3.3 Simulated vibrational mode . . . 50
3.4 Thermomechanical simulation results . . . 51
3.5 Device structure and integration . . . 53
3.6 Electromagnetic measurement setup and response . . . 55
3.7 Mechanical measurement setup and response . . . 57

4.1 Spectrometer architectures 67
4.2 Phase gradient beam deflection 68
4.3 Unit cell design architecture 70
4.4 Unit cell transmission 71
4.5 Metasurface design and response 73
4.6 Focusing lens design and response 76
4.7 Lens design and characterisation 79

5.1 Design of the pseudo-random metasurface 87
5.2 Experimental setup and representative wave patterns 89
5.3 Metasurface and CNN performance 91
5.4 Representative pattern images under continuous wave 93
5.5 Finite-bandwidth measurement concept 94
5.6 Accuracy under finite-bandwidth wave 95
5.7 Representative pattern images under 2 GHz bandwidth signals 96

B.1 Terahertz camera calibration 110

List of Tables

2.1 Performance comparison of transmissive terahertz quarter-wave plates . 36

2.2 Performance comparison of transmissive terahertz half-wave plates . . . 40

3.1 Performance comparison of terahertz room temperature bolometers . . . 61

A.1 Comparison of candidate absorber materials 106

Chapter 1

Introduction

THE terahertz band lies between two of the more technologically mature frequency regions of the electromagnetic spectrum, the microwave and infrared. This frequency spectrum holds immense application prospects, yet is relatively untapped. Although substantial progress in semiconductor research has enabled effective generation of terahertz waves, their widespread application is still trailing due to the lack of efficient terahertz devices. At the terahertz regime, most natural materials and conventional methods pose several limitations. As an alternative, engineered sub-wavelength structures called metasurfaces are found to be more effective. This introductory chapter begins with a brief definition of the terahertz region along with its benefits, drawbacks, and potential applications. This chapter also introduces metasurfaces and discusses their design and working principle. Later, terahertz metasurfaces are discussed, especially for terahertz wave manipulation, detection, and analysis, providing a motivation behind this research. Finally, this chapter concludes by outlining the structure of the thesis and summarising the original contributions.

1.1 Introduction to the terahertz waves

For decades, terahertz waves ranging from 0.1 to 10 THz have remained underutilised despite their many advantages and application prospects (Abbott and Zhang, 2007; Siegel, 2002). This electromagnetic spectrum is situated between two of the more widely explored frequency ranges, as shown in Figure 1.1. The lower bound frequencies, close to microwaves, partially coincide with the millimetre waves (30 to 300 GHz) and cover the whole sub-millimetre wave band (0.3 to 3 THz) (Wiltse, 1984). The terahertz band inherits some properties from microwaves, allowing it to penetrate dry non-metallic materials, while exhibiting relatively low photon energy, thereby precluding ionisation. These properties make this frequency range viable for non-destructive evaluation (NDE) applications, for instance material characterisation (Naftaly and Miles, 2007), and biomedical sensing (Pickwell and Wallace, 2006). The other end of the terahertz range overlaps with the far infrared, which stretches from 3 to 20 THz (Vatansever and Hamblin, 2012), passing down some unique features to the terahertz spectral range, conveying rich spectral fingerprints with high spatial resolution compared to microwaves. Uniquely so, terahertz waves combine microwave-like strong penetration with infrared spectroscopic precision and sensitivity to molecular resonances, paving the way for unprecedented imaging and sensing systems to characterise materials with depth information along with structural, molecular, and chemical signatures (Mittleman, 2018).

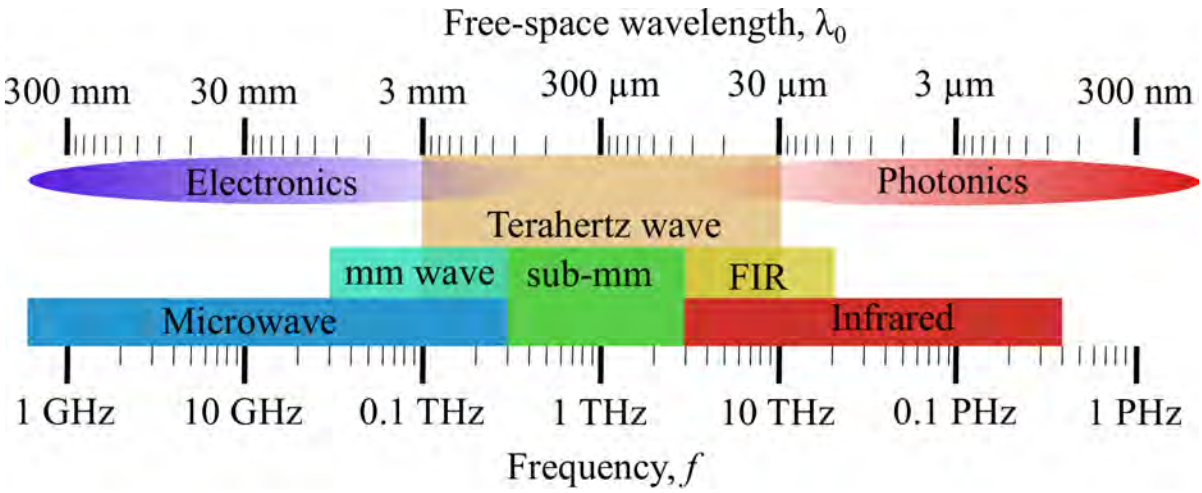

Figure 1.1. Electromagnetic spectrum. The terahertz frequency range within the electromagnetic spectrum, situated between the microwave and infrared waves and overlapping with the millimetre wave, sub-millimetre wave and far-infrared region. The figure highlights the gradual fading of electronic and photonic generation techniques in the terahertz regime.

Additionally, the extremely large available bandwidth at these frequencies enable ultra-high data rates, placing terahertz waves at the forefront of next-generation high-speed wireless communications systems (Nagatsuma *et al.*, 2016).

In recent years, the rising demand for data capacity in the microwave and millimetre wave bands has resulted in spectral clogging (Cisco, 2017; Nagatsuma *et al.*, 2016). This spectral congestion has created demand for higher frequency bands such as terahertz, as they hold capabilities to host ultra-fast communications as well as advanced imaging, and sensing applications (Withayachumnankul, 2010; Lee, 2018). However, utilising the terahertz region has been challenged by the lack of efficient methods to generate and detect adequate terahertz power. Although terahertz waves span the microwave–infrared boundary and lie between electronic and photonic sources, most conventional sources from both sides broadly fall short of generating sufficient terahertz power. The electronics-based generation techniques are used mainly at lower frequencies, especially microwaves and millimetre waves, and usually undergo progressive attenuation of output power with increasing frequency. The power roll-off becomes substantially high at moderate terahertz frequencies, preventing the generation of usable power (Eisele and Haddad, 1998; Sedra *et al.*, 1998). On the other end of the terahertz frequencies, the infrared waves rely on optical generation techniques, especially using lasers as power sources. However, optical approaches are limited because low terahertz photon energy and thermal excitations prevent efficient stimulated emission and suppress gain, thereby limiting practical terahertz output power (Williams, 2007). These inherent power bottlenecks from both generation techniques limit the achievement of sufficient power for practical applications at terahertz frequencies. This has significantly resulted in the persistent underutilisation of this spectral region, thereby leading to the band being designated as the 'terahertz gap'.

Despite the lack of sufficient generation power, terahertz waves have still been one of the most promising candidates to mitigate the spectral congestion of the microwave and millimetre wave regime. The immense potential benefits of this band, such as ultra-fast wireless communications, cutting-edge imaging and sensing applications have motivated much research over the recent decades to properly utilise the spectrum. Significant efforts to progressively narrow down the terahertz gap by improving terahertz generation techniques and achieving sufficient power have been concentrated on both the electronic and photonic generation domains. On the electronics front, the evolution in semiconductor materials and oscillator architecture has significantly increased the

output power experienced at higher frequencies. High-mobility transistors benefitting from the emergence of modern semiconductor platforms such as indium phosphite (InP), silicon germanium (SiGe), and advanced silicon push the achievable cut-off frequencies to higher values (Arabhavi *et al.*, 2022; Mei *et al.*, 2015). Concurrently, nanoscale gate lengths combined with ultrathin substrates have effectively helped to trim down the parasitic reactance at terahertz frequencies (Božanić and Sinha, 2019). Beyond these transistor-based solutions, advanced semiconductor materials have allowed diode-based oscillators such as Gunn diodes (Khalid *et al.*, 2014), impact ionisation avalanche transit-time (IMPATT) diodes (Bychok *et al.*, 2024), and resonant tunnelling diodes (RTD) (Asada and Suzuki, 2021) to leverage negative differential conductance to maintain oscillation frequencies close to 1.5 THz. Furthermore, reductions in conduction loss have enabled RTD-based oscillators to reach frequencies up to 1.92 THz (Maekawa *et al.*, 2016). Harmonic-multiplier chains built upon Schottky diodes add further tunability via harmonic up-conversion. Collectively, these innovations have served to address the long-standing terahertz generation barrier from the electronic side to operate effectively in the terahertz band.

On the other hand, constant effort towards photonic terahertz generation is concentrated on entirely bypassing stimulated emission. Advances in ultrafast optics, semiconductor materials, and nanofabrication have enabled high-performance femtosecond lasers, photoconductive antennas, nonlinear crystals, and photomixing techniques to generate terahertz waves through transient currents or nonlinear optical mixing (Burford and El-Shenawee, 2017; Ishibashi and Ito, 2021). This bypasses the need for population inversion, facilitating both pulsed and continuous terahertz generation. Moreover, hybrid methods that overcome limitations of both purely electronic up-scaling and terahertz lasing combine optical excitation with rapid electronic currents for effective terahertz generation. Quantum-cascade laser (QCL) uses a purely photonic terahertz generation technique by relying on stimulated emission as well as reducing the thermal load with engineered quantum wells and cryogenic cooling. Together, these combined methods have expanded access to the terahertz band for practical applications.

More recently, the use of modern photoconductive antennas driven by infrared femtosecond laser pulses has enabled terahertz time domain spectroscopy (THz-TDS) systems to generate and detect terahertz pulses. A typical implementation of such a system is the commercially available fibre-coupled TERA-K15 spectrometer by Menlo Systems, shown in Figure 1.2, which integrates a femtosecond laser, an optical delay line, and

Figure 1.2. Fibre-coupled THz-TDS system (TERA K15) from Menlo Systems. Photograph of the TERA K15, terahertz time-domain spectroscopy system manufactured by Menlo Systems. The systems integrates a femtosecond laser, an optical delay line, and terahertz emitter and detector units. Adopted from Menlo Systems (2020).

terahertz emitter and detector units. The Fourier transform of the full time-domain waveform captured by the THz-TDS system gives both magnitude and phase, enabling quantitative spectroscopy and material characterisation. This capability substantially overcomes the intensity-only detection techniques and underpins the use of THz-TDS in spectroscopy, material characterisation, sensing, and imaging.

Overcoming the limitations of generation and detection has unlocked terahertz technology for use in various applications. One such application is material characterisation (Naftaly and Miles, 2007; Scheller, 2011), as many substances, including crystalline materials, water, explosives, and many proteins and drugs, exhibit unique spectral characteristics in the terahertz spectrum. These unique spectral features at terahertz waves allow them to be applied for object identification (Shen *et al.*, 2005; Miles *et al.*, 2007), investigation of materials with chemical (Fischer *et al.*, 2005; Yakovlev *et al.*, 2015), and biological (George and Markelz, 2013; Yang *et al.*, 2016) signatures. Additionally, their sensitivity to humidity makes them applicable to probe water content in samples (Banerjee *et al.*, 2008; Shin *et al.*, 2017; Fan *et al.*, 2019), and even in biological tissues.

Moreover, with the capability of probing water content in biological tissues, the non-ionising characteristics of terahertz waves make them a non-destructive option for

medical (Cheon *et al.*, 2017; Hernandez-Cardoso *et al.*, 2017; Zhao *et al.*, 2018), and biological imaging (Yun *et al.*, 2017; Shi *et al.*, 2018; Wu *et al.*, 2020). Although the high water absorption of terahertz waves limits penetration depth and can obscure other biological signatures, it also provides useful contrast for imaging hydration-related features in tissues. Imaging applications are also supported by the improved imaging resolution compared to microwaves and millimetre waves, and the penetrability of terahertz waves through optically opaque objects. Terahertz waves can penetrate through dry and non-metallic materials, providing potential for non-destructive imaging of priceless artefacts and arts, and security screening to reveal hidden objects (Tzydynzhapov *et al.*, 2020; Cheng *et al.*, 2020).

A big leap in the application of terahertz waves is the potential for ultrafast data rate wireless communications. With the exponentially increasing data traffic, and to cope with the rising number of highly demanding applications such as virtual reality, augmented and mixed reality, terahertz waves with their fast data transfer and extremely large unused bandwidth is expected to become a vital part to mitigate the challenges. This frequency spectrum holds high potential for the development of future communications networks, owing to its capability to support theoretical transmission speed up to 1 Tb/s (Koenig *et al.*, 2013). A Few notable experimental studies conducted experiments at carrier frequencies up to 0.4 THz, demonstrating reliable transmission with data rates around several tens of Gbps (Nagatsuma *et al.*, 2009; Song *et al.*, 2012; Koenig *et al.*, 2013; Song *et al.*, 2014; Nagatsuma *et al.*, 2016). Experimentally achieving the theoretical speed limit is highly challenging due to various limitations of terahertz waves, such as high free-space path loss, strong atmospheric absorption, limited source power, receiver noise, and stringent beam-alignment requirements. These factors reduce the achievable signal-to-noise ratio and therefore the attainable data rate.

Advances in terahertz power generation and efficient detection overcome two of the major limitations of terahertz systems and make the band accessible for practical applications. However, the band intrinsically suffers from extreme atmospheric attenuation as illustrated in Figure 1.3. This strong atmospheric attenuation is mainly caused by the water-vapour absorption, which exhibits strong resonance across the terahertz spectrum and consequently limits the achievable transmission distance. As illustrated in Figure 1.3, the frequency-dependent atmospheric attenuation triggers a series of transmission windows between attenuation spikes, which experience relatively minimal

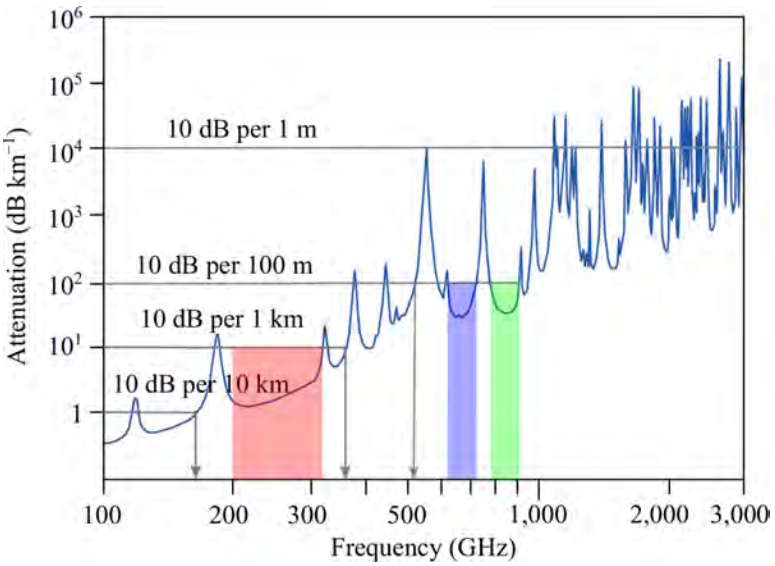

Figure 1.3. Frequency dependent atmospheric attenuation of terahertz waves. Attenuation of terahertz waves from 0.1 to 3 THz due to absorption by water-vapour in the atmosphere. Several resonance peaks disrupts the whole band, with 200–330 GHz (red) applicable for transmission over several kilometres, and 625–725 GHz (blue) and 780–910 GHz (green) optimal for indoor transmission. Adopted from Nagatsuma *et al.* (2016).

loss. For instance, the 200–330 GHz band supports short-range transmission over distances up to several kilometres, whereas higher-frequency windows beyond 600 GHz, specifically the 625–725 GHz and 780–910 GHz bands are optimal for indoor communications (Nagatsuma *et al.*, 2016). Transmission windows over 1 THz experience high atmospheric attenuation such that they are only limited to near field communications, typically around distances close to 1 metre. Among these available windows, the 200–330 GHz band is of particular interest as it supports short-range high-speed wireless communications while simultaneously allowing high-resolution sensing and imaging. Indeed, the IEEE has allocated the 252–325 GHz band for switched point-to-point high-data-rate wireless communications, as reported by the IEEE 802.15.3d (IEEE 802 LAN/MAN Standards Committee, 2017) standard and later extended this allocation to 252–450 GHz in the amended IEEE 802.15.3–2023 standard (IEEE 802 LAN/MAN Standards Committee, 2024).

The immense bandwidth of terahertz waves is accessible via distinct transmission windows with different propagation and absorption characteristics, allowing multiple applications. Accessing the applications requires various functional devices to generate, manipulate, detect, and analyse terahertz signals. Efficient terahertz devices are still

trailing the demand in many practical applications, since most natural materials exhibit a weak response to terahertz waves (Yen *et al.*, 2004; Chen *et al.*, 2006). Artificially engineered materials called metamaterials can essentially respond well enough to terahertz waves to be prominently used as terahertz devices for a plethora of applications.

1.2 From conventional devices to metasurfaces

Enhancing the various applications of electromagnetic waves in wireless communications, sensing, and imaging relies heavily on manipulating waves. Conventionally, electromagnetic waves are manipulated using bulk optical components such as dielectric lenses, prisms, beam splitters, and birefringent waveplates. These optical devices utilise classical physical principles, such as reflection and refraction of electromagnetic waves, along with phase accumulation during propagation of a wave through materials with a specific refractive index. As the wave passes through a medium, the material's refractive index introduces a phase delay in the wave's electric field components. Controlling phase and amplitude by manipulating electromagnetic waves enables various functionalities, including polarisation control, beam steering, focusing, and various other beamforming functionalities. For instance, materials exhibiting birefringence function as a waveplate by introducing controlled phase differences between orthogonal field components. Waveplates allow polarisation conversion through controlled phase differences. Achieving a specific phase difference by a birefringent material is strongly dependent on its physical thickness.

Although such conventional devices can effectively manipulate a large portion of electromagnetic waves, they encounter multiple constraints to function efficiently in the terahertz region. As these devices are strongly dependent on material thickness and require it to be comparable to the wavelength, at the terahertz range, these bulk optical elements become physically large and mechanically heavy. Thick materials increase absorption and reflection and require long propagation distances, making compact terahertz designs difficult and less efficient. Additionally, the need for precise thickness for specific functions like polarisation control using waveplates essentially narrows down the operation bandwidth and typically results in a modest extinction ratio or high insertion loss. Similarly, it is challenging to control the bandwidth of filters, especially those based on metal meshes and multilayer dielectrics, as improving bandwidth requires multi-layer stacking, which further increases weight, alignment complexity,

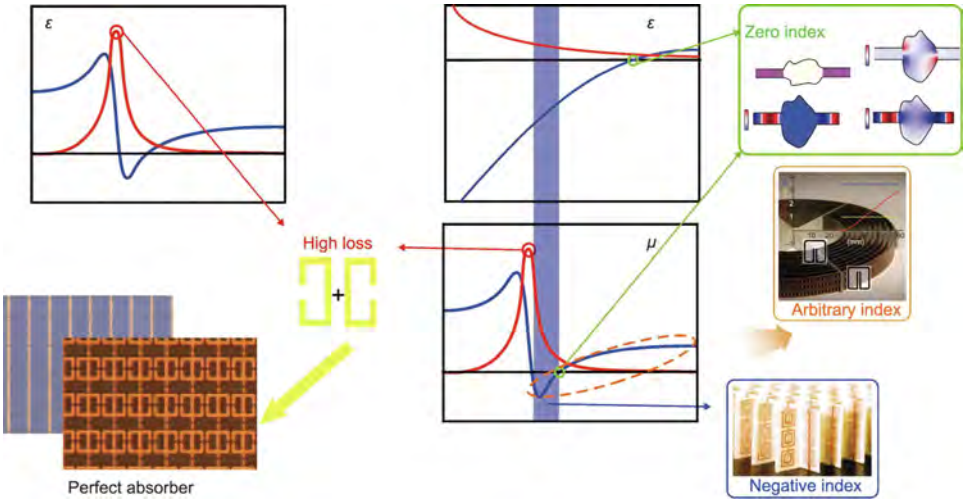

Figure 1.4. Examples of exceptional electromagnetic responses enabled by metamaterial unit cell design. Some widely implemented unit cell structures enabling various refractive index values achieved through metamaterial design, exhibiting exquisite phenomenon, such as negative indexes (Shelby *et al.*, 2001), zero-index materials (Mahmoud and Engheta, 2014), metamaterial perfect absorbers (Tao *et al.*, 2008), and the invisibility cloak (Schurig *et al.*, 2006). ε: permittivity; μ: permeability. Adopted from Sun and Zhou (2025).

and fabrication challenges. All these factors combined make it difficult to design lightweight, miniaturised, and multifunctional terahertz devices solely with traditional components. Thus, there is an urgent need to replace the traditional components with low-profile, lightweight devices that offer similar functionalities.

The quest for more effective and efficient devices to provide versatile control over electromagnetic waves has led to the development of metamaterials. Metamaterials are artificial sub-wavelength structures, for example, split-rings (Pendry *et al.*, 1999), metal wires (Pendry *et al.*, 1998), that are designed to exhibit unprecedented control over electromagnetic response. Figure 1.4 shows some examples of widely implemented unit cell structures and their corresponding electromagnetic response. They often exhibit exquisite phenomena such as negative permittivity (Pendry *et al.*, 1998), negative magnetic permeability (Pendry *et al.*, 1999), negative refraction (Smith and Kroll, 2000; Shelby *et al.*, 2001), electromagnetic cloaking (Schurig *et al.*, 2006) and much more. The emergence of metamaterials has quickly filled the void for high-performance devices in the terahertz frequencies, where most natural materials fail to deliver strong or tunable responses (Yen *et al.*, 2004; Chen *et al.*, 2006). Although metamaterials support much stronger control over electromagnetic waves than conventional materials,

they often suffer from significant dissipation losses due to their reliance on resonant mechanisms and the use of lossy metallic constituents. Such losses can be reduced through the use of all-dielectric metamaterials employing low-loss terahertz dielectric materials. However, similar to conventional devices, metamaterials are typically realised as multi-layered three-dimensional structures, which increases fabrication complexity, particularly at terahertz frequencies where precise alignment and micro-/nano-scale geometry control are required. Furthermore, their volumetric architecture complicates the integration of active tuning mechanisms and control circuitry. To address these limitations in bulkiness, fabrication complexity, and integration, metasurfaces have emerged as the two-dimensional counterpart of metamaterials, providing comparable wavefront manipulation capabilities while significantly reducing structural thickness and fabrication complexity (Zheludev and Kivshar, 2012). Metasurfaces are structures comprised of arrays of periodically arranged sub-wavelength scatterers on a planar substrate, making them ultrathin and lightweight. This arrangement of sub-wavelength scatterers supports metasurfaces to interact locally with the incident wavefront as a result, even a single-layer pattern can impart rapid changes to the phase, amplitude, polarisation, and spectral content of the impinged electromagnetic wave (Quader *et al.*, 2020a). This, in turn, supports complex spatial conversions while drastically lowering thickness and losses compared to conventional metamaterials. The single-layer ultrathin geometry simplifies fabrication via standard lithographic methods and complements coherent interfacing with current terahertz systems.

1.3 Terahertz metasurfaces

Metasurfaces provide a compelling alternative to replicate and, in most cases, surpass the functionalities achieved by traditional terahertz optics while actively addressing many inherent limitations of such bulky components. For instance, flat metalenses (Liu *et al.*, 2025), and polarisation converters (Nouman *et al.*, 2016) based on a metasurface are orders of magnitude thinner than their traditional counterparts, while being much more efficient. Moreover, metasurfaces offer multifunctionality and reconfigurability, allowing a single patterned layer to simultaneously offer various or switchable functionalities, including wavefront shaping, polarisation control, and spectral filtering, while reducing system complexity (Saifullah *et al.*, 2022). These unique capabilities make metasurfaces highly attractive for terahertz imaging (Tzydynzhapov *et al.*, 2020), sensing (Singh *et al.*, 2014), detection (Vicarelli *et al.*, 2022), and

communications systems (Li *et al.*, 2021), where size, weight, efficiency, and integration are critical.

A key reason behind the high suitability of metasurfaces to interact strongly with terahertz waves lies in the wavelength scale of this band. Terahertz wavelengths are in the proximity of a few hundred micrometres to several millimetres. Metasurface unit cells, being sub-wavelength structures, are generally in the order of tens to hundreds of micrometres. This range of dimensions can be fabricated with high precision using established methods, unlike optical metasurfaces that constantly challenge the nanofabrication limit.

Moreover, a few other factors strengthen the utilisation of metasurfaces in this band, for instance, material consideration. At terahertz frequencies, most metals, including gold, aluminium, and niobium act as good conductors, thereby minimising ohmic losses as compared to the optical spectrum. Therefore, metallic metasurfaces at this band yield high efficiency. On the contrary, the dielectric loss undertakes the major share of loss, yet is controllable owing to a few low-loss dielectric materials at terahertz, such as cyclic olefin copolymer (COC), high resistivity silicon, and quartz, thereby confining overall loss.

All these significantly complement the broad range of application prospects of terahertz metasurfaces. In terahertz imaging, metasurfaces can be used to shape and focus beams, improve resolution, or implement compact scanning-free imaging architectures. In spectroscopy and sensing, metasurfaces enable strong field confinement and frequency-selective responses, enhancing interaction with materials and improving sensitivity. In communications, metasurfaces support beam steering, wavefront shaping, and polarisation control that are necessary for high-capacity and directional terahertz links. More recently, frequency-dispersive and frequency-diverse metasurfaces have opened innovative routes for compact spectrometers and computational imaging systems, where the inherent dispersion of the metasurface becomes a functional advantage rather than a limitation. Additionally, for detection, a terahertz metasurface can be designed to be sensitive to incident power, thereby allowing terahertz detection.

At the physical level, the unit cells in a terahertz metasurface function as infinitesimal antennas for terahertz waves. In a metallic metasurface supported by a dielectric substrate, the unbound electrons in metals oscillate, whereas the bound charges in dielectrics undergo minimal deviations. This movement occurs at terahertz speed while imitating the rhythm of impinging waves. These unit cells each contain a sub-wavelength metallic

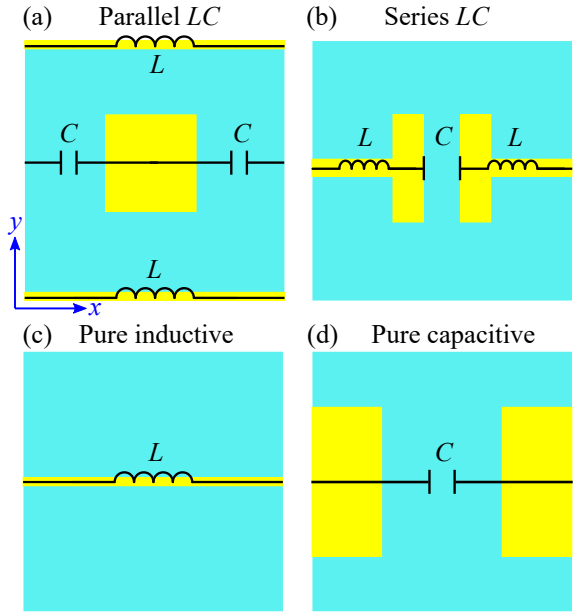

Figure 1.5. Equivalent circuit interpretation of metasurface unit cell geometries. Representative metallic patterns and their corresponding equivalent circuit interpretations under x-polarised incidence. a) Parallel LC, (b) series LC, (c) predominantly inductive, and (d) predominantly capacitive responses. The effective inductance is primarily governed by the current path length, and effective capacitance is determined by gaps or closely spaced conductors. Such equivalent circuit representations provide physical insight into the resonant behaviour of metasurfaces and enable prediction of resonance arising from inductive and capacitive reactance. Adopted from You *et al.* (2022).

geometric pattern, which, due to its size, strongly keeps the charge motion confined to the patterns. Charge also accumulates at gaps, corners, or discontinuities and localises the electric field. Altogether, these circulating currents and charge accumulation form electric and magnetic dipoles. These dipoles reradiate the field and produce induced electromagnetic waves by combining with the incident wave. The shape, size, and orientation of the unit cells usually define the electromagnetic response of the metasurface by controlling the transmission, reflection, and phase of the wave, thereby activating manipulation, detection, sensing, and analysing the terahertz waves (Cheng *et al.*, 2024).

The geometry of the unit cell largely defines the response of the metasurface due to it being a resonant structure. The response of the metasurface based on geometry can be explained by an equivalent circuit model. In general, the current path length closely corresponds to the effective inductance, and the gaps or closely spaced conductors are defined by the effective capacitance, as shown in Figure 1.5. This allows to predict the occurrence of resonance through inductive and capacitive reactance balance using the

equivalent circuit model of a given unit cell geometry. At resonance, the interaction between the unit cell and the impinging terahertz wave is strongly coupled by maximising induced currents and local fields. This resonant enhancement is achieved even with ultrathin metasurfaces and allows for a strong response in the terahertz region.

This interaction mechanism is also dependent on boundary conditions. The behaviour of tangential electric and magnetic fields at the interface can be determined from the spatially varying surface impedance supported by the metasurface. The unit cell geometry governs the local surface impedance, and by tailoring it, the reflection, transmission, and phase response of the metasurface can be controlled. Accordingly, metasurfaces can operate in either reflective or transmissive configurations, depending on whether the incident wave is primarily reflected or transmitted through the structure. Thus, each unit cell functions as a localised impedance element that collectively forms a spatially engineered electromagnetic boundary.

Lastly and importantly, when placed in an array, each unit cell interacts with its neighbouring unit cells through near-field or surface wave coupling. This mutual interaction modifies the effective response from that of a single element and can add up to the collective performance of a metasurface. This mutual coupling can be significant, including in the terahertz regime, due to the unit cell spacing being smaller compared to the wavelength, and so needs to be considered while designing a metasurface.

In summary, terahertz metasurface unit cells interact with terahertz waves by transforming incident fields into localised current and charge oscillations, which induce a modified electromagnetic field. This strong wave manipulation within a sub-wavelength thickness is caused by resonance, surface impedance control, and mutual coupling. These physical mechanisms are the reason behind efficient control over terahertz waves through carefully designing unit cells, despite them being planar structures. Such metasurfaces hold strong prospects for use in manipulation, detection, sensing, and analysis of terahertz waves, which will be explored in this thesis.

1.3.1 Terahertz wave manipulation

Most terahertz systems extending across imaging, sensing, and wireless communications fundamentally demand efficient manipulation of terahertz waves. These manipulations enable control over phase, amplitude, and polarisation of terahertz radiation to facilitate functionalities such as beam shaping (Li *et al.*, 2021; Zhang *et al.*, 2025b;

Stephen Li *et al.*, 2023), beam steering (Shiri *et al.*, 2023; Fu *et al.*, 2020), wave modulation (Degl'Innocenti *et al.*, 2022; Rahm *et al.*, 2013), and polarisation conversion (You *et al.*, 2021, 2020; Quader *et al.*, 2020b). All these capabilities explicitly facilitate the transmission, probing, and detection of terahertz energy. Such wave manipulations strongly complement many applications, for instance, in terahertz imaging systems, precise control over phase and amplitude is essential to focus terahertz beams onto a target and to tailor illumination profiles that improve spatial resolution and signal-to-noise ratio. In communications systems, beam steering and phase modulation are useful for directional links, spatial multiplexing, and suppressing interference, along with polarisation control to provide enhanced degrees of freedom for channel capacity and robustness.

With time, metasurfaces have evolved to act as an impactful medium to manipulate terahertz waves, enabling the adequate leveraging of these degrees of freedom through planar, compact structures. Metasurface-based polarisation converters have shown efficient conversion from one polarisation state to another using anisotropic or chiral unit cells that enable orthogonal resonant modes. Such devices capitalise on the significant coupling between the terahertz field and resonant currents to initiate controlled phase delays between orthogonal polarisation components, as a result, attaining ultrathin waveplates to substitute bulky birefringent devices.

Likewise, a widely used flat alternative to conventional terahertz lenses is metasurface-based focusing lenses (You *et al.*, 2025; Wang *et al.*, 2015b), and beam deflectors (Hong *et al.*, 2019; Su *et al.*, 2015). These ultrathin devices utilise a spatially varying phase profile across the metasurface to focus the terahertz beam to a specific focal point or steer it at a defined angle, resulting from generalised refraction principles. These metasurface lenses are comparatively much thinner, lighter, and easier to integrate into compact systems than traditional components, making them crucial for portable on-chip terahertz platforms. Beam deflectors based on phase gradients have also been employed in designing compact scanners and beam steering devices without mechanical tuning.

Tunable and reconfigurable wave manipulation functions in the terahertz domain are highly sought after and are strongly supported by metasurfaces (Xu *et al.*, 2022; Saifullah *et al.*, 2022; Li *et al.*, 2024a). Tunable metasurfaces allow an adjustable response from a single device. This tuning can be achieved by several means, such as mechanical (Pan *et al.*, 2025), thermal/optical (Ko *et al.*, 2022), or electrical tunability (Quader *et al.*,

2020b,a). Mechanical tunability utilises physical reconfiguration of the geometry, spacing, or orientation of the device to controllably shape the electromagnetic response. This usually provides large tuning ranges, however at the cost of increased complexity and slower response times. Optical/thermal tunability often requires unit cells to be based on phase-change materials or temperature-dependent conductivity to vary the state of the material depending on temperature. They are relatively easier to control but suffer from high power consumption and thermal latency. Electrical tunability leverages electric current to trigger a state change in materials like semiconductors, graphene, phase-change materials, or voltage-controlled materials. Although they offer fast and compact regulation, they are often faced with limited modulation depth, additional losses, or fabrication complexity. With the strong trade-offs between speed, tuning range, loss, system integration, and fabrication complexity in each of these schemes, tunability remains a challenge, especially in terahertz metasurface design.

Tunable or reconfigurable terahertz wave manipulation is essential for real-world systems; for instance, adaptive beam steering, polarisation versatility, and reconfigurable wavefront control are vital for several future terahertz applications like adaptive imaging, multifunctional sensing platforms, and terahertz communications links. Metasurfaces offer a scalable path to such reconfigurability, empowering functionality that would otherwise require multiple devices or mechanically complex systems.

1.3.2 Terahertz wave detection

One of the major constraints behind the limited deployment of terahertz technology lies in the difficulty of realising low-cost, compact, and room-temperature detector technologies that are readily scalable to large detector arrays (Niu *et al.*, 2020; Li *et al.*, 2023a; Sizov and Rogalski, 2010). Efficient detection of terahertz waves is necessary for the advancement of various terahertz applications like imaging, spectroscopy, and communications systems. However, detection of terahertz waves is not compatible with many conventional detection methods, such as photonic detectors that fail in this band due to the low photon energy of terahertz waves (Chen *et al.*, 2025).

Other detection types, such as thermal detectors, semiconductor detectors, and photoconductive antennas, do function in this band, yet bring in some performance trade-offs that require careful optimisation. For instance, thermal detectors, including bolometers, generally offer high responsivity and low NEP but at the cost of speed and are often

dependent on cryogenic operation for noise reduction (Rogalski and Sizov, 2011). This operational condition makes them bulky and impractical for many real-world applications. Semiconductor detectors, such as Schottky diode detectors, provide fast, compact, and sensitive room-temperature operation at sub-terahertz frequencies. However, their responsivity decreases with increasing frequency due to parasitic high-frequency effects and carrier transport limitations (Sizov and Rogalski, 2010). A reported study demonstrated responsivities of approximately $1000\,\mathrm{V\,W^{-1}}$ at 0.3 THz and $125\,\mathrm{V\,W^{-1}}$ at 1.3 THz for Schottky diode detectors (Ito *et al.*, 2008). In addition, semiconductor detectors and photoconductive antennas are relatively expensive and are not readily scalable to large detector arrays, posing further challenges for widespread implementation. These limitations have motivated the development of emerging techniques that enhance the interaction of detectors with terahertz waves without increasing system complexity.

Metasurfaces can enhance the interaction between incident terahertz waves and the active sensing region by promoting strong absorption at the detector interface (Zhang *et al.*, 2024). Resonant metasurfaces can be engineered to possess a matching impedance with that of free space and concentrate incident terahertz energy into localised regions. This boosts the absorbed power in the region within the active sensing element, thereby directly improving the responsivity and other performance parameters within the detector. Importantly, this enhancement can be achieved while keeping the detector volume low and preserving fast thermal response and compactness.

Beyond enhancing absorption, the ultrathin dimension of metasurfaces enables seamless integration with current detector technologies, including MEMS-based bolometers, semiconductor sensors, and hybrid optical readout methods. Their planar geometry is also compatible with standard microfabrication processes, making them well suited for scalable large-area detector arrays with relatively low fabrication complexity and cost. Furthermore, the ultrathin structure of metasurfaces can reduce the thermal mass of thermal detectors such as bolometers, thereby reducing the thermal time constant and enabling faster response speeds. Therefore, metasurfaces not only enhance detector performance but also facilitate system miniaturisation, scalable array fabrication, and high-speed terahertz detection, which are equally important for portable terahertz detection platforms.

1.3.3 Terahertz spectral analysis and spectrometer

Spectral information plays a crucial role in various terahertz applications such as material identification, chemical sensing, channel monitoring, and angle-of-arrival estimation in communications systems. Precise frequency prediction and detection support spectroscopic fingerprinting of materials, whereas information on the occupied bandwidth and propagation direction is vital for terahertz adaptive links and sensing environments.

Although traditional spectrometers in the terahertz regime, such as time-domain spectroscopy systems or mechanically tuned frequency-swept setups, offer high spectral resolution, they introduce high hardware complexity, increased size, and larger power consumption. As these methods usually utilise bulky optics, moving parts, or broadband sources and detectors, it is challenging for them to be used for compact and real-time applications. This clearly marks a trade-off between the effectiveness and adaptability of conventional spectroscopic techniques and their necessary infrastructures.

Dispersive metasurfaces based on phase-gradient structures support spatial separation of different frequencies, paving the way for compact spectrometers without moving parts (Jia *et al.*, 2021). These metasurfaces are designed with unit cells that exhibit similar amplitudes but different phase responses, which are arranged to excite a spatial phase gradient and function as dispersive devices providing smooth frequency spreading. Recently, metasurface-based techniques paired with machine-learning have demonstrated ways to analyse incident waves (Li *et al.*, 2024b). This system exploits planar metasurfaces to broaden the spatial features of the wave and transfers the feature processing to software from hardware, thereby trimming down the size and complexity of the system, while enabling real-time analysis. One such type of metasurface is based on the pseudo-random design (Imani *et al.*, 2020; Seidi *et al.*, 2025) strategy, where the phase-variant structures are designed in quasi-random patterns. This structure allows for more diverse frequency discrimination through patterns. Depending on the design and software implementation, different patterns can be used for specific mappings to convey various spectral information. These patterns are then applied to computational algorithms to train a model and reconstruct or predict the information. These strategies can be implemented for the estimation of frequency, angle-of-arrival, and other environmental conditions. Such metasurface-enabled spectrometry or wave analysis techniques naturally fits with the current trends in computational imaging and sensing,

where advanced systems are applied to reduce hardware complexity. In the terahertz domain, this shift is particularly beneficial for the development of compact, robust, and scalable platforms for practical spectral analysis.

Altogether, metasurfaces are capable of further advancing the development of terahertz wave manipulation, detection, and spectral analysis. Through precise control over the electromagnetic degrees of freedom, boosting the wave interaction with a designed structure, and incorporating machine-learning into the system, terahertz metasurfaces clearly create a pathway for promoting terahertz technology towards practical, compact, and high-performance devices.

1.4 Thesis outline and summary of original contributions

With the advent of terahertz wave generation techniques and extensive potential applications, devices for efficient manipulation, detection, and analysis of the waves are necessary to facilitate all possible functions. Practical deployment of such devices requires high performance and high efficiency while being ultrathin, compact, multifunctional, reconfigurable, and compatible with current terahertz systems. In this thesis, multiple terahertz devices with the above-mentioned features are proposed and demonstrated for the advancement of terahertz systems.

This thesis contains six chapters, including four chapters dedicated to original contributions. This current chapter sets the contextual background and motivation behind the thesis and provides an outline of the thesis along with a summary of original contributions. The next four chapters present the original contributions, while the final chapter offers a comprehensive conclusion and outlook. Although the individual chapters investigate different terahertz devices and applications, they are unified by the common objective of engineering the interaction between terahertz waves and artificially structured materials to advance terahertz technology. Together, these works cover many aspects of terahertz systems, spanning wave manipulation, detection, sensing and analysis. A summary of each chapter can be found as follows:

Chapter 1 - Introduction defines the terahertz frequencies within the electromagnetic spectrum and discusses their location and inherited benefits. This chapter further addresses the limitations of this frequency band and presents metasurfaces as a promising solution, thereby motivating this thesis. The concept of metasurfaces

is then introduced along with a brief literature review to provide the necessary background for the research and to establish the aims of this thesis.

Chapter 2 (Original Contribution) presents a metasurface consisting of two identical resonant plates that enable reconfigurable polarisation conversion. By mechanically tuning the separation between the plates, the device can switch between transmissive quarter-wave and half-wave plate functionalities. The metasurface operates across the terahertz communications band from 252 to 325 GHz, and can be simply installed into existing terahertz systems. The device is designed and analysed using full-wave electromagnetic simulation and an equivalent circuit model, and the results are validated via measurement. The contents of this chapter are published in Quader *et al.* (2024a) and later presented in an invited talk at the MAPCON conference in 2024 (Quader *et al.*, 2024c).

S. Quader contributed to the device design, simulation, experimental measurement, data analysis, and manuscript preparation.

- **Quader-S.**, Ako-R. T., Sriram-S., Fumeaux-C., and Withayachumnankul-W.(2024). Mechanically reconfigurable polarization converter for terahertz waves, *IEEE Transactions on Terahertz Science and Technology*, **14**(4), pp. 502–509.
- **Quader-S.**, Lv-X., You-X., Ako-R. T., Bhaskaran-M., Sriram-S., Fumeaux-C., and Withayachumnankul-W. (2024). Mechanically reconfigurable terahertz quasi-optical components for spectral filtering and polarization control, *IEEE Microwaves, Antennas and Propagation Conference (MAPCON)*, Hyderabad, India, pp. 1–4. (**Invited**)

Chapter 3 (Original Contribution) presents a microelectromechanical bolometer coupled with an antenna element to improve detection sensitivity. The device follows a monolithic design strategy by incorporating the electromagnetic absorber, thermal transducer, and mechanical resonator into a single element. Terahertz absorption induces a shift in the mechanical resonance, enabling effective detection under room-temperature, ambient air, and atmospheric pressure conditions. The device is designed and analysed using full-wave electromagnetic and mechanical simulations, and its performance is validated experimentally. The contents of the chapter were presented at the APMC conference, 2024 (Quader *et al.*, 2024b), and subsequently published in Quader *et al.* (2026).

S. Quader contributed to the device design, simulation, experimental measurement, data analysis, and manuscript preparation.

- **QUADER-S.**, FUMEAUX-C., AND WITHAYACHUMNANKUL-W. (2026). Antenna-coupled terahertz electromechanical bolometer, *APL Engineering Physics*, **1**(1), art. no. 016104. (**Invited, Featured**).
- **QUADER-S.**, FUMEAUX-C., AND WITHAYACHUMNANKUL-W. (2024). Antenna-coupled micro-electromechanical bolometer for terahertz detection, *IEEE Asia-Pacific Microwave Conference (APMC)*, Bali, Indonesia, pp. 802–804.

Chapter 4 (Original Contribution) presents a frequency-dispersive terahertz metasurface system enabling spatial spectral mapping. By introducing frequency-dependent angular dispersion through a quantised phase-gradient metasurface and mapping it using a dielectric focusing lens, the system enables compact spectrometer-like functionality. The metasurface is currently being fabricated, whereas the lens has been 3D-printed and experimentally characterised. A publication is under preparation.

S. Quader contributed to the device design, simulation, 3D-printing, experimental measurement, and data analysis.

Chapter 5 (Original Contribution) presents a 3D-printed pseudo-random metasurface coupled with machine-learning for precise frequency prediction in terahertz communications. The pseudo-random device exploits frequency-dependent unique spatial intensity patterns, allowing fine frequency discrimination at sub-gigahertz resolution from 220 to 330 GHz. The metasurface is 3D-printed, and corresponding transmitted intensity patterns are recorded, with varying input conditions. A convolutional neural network (CNN) model is trained over this large dataset to predict the incident frequency from the measured patterns. The contents of the chapter are published in Quader *et al.* (2025).

S. Quader contributed to the device design, 3D-printing, experimental measurement, data analysis, and manuscript preparation. His contribution excludes the implementation of convolutional neural network.

- **QUADER-S.**, ABDULLAH-M., HE-E., FUMEAUX-C., AND WITHAYACHUMNANKUL-W. (2025). 3D-printed frequency-diverse metasurface for camera-based terahertz frequency analyzer, *IEEE Microwave and*

Wireless Technology Letters, **35**(12), pp. 2105–2108. (**Selected by the committee for Special Issue on Asia-Pacific Microwave Conference 2025**)

Chapter 6 - Summary and Outlook concludes this thesis by summarising the key contributions and providing an outlook on future research directions built upon the proposed terahertz metasurfaces.

Chapter 2

Mechanically Reconfigurable Polarisation Converter

(Original Content)

IN terahertz systems, polarisation conversion is usually carried out using conventional waveplates. However, limitations in these waveplates arise from inadequate material accessibility, relatively narrow bandwidth, low efficiency, and bulkiness. To overcome these limitations, a transmissive terahertz metasurface with mechanically reconfigurable polarisation conversion is proposed. The separation between two identical metasurface plates is varied to switch between a quarter-wave plate and a half-wave plate functionalities. Measurement results verify that with no separation, the device can perform as a quarter-wave plate providing better than 3-dB axial ratio and an efficiency of over 75% from 246 to 320 GHz. With a separation of 150 μm between the two units, the transmission output becomes a cross-polarised wave with an 18-dB extinction ratio and an efficiency of over 74% across the same band. Altogether, the proposed polarisation conversion device provides the advantage of reconfigurability and can be simply installed into existing terahertz systems to achieve multiple functionalities.

2.1 Introduction

Terahertz waves are very suitable for many applications in wireless communications, spectroscopy, sensing, and imaging (Williams, 2005; Tonouchi, 2007; Song and Nagatsuma, 2011; Withayachumnankul *et al.*, 2018). Particularly, the IEEE 802.15.3d standard allocates a frequency range from 252 GHz to 325 GHz for switched point-to-point high-data-rate wireless communications (IEEE 802 LAN/MAN Standards Committee, 2017). To properly utilise terahertz waves for communications, imaging, and sensing, controlling their amplitude and phase is necessary. In addition, manipulating the polarisation state adds a degree of freedom in those applications, and is, in particular, crucial for communications (Chen *et al.*, 2023; Tamayama *et al.*, 2014). Conventional polarisation conversion devices or waveplates use natural crystalline birefringent materials with relatively large thickness, leading to narrow-band performance (Ji *et al.*, 2018; Masson and Gallot, 2006; Chen *et al.*, 2013). At terahertz frequencies, most suitable materials have a modest birefringence and are lossy (Chen *et al.*, 2006; Wiesauer and Jördens, 2013). The recent advancement of metasurfaces has solved the loss and bandwidth issues of polarisation converters (Chang *et al.*, 2019; Quader *et al.*, 2020b; Cheng *et al.*, 2014; Lee *et al.*, 2018; Ako *et al.*, 2019). The designable resonators forming an anisotropic metasurface allow flexible control over the phase of the incident terahertz wave components, leading to broadband polarisation conversion performance (You *et al.*, 2022). Also, metasurfaces are less lossy than bulk-material plates, and the resulting devices have a low profile (Al-Naib and Withayachumnankul, 2017; Ako *et al.*, 2020b).

Polarisation conversion devices can be classified into two major categories. One converts a polarised wave to its cross-polarised component, akin to a half-wave plate. The other, known as a quarter-wave plate, converts a linearly polarised wave to a circularly polarised wave or vice versa. Metasurface-based converters can be designed to perform either function and can operate in reflection or transmission. Polarisation converters working in transmission are more desirable than their reflective counterparts as they can be directly incorporated into communications systems or combined with sources. However, realisations of transmissive terahertz polarisation converters are limited in the literature, as they are more complicated to design and also usually suffer from low efficiency (Zi *et al.*, 2018; Grady *et al.*, 2013; Cong *et al.*, 2013; Cheng *et al.*, 2017; Ako *et al.*, 2020a; You *et al.*, 2021; Euler *et al.*, 2010; Wang *et al.*, 2015a; Cong *et al.*, 2014; Han *et al.*, 2018; You *et al.*, 2020). Most of these reported transmissive-type polarisation converters perform a single function. A transmissive dual-function polarisation converter using an

all-dielectric metasurface was simulated and measured in the work by Zi *et al.* (2020). This metasurface worked as a half-wave plate under one linear polarisation, and as a quarter-wave plate under the orthogonal polarisation. Its bandwidth remained limited to 2% at a centre frequency of 1 THz.

In this chapter, a reconfigurable metasurface is presented, which is made up of two separate but identical passive metasurface plates. By mechanically varying the separation between the two plates, the device can be reconfigured to realise two different functions, a quarter-wave plate and a half-wave plate, thereby enabling mechanically reconfigurable polarisation conversion. Each plate consists of metallic resonators on both sides of a cyclic olefin copolymer (COC) substrate. The device targets the terahertz communications band in IEEE 802.15.3d (IEEE 802 LAN/MAN Standards Committee, 2017).

2.2 Design

Here, we design a transmissive reconfigurable polarisation converter comprising two identical plates in a mirror-symmetric arrangement, as shown in Figure 2.1. Each plate has two metallic resonators made of gold, as presented in Figure 2.1(b) and (c), which are separated by a 100 µm thick COC spacer. The period p of one unit cell is 540 µm, such that $p \approx 0.5\lambda_0$ at a target centre frequency of 288 GHz. The resonator design is conceived to achieve inductive and capacitive responses for the two orthogonal linear polarisations, such that the transmission coefficients for the x and y polarised waves have similar amplitude, but their phase difference is adjustable by varying the separation between the plates.

The four metallic resonator layers provide a large tuning range in transmission phase, along with high transmission. In essence, the structure effectively allows to independently regulate the electric and magnetic dipole resonances relying on the concept of Huygens' metasurface.

As all the metallic layers have similar shapes and are separated by COC or air, they have similar equivalent circuit models. The equivalent circuit models for each metallic layer with respect to x and y polarisations are shown in Figure 2.2, with the metallic resonator shown in Figure 2.2(a). For the y polarisation, the thin metallic strip corresponds to the inductance L_{y1}, the gap between the elliptical metal patches forms capacitance C_{y1} parallel to L_{y1}, and another series capacitance C_{y2} forms due to the gap between

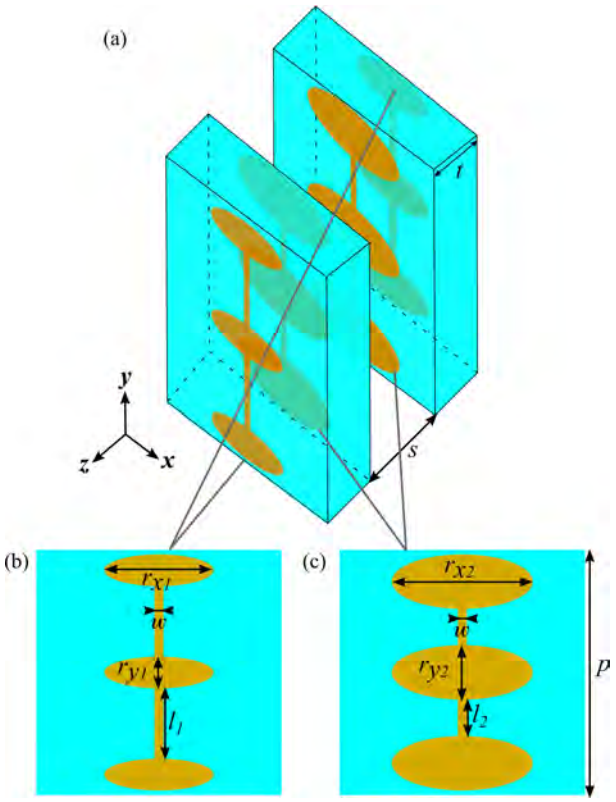

Figure 2.1. Metasurface structure. Schematic diagram of the polarisation conversion device. (a) Unit cell 3D view, (b) front metallic layer, and (c) back metallic layer. The geometric parameters of the design are $r_{x1} = 240$ µm, $r_{x2} = 310$ µm, $r_{y1} = 70$ µm, $r_{y2} = 120$ µm, $w = 20$ µm, $l_1 = 155$ µm, $l_2 = 80$ µm, $p = 540$ µm, $t = 100$ µm, and s is variable. Metallic resonators are made of gold to minimise metal loss and the substrate is cyclic olefin copolymer (COC) with a relative permittivity $\epsilon_r = 2.33$ and loss tangent $\tan\delta = 0.0005$ over the WR-3.4 band. Here, t denotes the thickness of each COC block. The two COC blocks forming the metasurface structure have identical thicknesses of 100 µm, while s represents the separation between them.

neighbouring unit cells, as shown in Figure 2.2(b). Here, the series combination of L_{y1} and C_{y2} is the dominant parameter. For the x polarisation, the elliptical metal shape yields the inductance L_{x1}, and the gap between neighbouring unit cells gives rise to capacitance C_{x1}, as presented in Figure 2.2(c). With all the above considerations, neglecting C_{y1} and considering all materials as lossless, the simplified admittance tensor for each metallic layer can be written as

$$\mathbf{Y}_{si} = \begin{bmatrix} \dfrac{j\omega C_{x1i}}{1-\omega^2 L_{x1i} C_{x1i}} & 0 \\ 0 & \dfrac{j\omega C_{y2i}}{1-\omega^2 L_{y1i} C_{y2i}} \end{bmatrix}, \tag{2.1}$$

where i indicates the metallic layer. Due to structural symmetry, there are no cross-coupling components in the tensor.

The inner and outer layers have different LC values based on different geometric parameters. The complete circuits for all layers while working as a quarter-wave plate ($s = 0$ µm) for both polarisations are shown in Figure 2.3, and the corresponding circuits while working as a half-wave plate ($s = 150$ µm) are shown in Figure 2.4. The equivalent circuit diagrams are almost the same for a specific polarisation for the cases $s = 150$ µm and $s = 0$ µm. In the absence of separation, the two inner metallic layers merge into one, and so the transmission line section portraying the air gap is no longer necessary, and the two inner LC branches merge into one. As a notable difference, the values of all corresponding C representing the middle layer for $s = 0$ µm increase from those used when $s = 150$ µm, due to the fact that the middle metallic layer is surrounded by COC on both sides, thus yielding higher electric energy storage.

The metasurface is simulated using the commercial software CST Microwave Studio with unit cell boundary conditions in the x and y directions, to emulate an infinite periodic array. In the z-direction, Floquet ports are employed to generate the normally incident plane waves and to retrieve the scattering coefficients for the transmitted

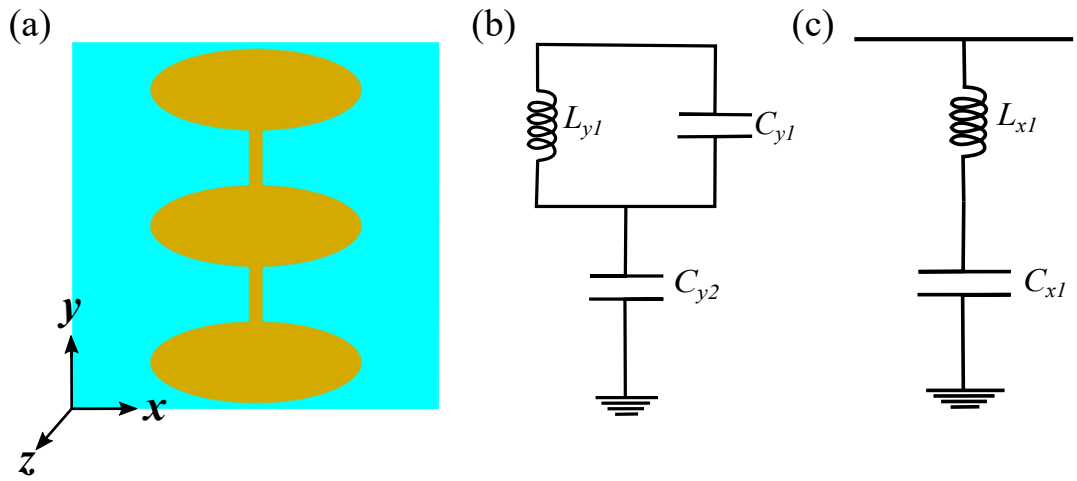

Figure 2.2. Circuit representation of metallic layers. Equivalent circuit model for each layer. (a) Metallic resonator. (b) Circuit models for y polarisation, and (c) x polarisation.

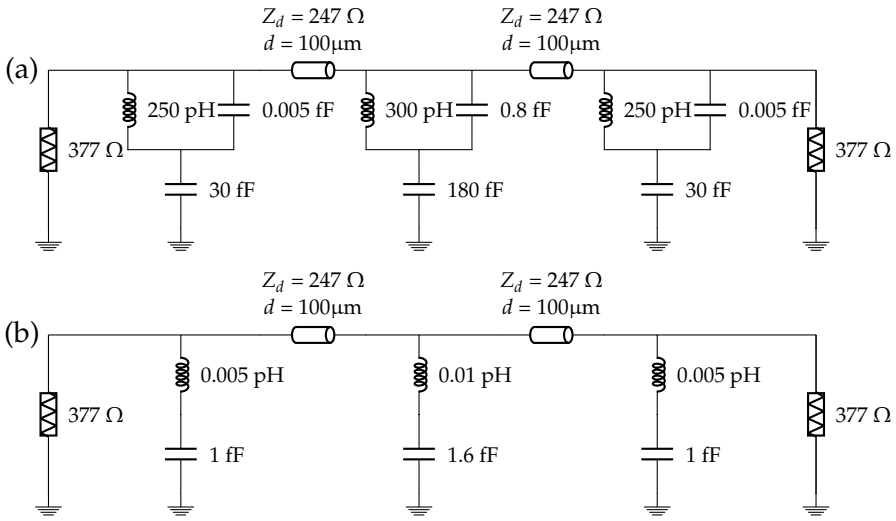

Figure 2.3. Circuit representation at 0 μm separation. Equivalent circuit model for the whole structure while working as a quarter-wave plate $s = 0$ μm. (a) Under y-polarised incidence, and (b) under x-polarised incidence. Here, Z_d is the characteristic impedance of the dielectric spacer, and d is the physical length of the equivalent transmission line section corresponding to each 100 μm COC block.

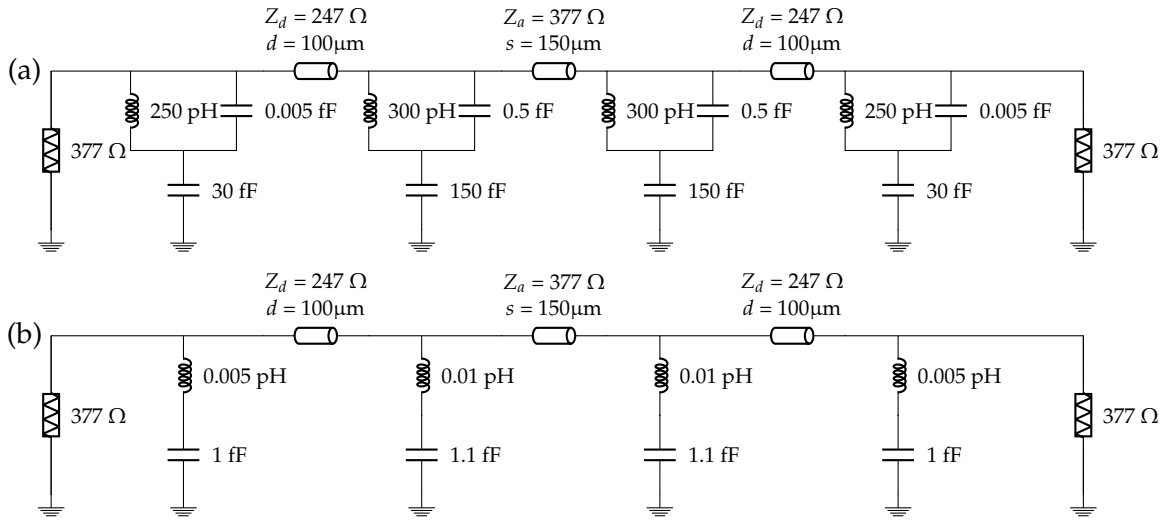

Figure 2.4. Circuit representation at 150 μm separation. Equivalent circuit model for the whole structure while working as a half-wave plate $s = 150$ μm. (a) Under y-polarised incidence, and (b) under x-polarised incidence. Here, Z_d, and Z_a are the characteristic impedance of the dielectric spacer and air, respectively, and d and s are the physical lengths of the equivalent transmission line sections corresponding to each 100 μm COC block, and 150 μm air gap between the blocks, respectively.

and reflected waves. The x-polarised transmitted wave for x-polarised incidence is denoted as S_{21}^{xx}. An analogous definition applies to S_{21}^{yy}. For the frequency of interest,

the relative permittivity of the COC dielectric spacer ϵ_r equals 2.33, and its loss tangent tan δ equals 0.0005 (Nielsen *et al.*, 2009). For the resonators, the surface impedance of gold at terahertz frequencies is described by a Drude model (Hashimshony *et al.*, 2001).

Here, the equivalent circuit parameters are not obtained from analytical expressions but through a full-wave simulation-assisted extraction approach. Individual resonator layers are first simulated in CST Microwave Studio, and equivalent *LC* branches are implemented in ADS. The inductance and capacitance values are then adjusted until the circuit response reproduced the corresponding CST resonance. The extracted resonator models are subsequently combined with transmission-line sections representing the dielectric spacers, with minor parameter adjustments made to improve agreement with the full-wave simulation response of the complete structure. Therefore, the reported inductance and capacitance values should be regarded as effective lumped-element parameters rather than exact physical inductances and capacitances.

2.3 Fabrication and measurement

The first step in the process is to fabricate a 5 μm thick COC base to support the metallic structure. This is done by spin-coating liquid COC (mr-I T 85 5.0) at 3000 r/min on a silicon (Si) wafer coated with sacrificial polymethyl-methacrylate (PMMA). Spin-coated liquid COC is used instead of commercial COC thin films, as the thickness of spin-coated COC is more controllable and the process results in a reasonably smooth surface to aid subsequent photolithography. Additionally, carefully prepared and treated COC is preferred to commercial COC due to its superior adhesion properties, specifically for the fabrication of double-sided devices. Conventional photolithography and electron beam deposition techniques are used to pattern the metallic structure on the COC base. In a separate process, a 100 μm thick COC is produced and bonded to the metallic structures patterned on a 5 μm COC substrate. This technique prevents dispersion of the metallic unit structures when liquid COC is spin-coated directly onto the metallic layer (Ako *et al.*, 2020b). It is also worth noting that many attempts to bond commercial COC films using this technique have failed. Next, the photolithography process is then employed to align the top pattern to the now sandwiched metallic layer. This is followed by metal deposition and lift-off. Finally, the free-standing device is released from the substrate when the sacrificial PMMA layer is dissolved in acetone. Other works by Lv *et al.* (2022), and Ako *et al.* (2020a), show that the extra 5 μm COC has no effect on

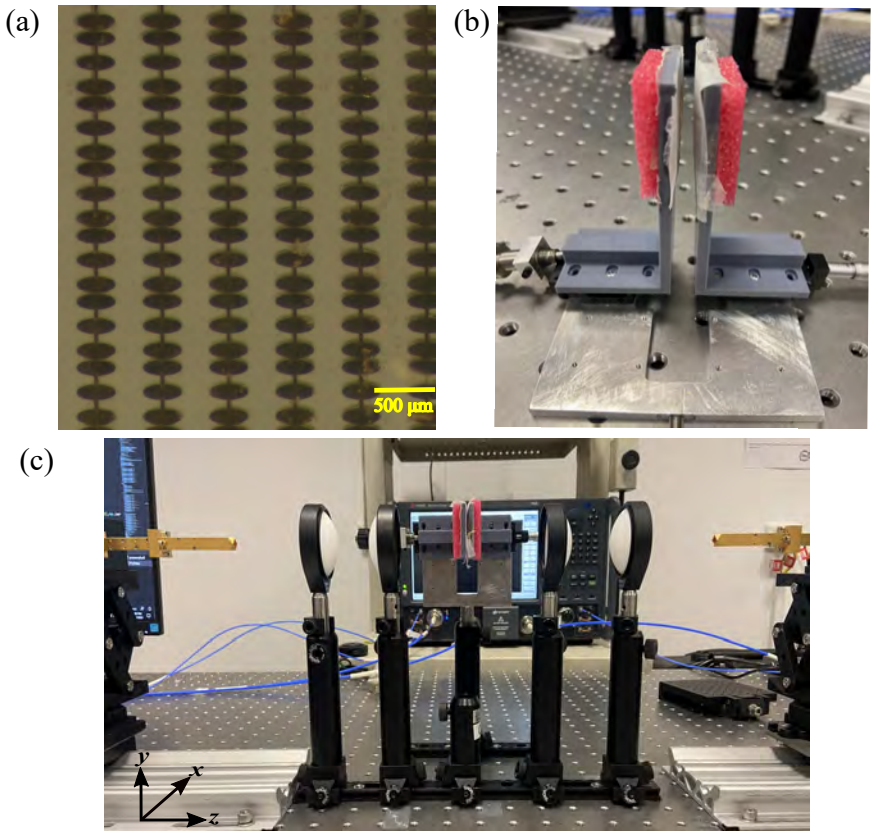

Figure 2.5. Metasurface sample and setup. Fabricated metasurface prototype and experimental setup. (a) Fabricated sample. (b) Sample pressed in the holder using low loss foam, and (c) measurement setup with four focusing lenses.

the performance of the device. Over a broad frequency range, the measured terahertz characteristics of the COC correspond well with the literature (Diaz-Albarran *et al.*, 2018; Cunningham *et al.*, 2011; Pavanello *et al.*, 2013; Motaharifar *et al.*, 2018). The effect of bonding the COC base with the COC slab, and the fabrication tolerance in the thickness of the COC spacer, t is negligible.

The metasurface is fabricated in one piece and then cut to form two separate layers of 25×25 mm^2 as shown in Figure 2.5(a). They are attached to the holder as depicted in Figure 2.5(b). Two 3D-printed L-brackets are attached to a metallic clamp with a Thorlabs differential screw DM10 for fine-tuning with micrometre resolution. Planarity and alignment are some of the important parameters that affect the performance of the metasurface. The effect of imperfect alignment is not separately quantified in this work, as the measured response is influenced by multiple coupled factors, including translational and rotational misalignment of the metasurface layers, fabrication non-uniformity, finite beam size, sample planarity, and uncertainty in the separation distance.

Nevertheless, these effects are minimised by carefully mounting and assembling the metasurface onto the L-brackets under a microscope. Furthermore, low-loss polystyrene foam, as shown in Figure 2.5(b), is used to properly press the two metasurface plates together to achieve close to 0 μm separation, as well as to ensure planarity and alignment of the metasurface. The foam exhibits a refractive index of approximately $n \approx 1.02$ and an absorption coefficient below 1.5 cm^{-1} across the terahertz band, resulting in negligible influence on the transmitted terahertz waves (Zhao *et al.*, 2002).

To verify the performance, the fabricated metasurface is measured using a Keysight Precision Network Analyzer (PNA) through VDI WR-3.4 extension modules. The modules operate from 220 to 330 GHz, covering the terahertz communications band from 252 to 325 GHz. A four-lens configuration is used as shown in Figure 2.5(c), where lens 1 collimates the incident wave, and lens 2 focuses the collimated beam onto the sample. The transmitted wave is then collimated by lens 3, where lens 4 focuses the collimated beam onto the receiver. A focal spot of 1 mm is achieved at the sample location to selectively illuminate a region with the highest uniformity on the metasurface. The emitter and receiver are linearly polarised along the x-axis. To measure orthogonal polarisations, the sample is rotated by 90°, and the transmitted wave is measured. No additional wire-grid polariser is required, as the VDI WR-3.4 transmitter and receiver modules inherently provide a well-defined linear polarisation state. As a reference, a measurement is taken without the sample to normalise the measured complex transmission spectra. Time gating is applied to eliminate multiple reflections from the setup, e.g., between the emitter, receiver, the sample, and within each lens.

2.4 Results

2.4.1 Quarter-wave plate

For a perfect quarter-wave plate, the transmission magnitudes of the orthogonal linearly polarised components must be equal to 1, i.e., $|S_{21}^{xx}| = |S_{21}^{yy}| = 0$ dB, and the phase difference must be 90°, i.e., $|\Delta\phi| = |\angle S_{21}^{xx} - \angle S_{21}^{yy}| = 90°$. The transmission magnitude of the S-parameters $|S_{21}^{xx}|$ and $|S_{21}^{yy}|$ from the equivalent circuit model, simulation, and measurement for the quarter-wave plate configuration ($s = 0$ µm) are shown in Figure 2.6(a), where the magnitudes of x and y-polarised transmission are high and nearly equal. Figure 2.6(b) shows the transmission phases $\angle S_{21}^{xx}$ and $\angle S_{21}^{yy}$, where it can be observed that the phase difference between the x and y polarised transmission is close to ideal, i.e., $|\Delta\phi| \approx 90°$. Although the results between the circuit model, measured, and simulated S-parameters are in general agreement, some minor discrepancies can be observed. These arise primarily from the simplified nature of the equivalent circuit model, which is based on effective lumped-element parameters extracted from individual unit cell responses and therefore cannot fully capture higher-order electromagnetic effects, inter-cell coupling, and finite-size effects present in the full-wave simulations and measurements. Furthermore, slight misalignment between the layers and the imperfect planarity of the metasurface introduce slight deviations in the measurement. Misalignment is the cause of a lower transmission magnitude and a frequency shift. Non-planarity and rotational misalignment are found in simulations to be the cause of ripples and a sudden drop in transmission in the measured results.

For a quarter-wave plate, two important performance metrics are the ellipticity and efficiency. Calculating ellipticity and efficiency involves the Stokes parameters, (McMaster, 1954),

$$\begin{aligned} S_0 &= |S_{21}^{xx}|^2 + |S_{21}^{yy}|^2 \\ S_1 &= |S_{21}^{xx}|^2 - |S_{21}^{yy}|^2 \\ S_2 &= 2|S_{21}^{xx}||S_{21}^{yy}|\cos(\Delta\phi) \\ S_3 &= 2|S_{21}^{xx}||S_{21}^{yy}|\sin(\Delta\phi). \end{aligned} \tag{2.2}$$

The ellipticity γ is the ratio S_3/S_0, where $\gamma = 1$ denotes an ideal left-handed circularly polarised (LHCP) output wave and $\gamma = -1$ denotes an ideal right-handed circularly polarised (RHCP) output wave. Additionally, the efficiency is equal to $S_0/2$. To further evaluate the polarisation conversion performance of the metasurface, the axial ratio

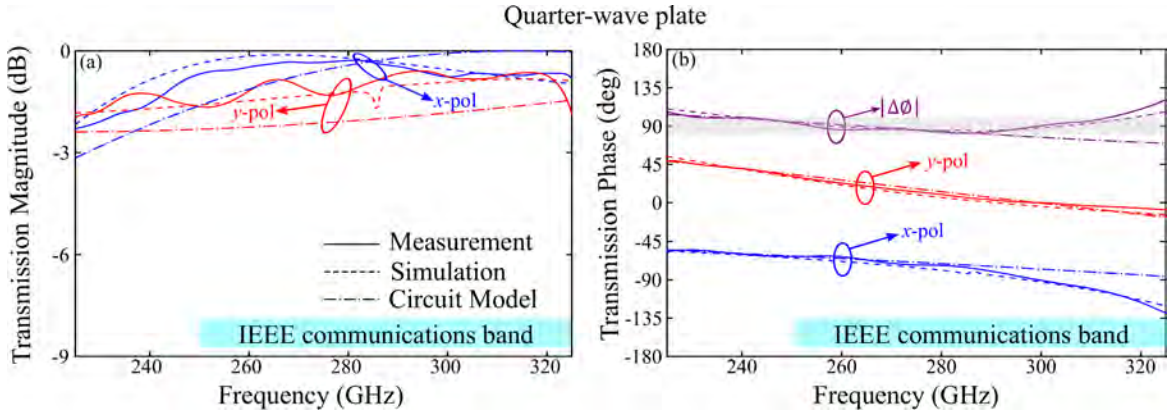

Figure 2.6. Quarter-wave plate simulated and measured transmission. Complex transmission coefficients of the metasurface at $s = 0$ µm for x and y polarisation. (a) Magnitude, and (b) phase with phase difference $|\Delta\phi|$. The region shaded in grey indicates the acceptable phase difference range around 90°, corresponding to quarter-wave plate operation.

(AR) of the transmitted wave is calculated as (You *et al.*, 2020),

$$\mathrm{AR} = \sqrt{\frac{E_x^2 + E_y^2 + \left[E_x^4 + E_y^4 + 2E_x^2E_y^2\cos(2\Delta\phi)\right]^{1/2}}{E_x^2 + E_y^2 - \left[E_x^4 + E_y^4 + 2E_x^2E_y^2\cos(2\Delta\phi)\right]^{1/2}}}, \tag{2.3}$$

where, $E_x = |S_{21}^{xx}|$ and $E_y = |S_{21}^{yy}|$. The axial ratio is the ratio of the major axis to the minor axis of the polarisation ellipse for the transmitted wave. The extinction ratio (ER) can also be calculated using the axial ratio as

$$\mathrm{ER} = \left(\frac{\mathrm{AR}+1}{\mathrm{AR}-1}\right)^2. \tag{2.4}$$

Figure 2.7 shows the calculated performance metrics from the equivalent circuit model, simulation, and measurement for the case where the device functions as a quarter-wave plate, i.e., $s = 0$ µm. Covering the terahertz communications band and beyond, from 246 to 325 GHz, the simulation results show that the ellipticity is over 95% and efficiency is above 75% as shown in Figure 2.7(a), with an axial ratio below 3-dB and extinction ratio above 30-dB through the same band, as shown in Figure 2.7(b) and (c), respectively. The measurement confirms the above claim up to 320 GHz. The nearly ideal circularly polarised output wave provides a very high ER, which is close to 120 dB at around 300 GHz for the measured result and approximately 70 dB at around 310 GHz for the simulation. This frequency shift in the ERs is caused by slight

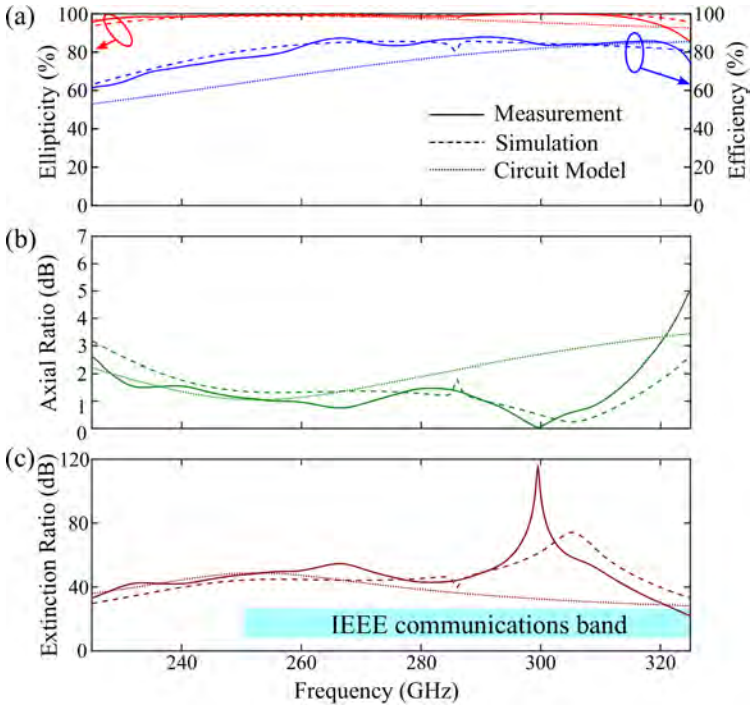

Figure 2.7. Quarter-wave plate performance. Performance parameters for the proposed device working as a quarter-wave plate at $s = 0$ µm. (a) Ellipticity and efficiency, (b) axial ratio, and (c) extinction ratio.

fabrication and measurement tolerances. Although the bandwidth is limited to the terahertz communications band and some other reported designs provided higher fractional bandwidth, the efficiency achieved in this work is very high compared to other recently reported transmissive quarter-wave plates, as presented in Table 2.1. The high efficiency is achieved due to the perfectly matched three-layer structure that enhances transmission based on the Huygens principle (Pfeiffer and Grbic, 2014).

To evaluate the robustness of the quarter-wave plate under practical operating conditions, its performance under oblique incidence is investigated. Figure 2.8 shows the simulated ellipticity for incidence angles from 0° to 40°. The ellipticity remains above 95% up to approximately 30° incidence across most of the terahertz communications band, confirming the stability of the quarter-wave plate performance for moderate angular deviations. Beyond 30°, the ellipticity gradually degrades at frequencies above 300 GHz, and a noticeable deterioration is observed at 40°.

The good angular stability can be attributed to the subwavelength periodicity and the use of broad elliptical resonators with distributed electromagnetic coupling across the multilayer structure. These structural features preserve the phase difference between the

Table 2.1. Performance comparison of transmissive terahertz quarter-wave plates. Comparison with other reported transmissive terahertz quarter-wave plates in terms of structural design, number of layers, spacer material, centre frequency, fractional bandwidth, and minimum efficiency.

Structure	Metallic Layers	Spacer Material	Centre Frequency (THz)	Fractional Bandwidth (AR < 3 dB)	Minimum Efficiency
Split slot rings (Euler *et al.*, 2010)	1	Silicon	0.325	12%	45%
Metal slots (Wang *et al.*, 2015a)	1	Polyethylene naphthalate	0.870	5%	30%
Metal gratings (Cong *et al.*, 2014)	2	Polyimide	1.180	44%	42%
Split ring resonators (Han *et al.*, 2018)	2	Benzocyclobutene	0.980	12%	62%
Metal pathches (You *et al.*, 2020)	3	COC	0.280	53%	70%
This work	3	COC	0.288	26%	75%

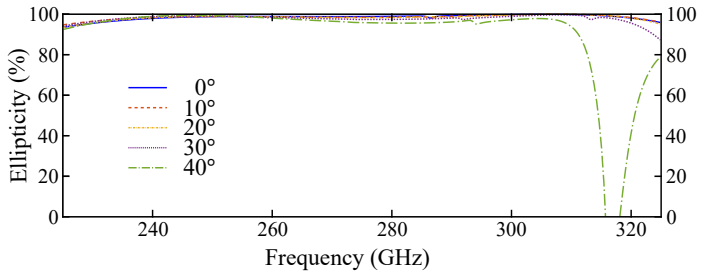

Figure 2.8. Angular stability of the quarter-wave plate under oblique incidence. Simulated ellipticity of the quarter-wave plate under oblique incidence for incidence angles ranging from 0° to 40°. The device maintains an ellipticity above 95% up to approximately 30° incidence across most of the operation band, demonstrating good angular stability.

orthogonal eigenmodes over a wide range of incidence angles while suppressing higher-order diffraction effects, thereby maintaining high ellipticity under oblique illumination. Furthermore, the device maintains high ellipticity up to approximately ±30° incidence, corresponding to an effective angular field of view of approximately 60°, which is advantageous for practical terahertz systems where perfect normal incidence cannot always be guaranteed.

2.4.2 Half-wave plate

To achieve an ideal half-wave plate, the magnitudes of orthogonal electric field components must be equal to unity, i.e., $|S_{21}^{xx}| = |S_{21}^{yy}| = 0$ dB, with the phase difference in this case being 180°, i.e., $|\Delta\phi| = |\angle S_{21}^{xx} - \angle S_{21}^{yy}| = 180°$. The metasurface with the

separation between two identical structures $s = 150$ µm works as a half-wave plate. As shown in Figure 2.9(a), the transmission magnitudes for the x and y polarised incidence remain high for frequencies above 250 GHz. However, at about 250 GHz and below, the transmission for the x-polarised incidence is relatively low due to strong resonance. The phases $\angle S_{21}^{xx}$ and $\angle S_{21}^{yy}$ are shown in Figure 2.9(b) with a phase difference between the x and y-polarised transmission, $|\Delta\phi| \approx 180°$.

For a half-wave plate, two important performance metrics are the polarisation conversion ratio (PCR) and the efficiency. The equations to calculate PCR and efficiency of a half-wave plate are presented as

$$\begin{aligned} \text{PCR} &= \frac{|t_{\text{cross}}|^2}{|t_{\text{cross}}|^2 + |t_{\text{co}}|^2}, \\ \text{Eff} &= |t_{\text{cross}}|^2, \\ t_{\text{co}} &= \frac{S_{21}^{xx} + S_{21}^{yy}}{2}, \\ t_{\text{cross}} &= \frac{S_{21}^{xx} - S_{21}^{yy}}{2}. \end{aligned} \tag{2.5}$$

To further evaluate the performance of the polarisation conversion metasurface, the extinction ratio is calculated as

$$\text{ER} = 10 \log_{10} \left(\frac{|t_{\text{cross}}|^2}{|t_{\text{co}}|^2} \right). \tag{2.6}$$

Figure 2.10 shows the calculated performance metrics from the equivalent circuit model, simulation, and measurement, when the device functions as a half-wave plate, i.e.,

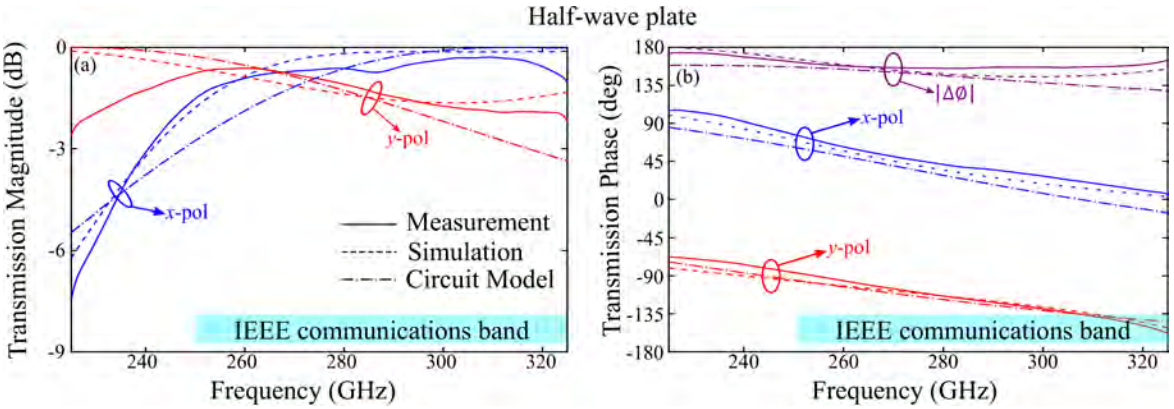

Figure 2.9. Half-wave plate simulated and measured transmission. Complex transmission coefficients of the metasurface at $s = 150$ µm for x and y polarisation. (a) Magnitude, and (b) phase with phase difference $|\Delta\phi|$.

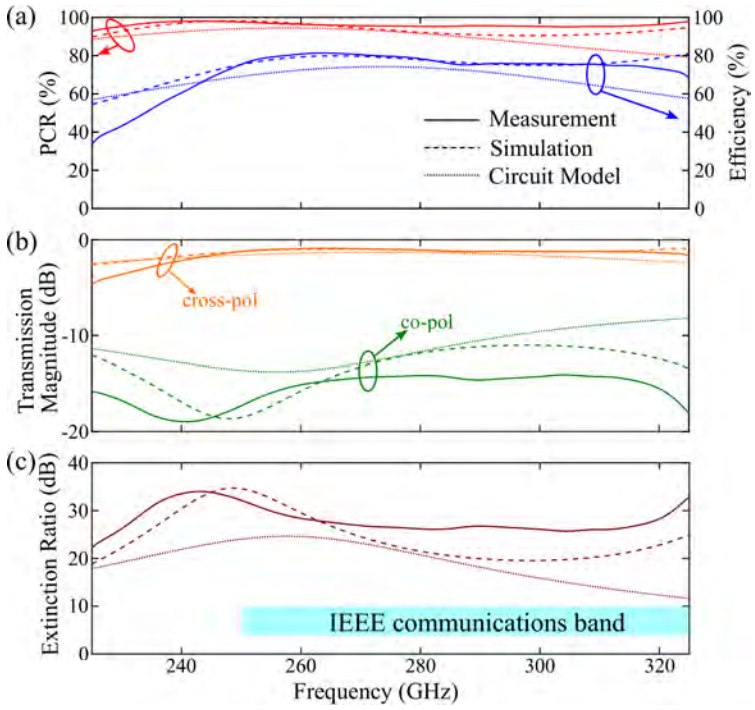

Figure 2.10. Half-wave plate performance. Performance parameters for the proposed device working as a half-wave plate at $s = 150$ µm. (a) PCR and efficiency, (b) co and cross-polarisation transmission magnitudes, and (c) extinction ratio.

$s = 150$ µm. Figure 2.10(a) shows that in the frequency band ranging from 246 to 325 GHz, enclosing the terahertz communications band, the simulated PCR is over 90%, and efficiency is above 74%. The simulated extinction ratio is beyond 18 dB for the same band as shown in Figure 2.10(c). Figure 2.10(b) shows the co- and cross-polarisation transmission magnitudes. The larger discrepancy observed between the equivalent circuit model and the simulation in Figure 2.10 for the half-wave plate configuration is primarily associated with the limitations of the equivalent circuit model. As discussed in Section 2.2, the equivalent circuit parameters are extracted from the resonator response and subsequently combined with transmission-line sections. While this approach provides good agreement for the quarter-wave plate configuration, where the inner metallic layers are in close contact, the half-wave plate response relies on electromagnetic coupling over the 150 µm air gap. These effects are captured more accurately in the simulation than in the simplified equivalent circuit representation, resulting in increased discrepancy with increasing layer separation. Nevertheless, the agreement remains strongest near the centre of the operation band, around the design frequency of 275 GHz, where the equivalent circuit parameters are optimised.

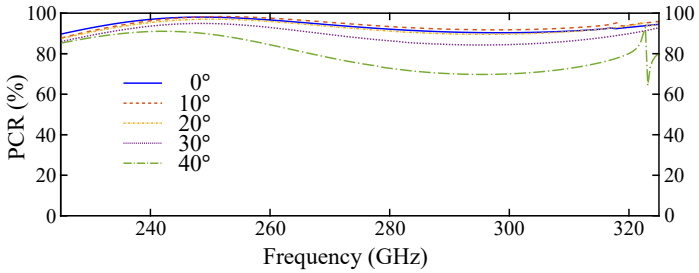

Figure 2.11. Angular stability of the half-wave plate under oblique incidence. Simulated polarisation conversion ratio of the half-wave plate under oblique incidence for incidence angles ranging from 0° to 40°. The device maintains a PCR above 80% up to approximately 30° incidence acros most of the operation band, demonstrating good angular stability.

Figure 2.11 shows the simulated PCR of the half-wave plate under oblique incidence for angles ranging from 0° to 40°. Compared to the quarter-wave plate configuration, the half-wave plate exhibits a stronger dependence on the incidence angle. Nevertheless, the device maintains good performance, with the PCR remaining above 80% for incidence angles up to approximately 30° across most of the operation band. The slight reduction in PCR with increasing angle is primarily attributed to the presence of the 150 μm air gap, which causes variations in the effective propagation path length and interlayer coupling under oblique illumination. Beyond 30°, the PCR degrades more noticeably, particularly at the upper end of the operation band. Despite this behaviour, the results demonstrate good angular tolerance for practical terahertz applications.

Measurement results confirm the claim of above 18 dB extinction ratio, and the PCR of above 90% for the whole band, the 74% efficiency remains up to 320 GHz, but stays above 70% for the whole band. Although the efficiency and PCR are reasonably high, the design has a slightly smaller fractional bandwidth and smaller efficiency compared to other recently reported designs, as shown in Table 2.2. In our case, the fractional bandwidth is limited to the terahertz communications band, and the efficiency is slightly lower as our design requires more metallic layers. Moreover, in our case, the extinction ratio is beyond 18 dB within the limited fractional bandwidth, as compared to over 12 dB or 15 dB extinction ratios achieved in other recently reported designs. Additionally, our device is reconfigurable as a dual-function polarisation converter.

Table 2.2. Performance comparison of transmissive terahertz half-wave plates. Comparison with other reported transmissive terahertz half-wave plates in terms of structural design, number of layers, spacer material, centre frequency, fractional bandwidth, and minimum efficiency.

Structure	Metallic Layers	Spacer Material	Centre Frequency (THz)	Fractional Bandwidth (ER > 12 dB)	Minimum Efficiency
Cylindrical pillars (Zi *et al.*, 2018)	2	Silicon	1.000	20%	80%
Cut wires (Grady *et al.*, 2013)	3	Polyimide	1.080	52%	80%
Wire gratings (Cong *et al.*, 2013)	3	Polyimide on silicon	1.025	102%	85%
Diode-like split rings (Cheng *et al.*, 2017)	3	Benzocyclobutene	0.700	134%	90%
SRR and *H* resonator (Ako *et al.*, 2020a)	3	COC	0.620	133%	80%
Metallic strips (You *et al.*, 2021)	3	COC	0.260	32% (ER > 15 dB)	77%
This work	4	COC	0.288	26% (ER > 18 dB)	74%

2.5 Conclusion

This chapter has proposed metasurface that operates as a mechanically reconfigurable polarisation converter for the IEEE terahertz communications band between 252 and 325 GHz, and beyond. Each metallic layer is made of three ellipses connected by a thin strip line, and separated from an adjacent layer by a 100 μm thick COC spacer. With two identical plates in contact, the device works as a quarter-wave plate with a 3-dB axial ratio, 30-dB extinction ratio, an ellipticity of over 95%, and efficiency of over 75% throughout the frequency band of interest. When the two identical units are separated by an air gap of 150 μm, the device functions as a half-wave plate, with above 18 dB extinction ratio, a PCR of above 90%, and an efficiency of above 74%. Measurement results confirm the performance metrics up to 320 GHz. An equivalent circuit model has been used to analyse the design. The metasurface provides convenient reconfigurability between polarisation states with high performance. Since it operates in transmissive mode, it can be readily incorporated into existing systems.

Chapter 3

Antenna-coupled Electromechanical Bolometer

(Original Content)

THE advancement of terahertz sensing and imaging applications is contingent upon the development of detectors that are compact, low-noise, and operate reliably at room temperature. Traditional terahertz bolometers are often constrained by limited absorption efficiency, low sensitivity, slow response times, and bulky architecture. We demonstrate an antenna-coupled microelectromechanical system bolometer for terahertz detection, featuring a spiral-shaped niobium antenna suspended above an air cavity on a cyclic olefin copolymer substrate and backed by a gold plate with periodically arranged square apertures. The spiral operating as an efficient terahertz absorber, thermal transducer, and mechanical resonator, makes the device compact and enhances sensitivity and responsivity. Upon exposure to terahertz radiation near the absorption peak of the structure, thermal expansion induces a redshift in the mechanical resonance frequency of the spiral, which is detected using a laser vibrometer through the rear gold plate. Experimental measurements show a clear resonance shift from 12.25 to 11.16 kHz under incident terahertz radiation at 278 GHz, with power levels from 0 to 0.9 mW. This result corresponds to a thermomechanical responsivity of $\sim$1200 Hz/mW. Operating at room temperature and relying on monolithic implementation, the proposed device offers a sensitive, compact, and scalable platform for terahertz sensing and imaging applications.

3.1 Introduction

The terahertz spectral range has attracted considerable interest because of its unique ability to characterise materials through their biological and chemical signatures non-destructively and with high spatial resolution (Wang *et al.*, 2018; Wallace *et al.*, 2008; Baxter and Guglietta, 2011). This is immensely useful for applications in spectroscopy (Jepsen *et al.*, 2011), biomedical imaging (MacPherson *et al.*, 2013; Wallace *et al.*, 2006), security screening (Cheng *et al.*, 2021; Li *et al.*, 2018), and also in high-speed wireless communications (Jornet *et al.*, 2024) due to the huge untapped bandwidth. Yet, the unavailability of fast, compact, sensitive, and room-temperature compatible detectors, especially in the lower terahertz range, has substantially hindered the development of practical terahertz imaging systems (Niu *et al.*, 2020; Li *et al.*, 2023a). Thus, terahertz detectors with such features are important for the evolution of many practical terahertz applications.

Although photon detectors are faster and can be highly sensitive, they are generally not suitable for terahertz detection as the energy of terahertz photons lies in the sub-bandgap region of most semiconductor materials used in such detectors. On the other hand, thermal detectors, particularly bolometers, are well-suited for terahertz detection due to their ability to operate sensitively at room temperature (Peng *et al.*, 2025). Bolometers convert absorbed radiation into heat for detection through temperature rise. Conventional bolometers utilise temperature-induced change in resistance as an output signal (Bielecki *et al.*, 2024). This approach inherently depends on precise biasing, causes bias instability and drift, and implicates a trade-off between miniaturisation and speed versus sensitivity and responsivity (Niu *et al.*, 2020; Cherednichenko *et al.*, 2011).

Alternatively, microelectromechanical system (MEMS) bolometers convert absorbed energy into electromechanical effects, allowing highly effective terahertz detection. Due to their transduction pathway, MEMS bolometers support miniaturisation and low thermal mass, unlike conventional bolometers. As a result, they yield a high mechanical quality factor, fast response time, high sensitivity, and high responsivity (Zhang *et al.*, 2019; Liu *et al.*, 2022). Although some MEMS implementations may exhibit hysteresis arising from thermal and mechanical effects, depending on the transduction mechanism, materials, and operating conditions, such effects can generally be minimised through appropriate device design and operation within the linear regime. Several MEMS bolometers resort to piezoresistive (Chu *et al.*, 2017; Rahafrooz and Pourkamali, 2012; Bhattacharya and Li, 2019), capacitive (Naing *et al.*, 2020; Hsu *et al.*, 2001; Clark *et al.*,

2005), or piezoelectric (Muralt *et al.*, 2005; Zuo *et al.*, 2010; Lin *et al.*, 2012) readout mechanisms to detect subsequent electromechanical effects. These methods still require electrical contacts and complex on-chip circuitry, which are impacted by environmental noise and often degrade thermal isolation, resulting in lower sensitivity and slower response. Moreover, electrical bias can inadvertently heat up the detecting element, introducing additional disturbances to the readout. Optical readout approaches, such as interferometry and laser vibrometry, provide a non-contact substitute capable of detecting picoscale displacements with high spatial and temporal resolution. These methods eliminate the need for electrical transduction, thereby reducing noise and enabling streamlined integration with minimal thermal disturbance to the system.

Although numerous MEMS resonator bolometers have been proposed in the infrared spectral range (Gokhale and Rais-Zadeh, 2013; Piller *et al.*, 2019; Zhang *et al.*, 2013; Sadeghi *et al.*, 2020; Vicarelli *et al.*, 2022; Zhang *et al.*, 2019, 2016, 2025a), relatively few have operated as terahertz detectors at room temperature. The performance of these terahertz room temperature detectors varies significantly depending on the design strategy and readout scheme. A widely implemented MEMS bolometer structure is based on a bi-layer cantilever architecture (Froberger *et al.*, 2022; Zhu *et al.*, 2022; Belacel *et al.*, 2017; Liu *et al.*, 2022). A split-ring resonator (Belacel *et al.*, 2017), or half-wave dipole antenna (Froberger *et al.*, 2022) was integrated on the cantilever for terahertz absorption, and the out-of-plane mechanical deformation was optically readout using a near-infrared laser and a balanced photodiode scheme. Another similar structure utilised visible light microscopy to readout the cantilever displacement (Zhu *et al.*, 2022). One very advanced readout technique is the optical interferometry using a phase-locked loop (PLL) to track the resonance frequency shift (Liu *et al.*, 2022; Zhang *et al.*, 2024, 2019; Vicarelli *et al.*, 2022). The work by Liu *et al.* (2022) used a doubly clamped bi-material nanobeam as a terahertz resonator, whereas Zhang *et al.* (2024), utilised a silicon nitride membrane as a nanomechanical resonator with a metasurface absorber, both to be read via optical interferometry. One prominent design employed a nickel-chromium (NiCr) terahertz absorber on top of a suspended multilayered gallium arsenide (GaAs) and aluminium gallium arsenide (AlGaAs) heterostructure microbeam incorporating a two-dimensional electron gas (2DEG) (Zhang *et al.*, 2019). The 2DEG, along with top gates on both ends of the beam, forms two piezoelectric capacitors enabling excitation and detection. The response was processed using a PLL for resonance-frequency tracking, yielding an optical noise equivalent power (NEP) of $500\,\mathrm{pW}\cdot\mathrm{Hz}^{-0.5}$, responsivity of

$39.3\,\mathrm{kHz} \cdot \mathrm{mW}^{-1}$, and operation speed in the kilohertz range, at the operation frequency of 250 GHz, under vacuum conditions.

Another work featured a chromium-gold (Cr–Au) coated silicon nitride (Si_3N_4) trampoline membrane, which vibrates freely at its mechanical resonance frequency. Upon absorption of terahertz radiation of around 140 GHz, the shift in mechanical resonance frequency of the out-of-plane vibration was read out by a 945 nm self-mixing laser interferometric probe (Vicarelli *et al.*, 2022). This setup provided a low NEP of $100\,\mathrm{pW} \cdot \mathrm{Hz}^{-0.5}$. Nevertheless, this device relied on front-side laser illumination, which complicates optical alignment and may interfere with terahertz illumination. A very recent work featuring a piezoresistive readout with broadband (1–10 THz) NiCr terahertz absorber layer on a silicon-on-insulator platform was presented by Zhang *et al.* (2025a). The proposed detector achieved a very low NEP of $36\,\mathrm{pW} \cdot \mathrm{Hz}^{-0.5}$. Although favourable sensitivity, responsivity, NEP, and speed were demonstrated at room temperature for most of the reported works, only a limited number explicitly provide the terahertz absorption spectrum (Zhang *et al.*, 2024; Niu *et al.*, 2020; Liu *et al.*, 2022; Belacel *et al.*, 2017; Zhu *et al.*, 2022; Froberger *et al.*, 2022), leaving the absorption efficiency throughout the band unclear. Among the studies that report absorption spectra, most exhibit efficiencies below 50%, with a few exceptions, for instance, Zhu *et al.* (2022).

Enhancing terahertz absorption efficiency can significantly increase the responsivity of the bolometer. This can be achieved by integrating a properly matched antenna element (Quader *et al.*, 2024b). Additionally, a well-designed antenna element can subsequently reduce NEP, speed up thermal response times, and broaden the operating temperature range (Bielecki *et al.*, 2024). Various antenna configurations are usually employed to achieve high terahertz absorption, of which spiral antennas notably offer good absorption, provide linear polarisation insensitivity, and demonstrate efficient field confinement (Gou *et al.*, 2017; Liu *et al.*, 2008; Huang *et al.*, 2013; Wu *et al.*, 2018). From the mechanical perspective, spiral and spiral flexure geometries are well-suited for MEMS bolometer antenna designs as they allow flexible movement in the out-of-plane direction while remaining relatively stiff in other directions. A notable study demonstrated a microbridge bolometer integrated with a spiral-type antenna (Gou *et al.*, 2017). However, the work focused solely on simulated absorption spectra and lacked experimental validation or a functional detection system.

This chapter presents and experimentally demonstrates an antenna-coupled, MEMS-based bolometer for terahertz detection. The device features an Archimedean-spiral-shaped niobium structure suspended above an air cavity within a cyclic olefin copolymer (COC) substrate, backed by a gold periodic lattice of square apertures. This spiral acts simultaneously as an efficient terahertz absorber and a mechanical resonator, making it a monolithic bolometer by unifying the absorber, thermal transducer, and mechanical resonator in a single microfabricated structure. This approach eliminates heat transfer between the absorber and the resonator element, minimising heat loss and thermal lag, thus speeding up the device response. Additionally, a monolithic implementation makes the device more compact, thus reducing thermal mass, increasing responsivity, and sensitivity to low-power terahertz signals. The responsivity and sensitivity are further improved through efficient absorption of terahertz waves using a well-matched antenna element featuring a spiral design. When illuminated by terahertz radiation, the absorbed energy induces localised heating and thermal expansion, resulting in a red shift of the spiral's mechanical resonance frequency. This shift is optically measured using a laser vibrometer from the backside to ease the system alignment and increase measurement flexibility. The vibrometer senses out-of-plane motion without any electrical interface or physical contact, resulting in a compact, passive architecture well-suited for room-temperature terahertz sensing. Overall, the device offers a compact, sensitive, and responsive room-temperature terahertz detector.

3.2 Device architecture and characterisation approach

3.2.1 Device design and materials

To achieve high performance as a monolithic bolometer, an optimally balanced structure must provide strong terahertz absorption, efficient electromagnetic-to-thermal conversion, and excellent mechanical resonance vibrations, mainly in the out-of-plane direction for efficient non contact optical readout using a laser Doppler vibrometer. In terms of structural design, a spiral configuration supersedes most other designs. Spiral antennas have long been proven to provide strong broadband or frequency-selective terahertz absorption. The spiral geometry naturally concentrates surface currents towards its centre, leading to localised heating where the structure is most mechanically sensitive, resulting in a strong impact on its mechanical vibrations. Spirals also exhibit linear polarisation insensitivity to incident electromagnetic waves. Furthermore, the

mechanical symmetry of spirals naturally reduces the axial stiffness while boosting the lateral stiffness, promoting strong out-of-plane vibrations.

Niobium is selected as the spiral material due to its well-balanced combination of terahertz absorption, thermal behaviour, and mechanical performance. With a moderate electrical resistivity of around $16\,\mu\Omega \cdot \mathrm{cm}$, it supports localised Joule heating and efficient terahertz absorption. A thermal conductivity of $53.7\ \mathrm{W{\cdot}m^{-1}{\cdot}K^{-1}}$ provides a balance between adequate heat dissipation and the prevention of thermal accumulation or lagging thermal response. Likewise, a balanced Young's modulus, E_0, of 105 GPa, thermal expansion coefficient of $7.2 \times 10^{-6}\,\mathrm{K^{-1}}$, and density of $8.5\,\mathrm{g{\cdot}cm^{-3}}$ altogether ensure mechanical stability without excessive brittleness or mass loading, while maintaining sufficient thermal responsiveness to yield measurable vibration amplitudes. The rationale for selecting niobium over alternative materials is discussed further in the Appendix A. Niobium has also been demonstrated to enable fast and sensitive detection of terahertz waves (Reese *et al.*, 2007). With an excellent fabrication compatibility, measurable vibration response, thermal sensitivity, and structural integrity, niobium-based spiral structures are ideal for MEMS-based terahertz bolometers.

Herein, we design a bolometer operating over a narrow band to significantly suppress the effect of blackbody radiation, which is prominent at room temperature. In contrast to broadband detectors, narrowband detectors suppress unwanted frequencies, resulting in a cleaner baseline signal, thus enhancing the signal-to-noise ratio, responsivity, and measurement accuracy. Our design aims to achieve peak narrowband absorption at around 275 GHz, which is the centre frequency of the WR-3.4 band (220–330 GHz). The device is shown in Figure 3.1. The niobium spiral antenna, as shown in Figure 3.1(a) with thin arms and a smaller centre, is optimised to ensure strong absorption near the target frequency and to concentrate induced surface current more tightly, leading to stronger localised Joule heating in the spiral centre, improving responsivity. A 50 μm thick niobium layer is selected due to its optimal balance between maintaining structural integrity and out-of-plane mechanical resonance.

The resonator-antenna structure is supported by a 300 μm-thick slab of COC, where a 500 μm-wide and 100 μm-deep air cavity is etched right underneath the spiral, primarily to enable unhindered out-of-plane mechanical vibration and provide thermal isolation. The substrate is selected as COC due to its favorable properties at terahertz frequencies, including a low loss tangent of 0.0005 and a relative permittivity of

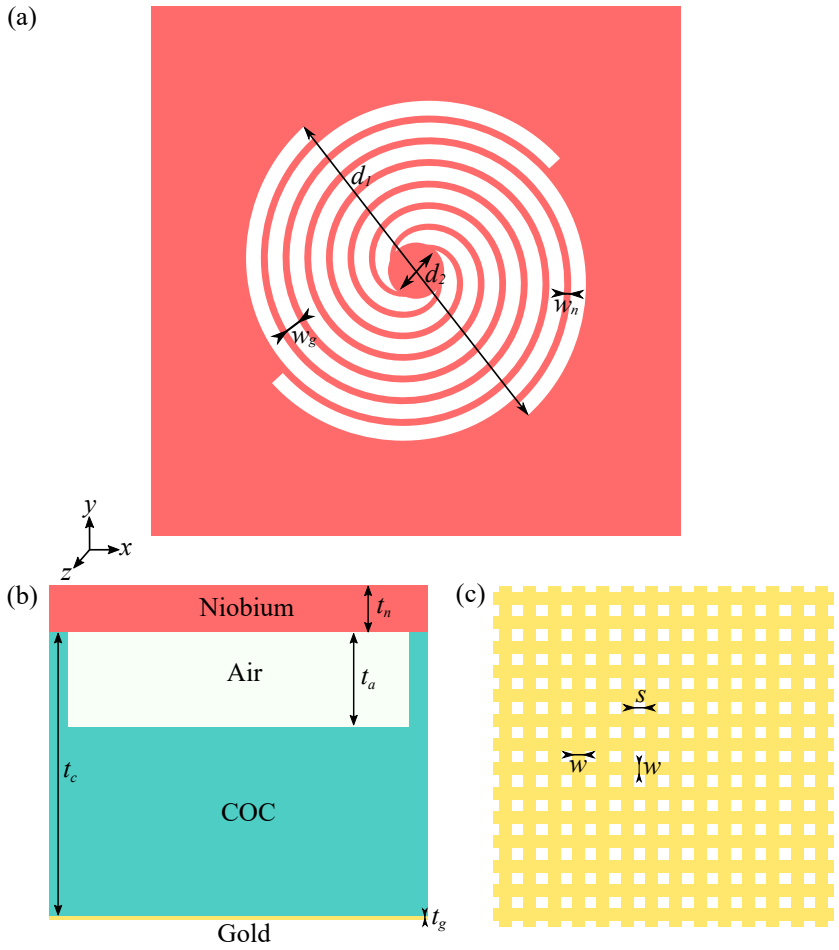

Figure 3.1. MEMS bolometer device layout. Schematic of the MEMS bolometer structure. (a) Top view showing the niobium Archimedean spiral antenna, with spiral diameter $d_1 = 360$ µm, core diameter $d_2 = 60$ µm, spiral arm width $w_n = 7$ µm, gap between spiral arms $w_g = 15$ µm. (b) Cross-sectional schematic illustrating the layered structure comprising a niobium absorber with thickness $t_n = 50$ µm, air cavity with thickness $t_a = 100$ µm, cyclic olefin copolymer (COC) support with thickness $t_c = 300$ µm, and gold back reflector with thickness $t_g = 1$ µm. (c) Patterned gold backplane showing periodic square apertures with gold strips of width $w = 20$ µm and spacing $s = 20$ µm.

2.33 (Nielsen *et al.*, 2009; You *et al.*, 2021). To improve absorption efficiency and suppress terahertz transmission, a gold back reflector is placed at the rear side of the COC, where the surface impedance of the gold layer at terahertz frequencies is described by a Drude model (Hashimshony *et al.*, 2001). The constructive interference of the multiple internal reflections between the spiral antenna and the reflective gold plane considerably improves the overall absorption. The gold back plate is designed as a periodic square-lattice of 20 µm square apertures, as shown in Figure 3.1(c), to permit

the laser beam to pass through. COC being highly transparent to optical probing, this design facilitates non-contact optical readout via backside laser vibrometry, reducing alignment complexity while preserving signal clarity from the vibrating spiral resonator.

3.2.2 Numerical modelling

To evaluate the performance of the monolithic bolometer, an extensive numerical modelling framework is used, integrating electromagnetic, thermal, and mechanical analysis. To begin with, the electromagnetic response of the niobium spiral is evaluated using full-wave finite-element simulations in CST Microwave Studio. The device is simulated under open boundary conditions in the in-plane directions, with a plane wave incident along the out-of-plane direction directed towards the niobium spiral. Although the targeted absorption peak is at 275 GHz, the simulated peak is slightly shifted for practicality and the need to maintain fabricable, rounded spiral dimensions. To identify the peak resonance frequency, frequency-dependent electric field confinement at the centre of the spiral is observed as shown in Figure 3.2(a). The electric field reaches its peak at around 277.5 GHz, indicating the strongest coupling between the terahertz wave and the spiral at the resonance frequency. Additionally, the frequency-dependent power loss in niobium also exhibits a peak near the same frequency, indicating that most of the terahertz energy around 277.5 GHz is effectively absorbed and dissipated as heat. To further verify absorption in the spiral structure, the electric field and surface current distribution on the niobium spiral at the resonance frequency are analysed. The strong confinement of electric fields around the spiral arm, as shown in Figure 3.2(b), indicates energy being effectively trapped within the spiral structure. Similarly, at the resonance frequency, the spiral design attracts high current density as shown in Figure 3.2(c). The co-localisation of high electric fields and surface currents at the resonance frequency indicates that the structure effectively absorbs incident electromagnetic energy and dissipates it as heat through Ohmic loss.

Following the electromagnetic analysis, the mechanical characteristics of the spiral are investigated using COMSOL Multiphysics. Initially, to determine the natural mechanical resonance frequency of the spiral structure, an eigenfrequency study is conducted within the solid mechanics module. By treating the niobium parts in contact with the COC support as fixed boundaries, the natural mechanical frequency is found to be 12.20 kHz. Figure 3.3 shows the mechanical vibrational mode of the structure, which confirms that the vibrations are restricted to out-of-place displacement.

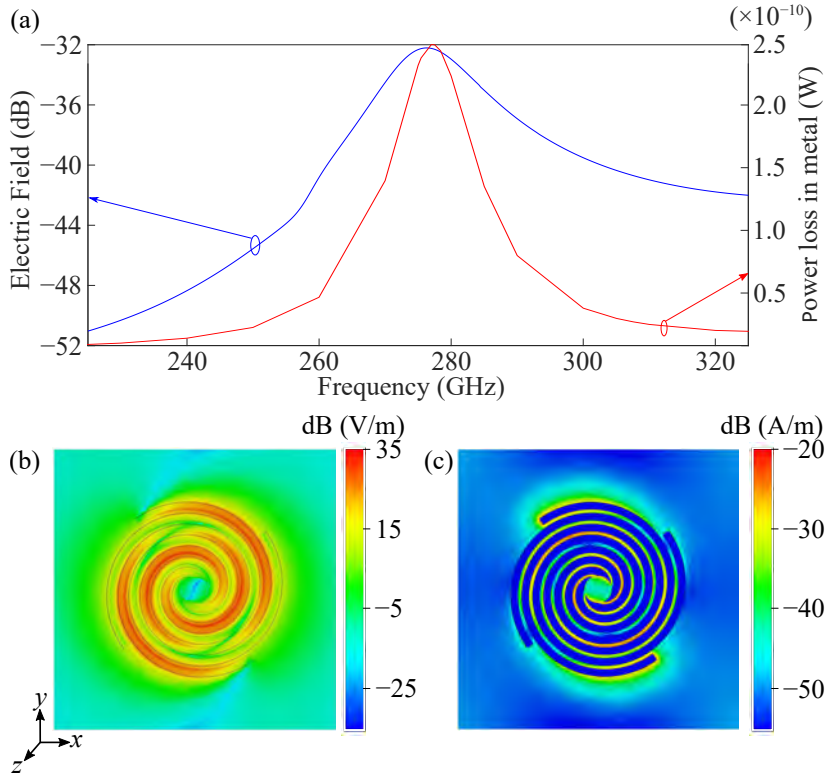

Figure 3.2. Electromagnetic simulation results. Electromagnetic response of the proposed terahertz bolometer. (a) Frequency-dependent electric field enhancement at the centre of the spiral, and frequency-dependent power loss in niobium metal including niobium spiral. (b) Electric field intensity, and (c) surface current profile at 277.5 GHz. The incident wave is linearly polarised and propagates in the $-z$-direction.

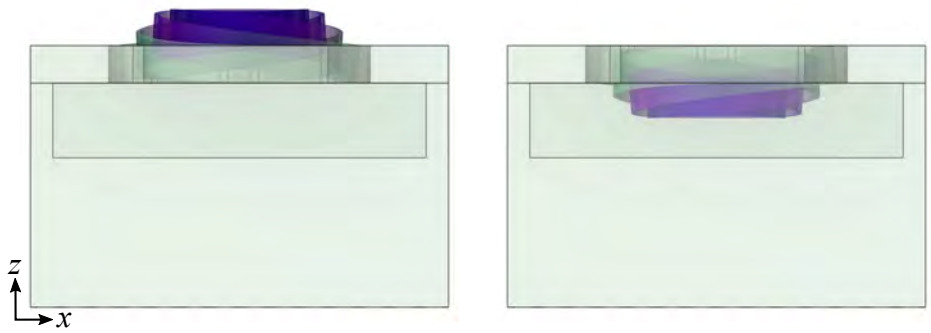

Figure 3.3. Simulated vibrational mode. COMSOL Multiphysics based simulated out-of-plane (up–down) vibrational mode of the niobium spiral structure at baseline mechanical resonance frequency of 12.20 kHz. Purple colour indicates the vertical displacement amplitude. The model includes the niobium spiral, COC substrate with an air gap, and the patterned gold reflector, accurately representing the full multilayer device geometry.

Next, the thermal response of the structure under terahertz illumination is investigated, using the time-dependent study in the heat transfer in solids module in COMSOL Multiphysics. Deposited beam power ranging from 0 to 1 mW is applied to the top of the niobium plate to imitate the heat generated through absorption. The corresponding temperature distributions at 0.1, 0.5, and 1 mW input power at equilibrium (0.2 seconds) are presented in Figure 3.4(a)–(c), respectively. Figure 3.4(d) shows the temperature at the spiral core with respect to various input powers, where the maximum temperature at the core varies from 293 to 328 K, from no input power to 1 mW of input power. The simulated heat maps exhibit a spatially uniform thermal distribution across the spiral arms, thereby minimising thermal stress and enabling uniform expansion throughout the spiral. This, in turn, promotes a coherent mechanical response and stable resonance frequency, allowing a predictable and repeatable transduction pathway essential for achieving high sensitivity and low noise in the bolometer.

Finally, this temperature profile with respect to input power is imported into the solid mechanics module to simulate the thermally induced mechanical resonance. The thermal conductivity and coefficient of thermal expansion are almost constant over the

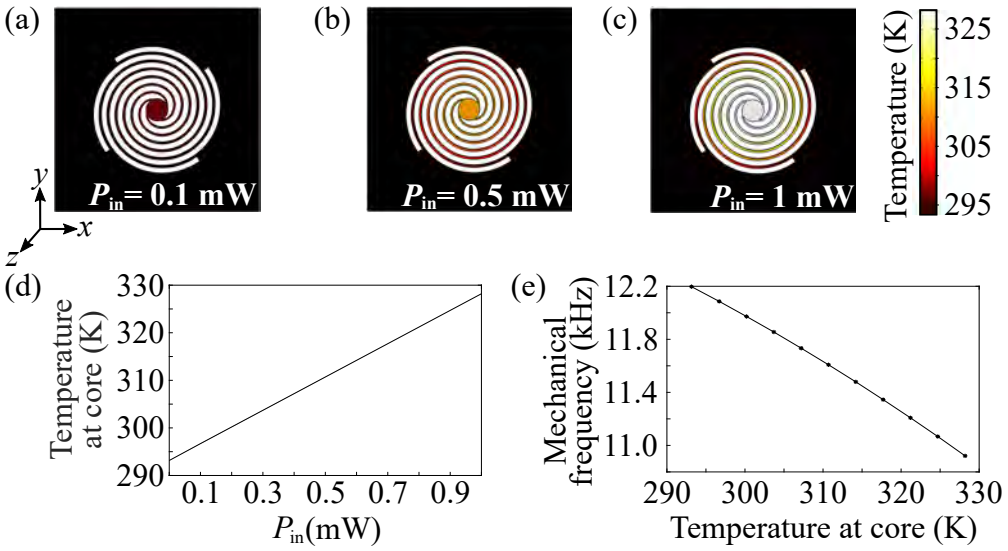

Figure 3.4. Thermomechanical simulation results. COMSOL Multiphysics simulation results illustrating the thermal and mechanical response of the niobium spiral bolometer. (a–c) Simulated heat maps showing temperature distribution at input powers of (a) 0.1 mW, (b) 0.5 mW, and (c) 1 mW, respectively. (d) Plot of input power, P_{in}, versus temperature at the core of the spiral, indicating a linear rise from 293 K to approximately 328 K. (e) Corresponding mechanical resonance frequency as a function of core temperature.

0–100°C range; however, the Young's modulus has a slight variation over temperature, which is described in Equation 1 (Bowling *et al.*, 2024).

$$E(T) = E_0 + M(T - T_0), \tag{3.1}$$

where E_0 is 105 GPa and $M = -0.011$. This equation is entered into COMSOL to define niobium properties. Finally, the temperature at the spiral core (T) is varied accordingly, and the corresponding mechanical resonance frequency is recorded. The corresponding temperature-induced mechanical resonance frequency is illustrated in Figure 3.4(e), where the resonance frequency decreases from approximately 12.2 to 10.9 kHz as the input power increases from 0 to 1 mW. This coupled multiphysics analysis depicts the overall working principle of the bolometer by showing the shift in mechanical resonance frequency influenced by the terahertz absorption.

3.3 Experiments and results

This section outlines the fabrication process, experimental setup, and performance analysis of the proposed MEMS-based terahertz bolometer. Similar to the simulation flow, two separate measurement setups are used, first to analyse the electromagnetic behaviour of the device, and the second to measure the absorption-induced mechanical response at the peak absorption frequency.

3.3.1 Fabrication

The bolometer device is fabricated in two separate parts, the first consists of the niobium spiral at the centre, with niobium spreading across the surrounding area, as shown in Figure 3.5(a). The second comprises a 300 µm-thick COC substrate with a centrally positioned air gap, attached to a gold backplane with periodic square apertures, as shown in Figure 3.5(b), also extended to match the lateral dimensions of the niobium plate. Additionally, both parts are fabricated with four bolt holes with high precision, such that by fastening them together with nuts and bolts, the spiral and the air cavity become completely aligned. Although the addition of dowel pins could further improve alignment accuracy, sufficient alignment is achieved using the precision-fabricated holes alone, without adding further fabrication and assembly complexity.

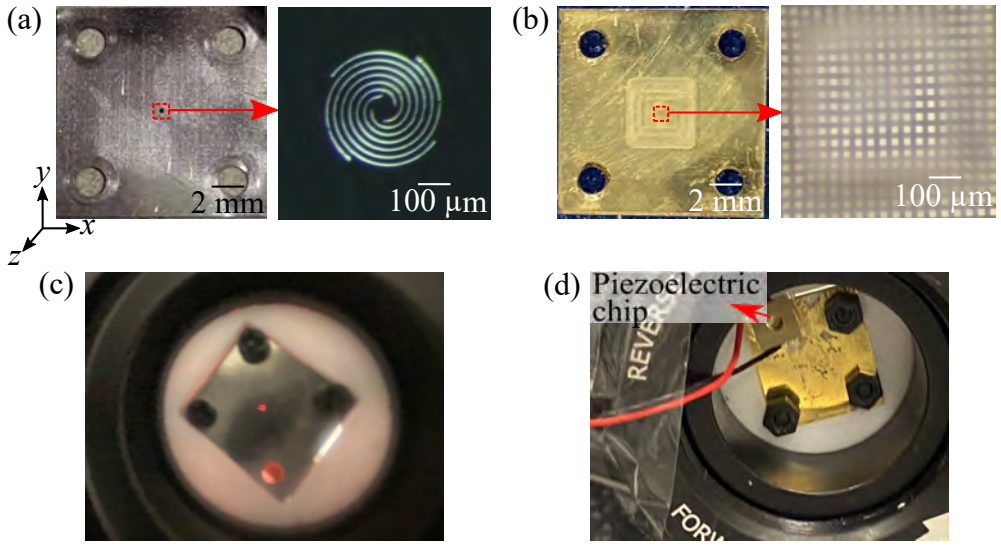

Figure 3.5. Device structure and integration. Fabricated sample and device assembly. (a) Fabricated niobium (Nb) spiral structure, showing the extended Nb plate and four screw holes with a microscopic view of the central spiral. (b) Optical image of the COC–gold plane with screw holes at corners and air-cavity at the centre, also showing a microscopic view of the periodic square apertured gold structure visible through the transparent COC. (c) Front view (Nb side) of the fully assembled device fastened with nuts and bolts and mounted onto a sample holder. (d) Backside view (gold side) of the assembled device, showing the mounted piezoelectric chip attached to one corner of the gold plane.

The spiral cuts in 50 µm thick niobium foil (Goodfellow) are produced by ultra-fast pulsed laser micromachining. The workstation for this is a microSTRTUCT-C (3D-Micromac AG), fitted with a Carbide femtosecond laser (Light Conversion), intelliSCAN galvos (Scanlab), and F=100 mm f-θ optics. As fine features of less than 15 µm are required, laser machining is performed with the second or fourth harmonic output from the laser (515 nm or 257 nm), with gentle laser parameters ($<$10 J/cm^2) and several repetitions to etch through the foil with minimal percussive forces or heat accumulation. Although the spiral is very accurately fabricated, some of the air gaps between adjacent spiral arms become bridged.

The other part consists of COC with gold patterns. The air cavity is formed by micro-milling the COC on a William Macodel 408MT using a range of standard and micro tooling. The parts are inspected using an Olympus Laser Confocal microscope (OLS5000). For the gold backplane, a thin adhesion layer is deposited on COC to support a thin

(∼1 μm) layer of gold on the back of the 300 μm thick COC. A 20 μm wide checkered feature is patterned on the gold layer using photolithography and lift-off.

The fully assembled device, consisting of the niobium plate and the COC–gold plane fastened together with screws and mounted onto the holder, is shown in Figure 3.5(c) and (d).

3.3.2 Terahertz response

To study the terahertz response, the fabricated device is illuminated by a wave produced using a vector network analyzer (VNA) through WR-3.4 extension modules operating over the 220–330 GHz range. A four-lens setup is used as shown in Figure 3.6(a), where lens 1 is used to collimate the incident wave, and the collimated wave is focused by lens 2 onto the sample. Lens 3 collimates the transmitted wave, which is then focused onto the receiver by lens 4. To determine the transmission reference, a measurement is taken without the sample, and for the reflection reference, the beam is focused onto bare niobium (reflectance $\approx$ 99.5%), which is then used to normalise the measured complex transmission and reflection spectra. Finally, the sample is placed at the centre with the beam focusing on the spiral, and the corresponding S-parameters, S_{11} and S_{21}, are measured. Appropriate time-gating is incorporated to mitigate multiple reflections from the setup, e.g., between the transmitter, receiver, the sample, and within each lens.

The terahertz beam is tightly focused with a 1250 μm spot size, and as the beam width exceeds the spiral's diameter of 360 μm, significant reflection appears from the surrounding niobium. However, the reflection reference from bare niobium compensates for the reflection from surrounding niobium, and the observed S-parameter primarily reflects the spiral's contribution. Since the spiral covers only a fraction of the beam cross-section, the absorbed power is contingent upon the local power density at the spiral structure, rather than the integrated beam power. The S-parameters measured by the VNA are used to compute the reflection, transmission, and absorption as shown in Figure 3.6(b). The absorption is calculated using the relation $A = 1 - |S_{11}|^2 - |S_{21}|^2$, where S_{11} and S_{21} represent the reflection and transmission coefficients, respectively.

The resulting absorption spectrum reveals a peak at around 278 GHz, indicating a good match with the simulated absorption peak of 277.5 GHz. However, a wider absorption bandwidth is observed from the absorption spectra as opposed to the design criteria of a narrowband absorber. This deviation is attributed to fabrication-induced imperfections,

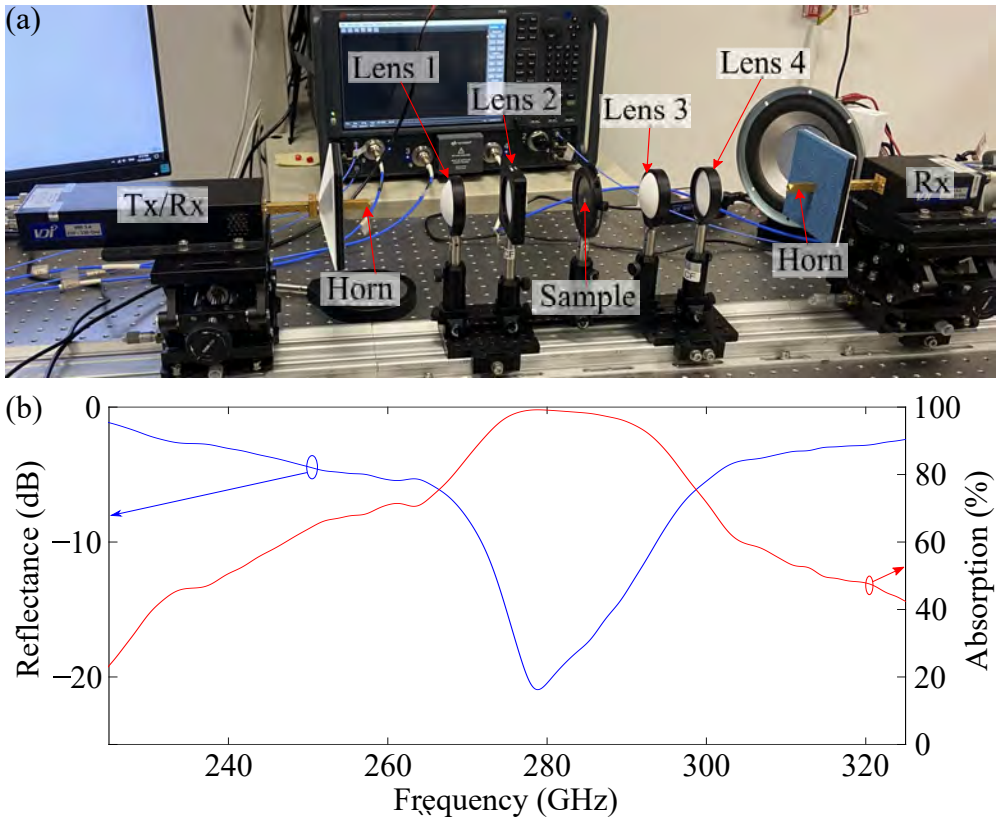

Figure 3.6. Electromagnetic measurement setup and response. Experimental setup and characterisation of terahertz response. (a) Measurement setup with four lenses and sample at the centre. (b) Measured electromagnetic response showing reflection and corresponding absorption across the 225–325 GHz range. Transmittance is below −100 dB and is therefore omitted for clarity.

such as bridging between spiral turns resulting in localised electrical shorting, and mechanical misalignment of the device. The leading cause of mechanical misalignment is that the niobium spiral fabricated on a thin foil is subject to slight bending or warping while handling and mounting. This can cause imperfect angular alignment between the absorber structure and the terahertz wave, hampering effective field coupling. All these combined cause the resonance frequency to slightly shift and exhibit a low electromagnetic Q-factor. However, the peak remains well within the intended WR-3.4 terahertz window. The agreement between simulation and measurement validates the electromagnetic design and confirms efficient terahertz absorption.

3.3.3 Mechanical response

Following the terahertz absorption characterisation, the mechanical response of the spiral is studied using laser Doppler vibrometry (LDV). The setup, as shown in Figure 3.7(a), presents the terahertz illumination consisting of a microwave signal generator coupled with a WR-3.4 frequency extender to provide a variable power of 278 GHz terahertz wave. This terahertz signal undergoes a two-lens setup to finely focus the terahertz wave onto the niobium spiral. The other side of the measurement setup uses the LDV to probe mechanical vibrations of the niobium spiral through the semi-transparent square-apertured gold plane. The sample is fastened together and mounted to a holder, and a piezoelectric chip is mounted to the rear side of the sample (gold), as shown in Figure 3.5(d). This piezoelectric chip producing out-of-plane displacement is driven by a signal generator providing a frequency sweep from 1 kHz to 25 kHz to excite the mechanical resonance frequency. Initially, the baseline mechanical resonance frequency of the device is measured without the influence of a terahertz wave. Thus, the terahertz source is turned off (0 mW), while the LDV shines a laser through the rear of the device, and the piezoelectric chip excites the mechanical resonance frequency. The spiral exhibits a baseline mechanical resonance frequency of 12.25 kHz, which closely matches the simulated natural mechanical resonance frequency of 12.20 kHz. The quality factor of the MEMS resonator with no terahertz illumination at the mechanical resonance frequency is calculated to be around 43.

Afterwards, the bolometric response is evaluated under active terahertz illumination with the terahertz source turned on. The terahertz radiation at the measured absorption peak frequency (278 GHz) is directed onto the spiral absorber with tunable power levels from 0 to 0.9 mW in 0.1 mW steps. The mechanical resonance frequency is measured at each power level. With increasing terahertz power, the mechanical resonance frequency exhibits a red shift, as shown in Figure 3.7(b), which shows a mechanical frequency shift from 12.25 kHz to 11.17 kHz over the tested power range. The sharp peak at 1 kHz originates from the initial excitation of the piezoelectric chip actuating at that frequency, i.e., drive resonance. The prominent vibration peaks observed above the fundamental resonance are attributed to higher-order mechanical modes. COMSOL Multiphysics eigenfrequency simulations under zero terahertz illumination predict resonant modes at 12.2, 13.2, 16.4 and 22.6 kHz. The 12.2 kHz mode corresponds to the dominant fundamental out-of-plane flexural vibration of the suspended spiral and agrees well with the measured resonance at approximately 12.25 kHz. The 13.2 kHz

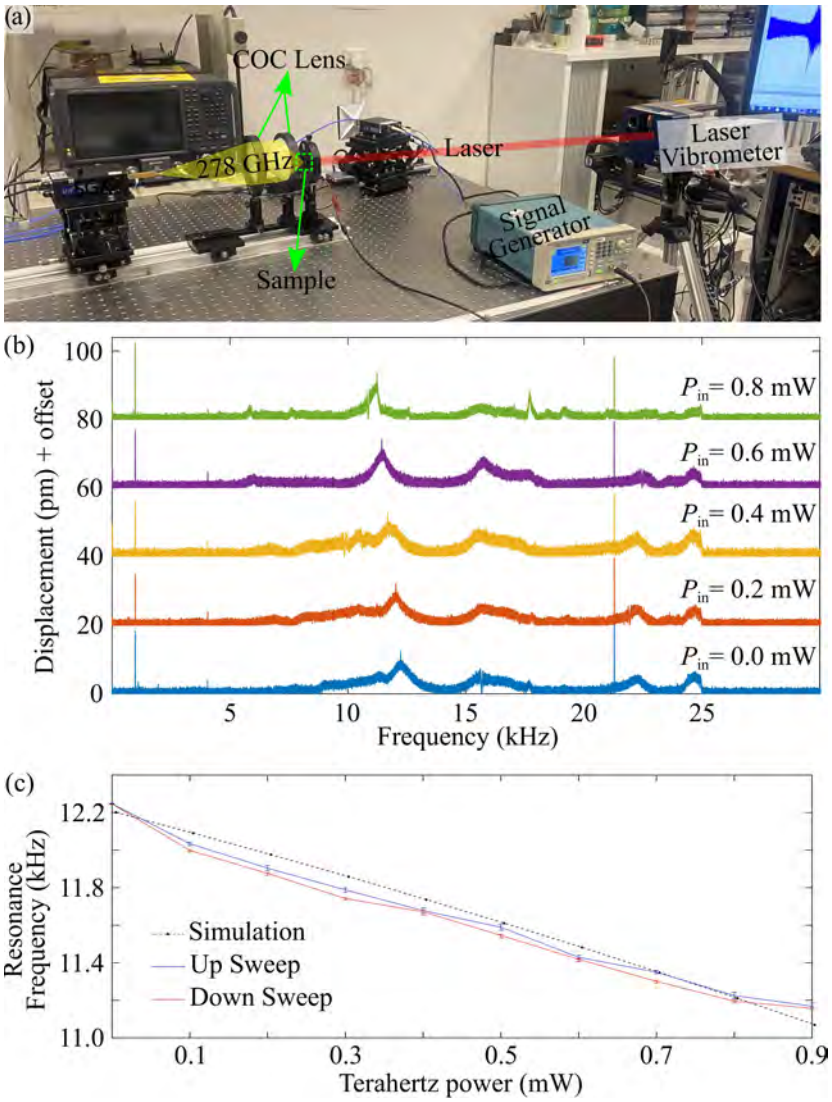

Figure 3.7. Mechanical measurement setup and response. Experimental setup for characterisation of the mechanical response. (a) Measurement setup with a continuous terahertz wave at 278 GHz incident from the SGX to the niobium spiral. On the opposite side, a laser beam from the LDV is incident to the spiral through the patterned gold and COC. Signal generator is connected to the piezoelectric chip to excite mechanical resonance. (b) Measured out-of-plane displacement spectra of the niobium spiral bolometer under increasing terahertz power levels (0 to 0.8 mW), acquired using laser Doppler vibrometry. Each curve is vertically offset for visual clarity. No vibrational response is observed beyond 25 kHz due to the 1–25 kHz range of the piezoelectric chip excitation. (c) Simulated and measured resonance frequency as a function of incident terahertz power, showing both measured up-sweep and measured down-sweep trends. Each measured point has error bars from five separate readings.

mode corresponds to a torsional mode, where opposite sides of the structure undergo opposite out-of-plane displacements, resulting in a relatively small net out-of-plane vibration at the centre of the spiral. The 16.4 and 22.6 kHz mode corresponds to higher-order out-of-plane flexural modes with a smaller vibration amplitude than the fundamental mode. These simulated resonant modes are also reflected in the measured frequency response, confirming that the resonance near 12.2 kHz is the dominant sensing mode, while the higher-frequency peaks arise from higher-order mechanical resonances. In Addition, the consistent strong peak around 21 kHz denotes the frame resonance, mainly from the small 3D-printed COC holder. The other small vibrations across the frequency range are the background noise from the measurement setup or the environment.

To further assess the repeatability and thermal stability, two sets of five independent resonance measurements were conducted, one with increasing terahertz power from 0 to 0.9 mW, and the other with decreasing power from 0.9 mW back to 0 mW in 0.1 mW steps. The resulting mechanical resonance frequency at various terahertz power levels is shown in Figure 3.7(c), which demonstrates quasi-linear behaviour, implying high repeatability and reversibility, suggesting that the structure does not endure permanent deformation due to the stress. The minimal standard deviation among the five measurements verifies the consistency and accuracy of the measurement. Note that all measurements mentioned above are performed in ambient air and at room temperature. For consistent bolometric detection, the beam alignment and spot size are kept identical to calibration conditions to ensure repeatable power density at the spiral absorber. However, if the spot size or alignment varies, recalibration enables accurate power measurement for the specific measurement condition. The close agreement between simulation and experiment in Figure 3.7(c) confirms the accuracy of the multiphysics model and validates the thermal-to-mechanical transduction mechanism.

The evident red shift of the mechanical resonance frequency with respect to elevated power levels is caused by the thermally induced softening of the spiral owing to localised heating from terahertz absorption. The maximum observed shift in mechanical frequency from 0 mW (12.25 kHz) to 0.9 mW (11.17 kHz) is 1080 Hz, corresponding to a thermomechanical responsivity, R, of 1200 $\mathrm{Hz{\cdot}mW^{-1}}$, assuming an almost 100% absorption efficiency and thermal conductance of $2 \times 10^{-5}\,\mathrm{W{\cdot}K^{-1}}$.

This thermomechanical responsivity is achieved due to the geometry and several thermomechanical effects. With the temperature increasing from 293 K to approximately

328 K, the Young's modulus of niobium decreases slightly, and the spirals expand due to thermal expansion. Given the change in Young's modulus within 35 K is around 1–2%, the change in mechanical resonance frequency based on this alone would be rather modest. However, due to the constrained geometry, compressive thermal stress plays a dominant role. As the niobium spiral arms start to expand due to heat, they are obstructed by their constrained geometry at both the centre and the outer edge. This restriction builds up compressive stress along the arms and drastically lowers the bending stiffness. Additionally, the ultra-narrow spiral arms of 7 μm amplify this effect by increasing the mechanical flexibility of the spiral, thus undergoing a significant shift in stiffness under small stress. These combined effects reduce the bending stiffness significantly and thus result in a noticeable red shift in mechanical resonance frequency.

The maximum measured power of 0.9 mW is limited by the safe operation of the terahertz source used. The ideal maximum power that the mechanically constrained spirals can tolerate directly depends on the maximum temperature the structure can handle. The ideal bearable maximum temperature above room temperature, ΔT, can be calculated from

$$\Delta T = \frac{\sigma_{\text{yield}}}{E_0 \alpha}, \tag{3.2}$$

where σ_{yield} is the yield strength of 240 MPa, and α is the thermal expansion coefficient of 7.2×10^{-6} K^{-1}. The equation indicates that the device can ideally handle almost 317 K above room temperature. However, several factors, such as fabrication-induced residual stress, thermal cycling effects, and the ultra-narrow 7 μm spiral arms, can significantly limit the maximum tolerable power before the structure tends to undergo permanent deformation or breakdown. Thus, a practical maximum temperature estimation is 400 K, which leads to approximately 3 mW of incident terahertz power, assuming a linear relationship between temperature rise and incident power, as suggested from the simulation shown in Figure 3.4(d).

The thermomechanical responsivity also directly impacts the minimum resolvable power, as higher responsivity can detect very small changes in terahertz power. The minimum resolvable power also depends on the frequency resolution of the LDV, f_{LDV}. As the frequency resolution of the LDV used is below 1 Hz, the minimum resolvable power can be calculated using $P_{\text{min}} = f_{\text{LDV}}/R$. From the equation, the minimum resolvable power is calculated to be 0.833 μW. However, the minimum detectable power also depends on the noise performance. To study the noise performance of the proposed bolometer, the noise spectral density (NSD) is measured at the mechanical

resonance frequency of 12.25 kHz under no terahertz illumination. Here, the NSD characterises frequency jitter in the resonator, derived from the instantaneous frequency fluctuations of the spiral. The instantaneous frequency around 12.25 kHz is extracted by differentiating the unwrapped instantaneous phase of the displacement–time signal from the vibrometer via Hilbert transform, and Welch's method is applied to calculate the power spectral density (PSD), whose square root yields the NSD in $\mathrm{Hz}\cdot\mathrm{Hz}^{-0.5}$. Since the NSD is a spectrum describing the distribution of jitter power around resonance, the maximum value of 11.4 $\mathrm{Hz}\cdot\mathrm{Hz}^{-0.5}$ is taken as a conservative figure of merit. From the NSD and the experimentally determined thermomechanical responsivity, $R = 1200\ \mathrm{Hz}\cdot\mathrm{mW}^{-1}$, the NEP is calculated using $\mathrm{NEP} = \mathrm{NSD}/R$. The maximum NEP is found to be $9.52\,\mu\mathrm{W}\cdot\mathrm{Hz}^{-0.5}$, indicating a minimum detectable terahertz power in a 1 Hz bandwidth. Since the minimum detectable power limited by the NEP is higher than the minimum resolvable power, the practical lower bound for power detection under standard conditions is 9.52 μW.

Although this NEP is relatively high compared to some of the literature discussed above, this level of NEP is still within a reasonable limit for a practical bolometer. One contributing factor for the modest responsivity and elevated NEP in this work is linked to the antenna's sub-wavelength dimension and its partial coverage of the incident beam, resulting in limited energy absorption. Moreover, similar to other works that have demonstrated much lower NEP under vacuum conditions, the performance of this device is also expected to improve in vacuum by limiting convective heat loss and air damping, thereby lowering the NEP and enhancing sensitivity. For non-ideal operating conditions, the system must remain mechanically stable, shielded from external airflow to avoid disturbance of the MEMS structure, and maintained at surrounding temperatures below approximately 320 K to prevent thermal drift or material stress. If environmental conditions deviate from room temperature and ambient air, recalibration of the device may be required.

A comparative overview of the key performance metrics and design aspects between the proposed bolometer and existing bolometers reported in the literature is presented in Table 3.1. While prior works demonstrate lower NEP, they usually utilise vacuum operation (Zhang *et al.*, 2019; Liu *et al.*, 2022; Vicarelli *et al.*, 2022; Zhang *et al.*, 2024), electrical readouts (Cherednichenko *et al.*, 2011), photodiode detection (Froberger *et al.*, 2022; Belacel *et al.*, 2017), optical microscopy (Zhu *et al.*, 2022), or phase-locked loop

Table 3.1. Performance comparison of terahertz room temperature bolometers. Comparison of key performance metrics, design strategy, and measurement conditions with other reported terahertz room temperature bolometers.

Structure	Readout & detector type	Detection Frequency (THz)	Responsivity (W^{-1})	NEP ($pW.Hz^{-0.5}$)	Environment (Room temperature)
Au spiral antenna with YBCO microbridge (Cherednichenko *et al.*, 2011)	Thermoresistive	0.33	15 μV	450	Ambient air
NiCr absorber on GaAs MEMS resonator (Zhang *et al.*, 2019)	Thermomechanical (Phase-locked loop)	0.25	39.3 Hz	500	Vacuum
Bi-layer MEMS microcantilever (Froberger *et al.*, 2022)	Thermomechanical (Optical, photodetector)	2.5	150 pm	2×10^4	Ambient air
Bi-material microcnatilever with absorber (Zhu *et al.*, 2022)	Thermomechanical (Optical, microscope)	3.4	24.8 μm	38.2 (simulated)	Ambient air
SRR meta-atom with suspended cantilever (Belacel *et al.*, 2017)	Thermomechanical (Optical, photodetector)	2.7	50 pm	1.6×10^4	Ambient air
Bimaterial nanobeam with terahertz absorber (Liu *et al.*, 2022)	Thermomechanical (Phase-locked loop)	2.5	21 MHz	Not stated	Reduced pressure (1 mbar)
SiN membrane resonator with metamaterial absorber (Zhang *et al.*, 2024)	Thermomechanical (Phase-locked loop)	2.0	15 Hz	36	Vacuum
Cr–Au on Si_3N_4 trampoline membrane (Vicarelli *et al.*, 2022)	Thermomechanical (Interferometry)	0.140	75 mHz	100	Vacuum
NiCr absorber on silicon-on-insulator platform (Zhang *et al.*, 2025a)	Thermomechanical (Piezoresistive)	1–10	123 Hz	36	Ambient air packaged
This work	Thermomechanical (LDV)	0.278	1.2 Hz	9.52×10^6	Ambient air

circuitry (Zhang *et al.*, 2019; Liu *et al.*, 2022; Zhang *et al.*, 2024), which elevates the system complexity. Moreover, several prior works do not report the terahertz absorption spectra (Zhang *et al.*, 2019; Vicarelli *et al.*, 2022; Zhang *et al.*, 2025a), and in most other cases, the terahertz absorption efficiency is not accounted for. Thus, the detected power reflects only the power absorbed by the device, and not the actual power impinged on the structure. In contrast, the proposed device exhibits near-unity terahertz absorption at the detection frequency, providing a direct and consistent correlation between the illuminated power density and the detected power. Additionally, the proposed design

also delivers competitive responsivity under room temperature and ambient air conditions without external circuitry, thereby balancing simplicity, integration, and practical operation with acceptable overall performance.

3.4 Conclusion

This chapter has demonstrated an antenna-coupled MEMS-based terahertz bolometer that utilises laser vibrometry for non-contact, high-resolution optical readout of thermally induced resonance shifts. This eliminates the need for integrated electrodes, biasing, or on-chip electronics, which simplifies integration and reduces parasitic noise. The device integrates a spiral-shaped niobium antenna that enables efficient and linear polarisation-insensitive terahertz absorption, spatially uniform thermal distribution, and high-sensitivity mechanical response under room-temperature conditions. The niobium spiral sits over a COC substrate and a micromachined air cavity that ensures low thermal conductivity, mechanical stability, and unhindered mechanical vibration, while also allowing the laser to pass through the patterned checkered gold reflector from the back side, minimising alignment complexity. Experimental results confirm a precise and repeatable downshift in mechanical resonance frequency from 12.25 kHz to 11.17 kHz as the incident terahertz power increases from 0 to 0.9 mW. The observed thermomechanical responsivity of 1200 $\mathrm{Hz{\cdot}mW^{-1}}$ is consistent with theoretical estimates based on thermal expansion and stress softening. The compact design, passive operation, frequency-selective near-unity narrowband terahertz absorption, and broadband optical readout highlight the potential of this platform for scalable terahertz sensing, spectrometry, and imaging applications. Additionally, the unification of a terahertz absorber, thermal transducer, and mechanical resonator into a single spiral structure helps to elevate the transduction efficiency of the device response. Future work will focus on device packaging for environmental isolation, reducing the NEP through structural optimisation, widening the operation band of the detector, and exploring hybrid readout schemes combining photonic and electronic modalities.

Chapter 4

Compact Terahertz Spectrometer

(Original Content)

TERAHERTZ spectroscopy is of considerable interest due to the abundance of molecular and atomic fingerprints within this spectral region, empowering advanced applications in material science, biology, security screening, and astronomy. Conventional terahertz spectroscopic systems are often bulky, mechanically complex, and impractical for compact integration. However, numerous spectroscopic applications require compact, passive, and easily deployable systems. To address this demand, we present a compact terahertz spectroscopic system based on a phase-gradient metasurface and a focusing lens. The metasurface implements a one-dimensional sawtooth-like phase gradient to generate frequency-dependent angular deflection across the 270–330 GHz band. The deflected beams are subsequently converted into spatially separated focal spots using a designed aspheric focusing lens, enabling direct frequency-to-space mapping. The spatially separated beams are captured using a terahertz camera, enabling single-shot spectral detection without mechanical scanning. The system operates in the sub-terahertz regime and achieves spatial focusing over a 16.8-mm-wide focal plane, within which the majority of the operating band is effectively resolved. The results demonstrate frequency-to-space mapping across the operation band, thus corroborating the system as a feasible, compact, passive terahertz spectrometer suitable for portable applications.

4.1 Introduction

Spectroscopy at terahertz frequencies play a crucial role as the energy level of terahertz waves closely matches the energy of molecular rotation, intermolecular vibration, and excitation of several elements. In astronomy, terahertz spectroscopic study helps to probe the evolution of the galaxy and understand the formation of stars in the early universe (Taniguchi *et al.*, 2022; Risacher *et al.*, 2016). Beyond astrophysical applications, spectroscopic observation at the terahertz band is equally significant for material science, biology, chemistry, and many other fields, as they introduce a multitude of molecular and atomic transitions occurring in this spectral region (Wietzke *et al.*, 2010; Plusquellic *et al.*, 2007; Baxter and Guglietta, 2011). All these combined have enabled terahertz spectroscopy to emerge as the front-runner of terahertz sensing technologies, as it provides unique capabilities in interrogating molecular structures, detecting concealed objects, and analysing biomolecular structures.

Terahertz spectrometers are well established and are typically based on time-domain spectroscopy (THz-TDS), Fourier-transform spectrometry, or heterodyne receiver architecture. These methods provide very high spectral resolution and sensitivity. However, they require bulky optical assemblies, mechanically scanned components, or complex signal processing. In addition, these systems rely on controlled excitation sources, such as pulsed lasers or local oscillators, and therefore cannot operate with arbitrary or uncoordinated input signals. Moreover, several practical applications, such as industrial quality control (Zeitler *et al.*, 2007; Shen, 2011), security screening (Federici *et al.*, 2005), on-site non-destructive testing (Jackson *et al.*, 2011; Walker *et al.*, 2013), and communications systems analysis, typically emphasise compact, robust, and real-time spectral discrimination over extreme spectral resolution or high sensitivity. Therefore, in many cases, moderate frequency resolution is sufficient, where compactness, mechanical stability, and ease of deployment are the primary design considerations. These needs necessitate the exploration of a substitute spectrometer design that facilitates frequency discrimination while utilising a simple, compact, and passive configuration.

Conventionally, the low to medium resolution spectrometers were realised using diffraction grating-based structures (Ji *et al.*, 2025), or dispersive optics (Headland *et al.*, 2020). These structures caused multiple diffraction orders and typically operated in reflective, off-axis configurations optimised for specific incidence angles to maximise the diffraction efficiency (Luo *et al.*, 2026). These enhance the alignment complexity and system footprint. A typical grating-based spectrometer is shown in Figure 4.1(a), incorporating

a grating and a reflective focusing lens. This complicated the setup and may introduce unwanted interference between incident and reflected beams from the focusing mirror. A solution for this was presented in the work by Luo *et al.* (2026), showcasing a grating-based spectrometer as shown in Figure 4.1(b). This utilised two transmissive metasurfaces to collectively function as a focusing lens. Using two metasurfaces introduced additional complexity and impacted the overall efficiency. Moreover, a reflective grating distributed the power among multiple diffraction orders, thus hampering total efficiency. As an alternative, metasurfaces with their immense advantages and ultrathin profile can help solve these issues. Phase-gradient metasurfaces enable strong dispersion while suppressing higher diffraction orders, and can operate under normal incidence and in transmission mode. Although a spectrometer based on a reflective metasurface was presented by Ji *et al.* (2025) to achieve higher efficiency and broader bandwidth (Zheng *et al.*, 2015; Arbabi *et al.*, 2017), they still required strict oblique incidence angles, which complicates the setup compared with transmissive systems that operate under normal incidence, as shown in Figure 4.1(c).

Phase-gradient metasurfaces employ a spatially varying phase response throughout the surface, enabling frequency-dependent angular deflection of incident waves. In such structures, a linear phase ramp across the surface maps different frequencies into distinct propagation directions through the well-known beam-squint effect, thereby enabling spectral separation. Compared with conventional diffraction gratings, metasurfaces provide additional design flexibility and can be engineered to suppress higher diffraction orders, improving the transmission efficiency of the desired deflected beam. By combining a phase-gradient metasurface with a focusing element, the angularly dispersed beams can be converted into spatially separated focal spots at a detector plane, enabling single-shot spectral measurements without mechanical scanning or time-domain reconstruction.

In this chapter, a compact terahertz spectrometer based on a transmissive phase-gradient metasurface and a focusing lens is presented for spatial spectral mapping onto a terahertz camera. The system operates across the 270–330 GHz band and is designed for integration with the MICROXCAM-384i terahertz camera from the Institut national d'optique (INO). A trilayer transmissive metasurface with eight phase quantisation levels is designed and simulated in CST Microwave Studio to generate a linear phase gradient and achieve efficient frequency-dependent beam deflection while suppressing unwanted diffraction orders. The deflected beams are subsequently focused using a

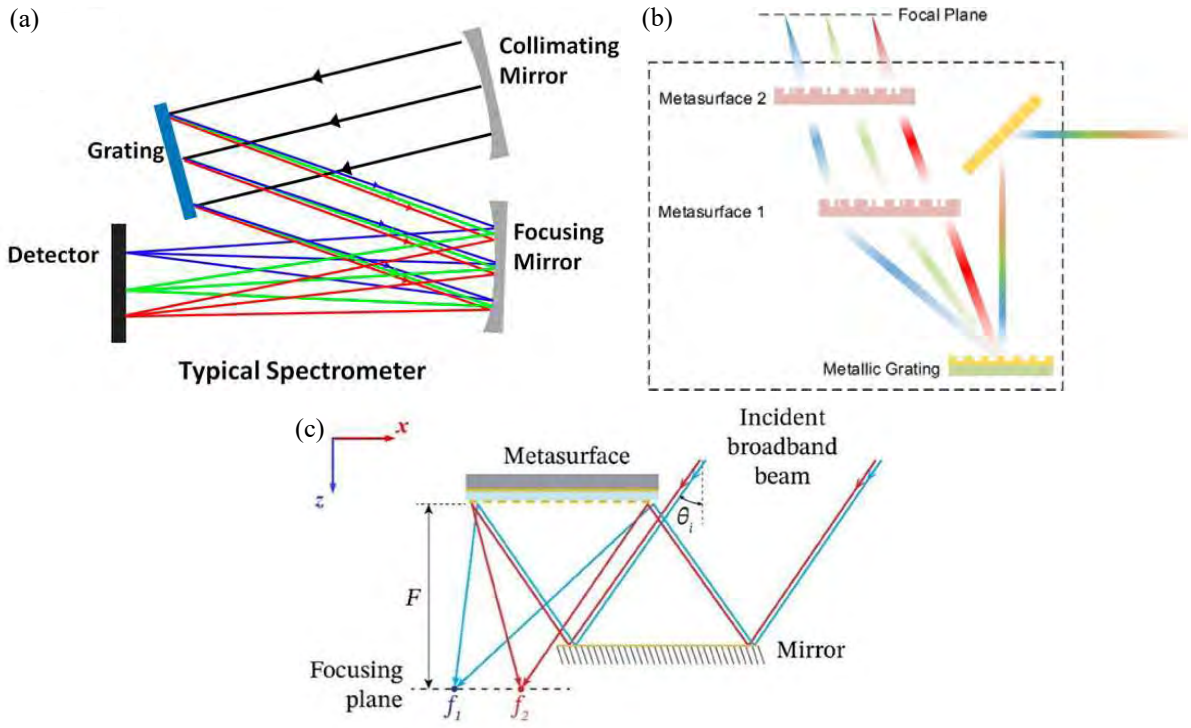

Figure 4.1. Spectrometer architectures. Schematic illustrations of conceptual spectrometer architectures in literature. (a) Conventional grating spectrometer with focusing mirror. Adopted from Zhu *et al.* (2017). (b) Compact terahertz metasurface spectrometer with metallic diffraction grating and two off-axis metasurface lenses. Adopted from Luo *et al.* (2026). (c) Single-element reflective metasurface spectrometer providing frequency-dependent angular deflection and focusing for direct frequency-to-space mapping. Adopted from Ji *et al.* (2025).

designed aspheric biconvex lens, which is simulated, fabricated through 3D printing, and experimentally characterised to project the angularly dispersed beams onto the camera focal plane. The combined transmissive metasurface–lens module reduces mechanical complexity through an inline architecture and forms a detachable, compact device capable of converting a terahertz camera into a passive spectrometer.

4.2 Metasurface design

Phase-gradient metasurfaces are widely used for beam control and beam-forming applications, including beam deflection (Headland *et al.*, 2018). A one-dimensional linear phase ramp imposed across the metasurface steers the outgoing beam at a specific angle, with the deflection direction determined by the slope of the phase gradient, as illustrated in Figure 4.2. Each unit cell introduces a discrete phase shift, and together

the array forms an effective linear phase distribution. Due to phase wrapping, the phase profile repeats every 2π, producing a periodic sawtooth-like phase function. The spatial period of this phase ramp, denoted as D, corresponds to the super unit cell or a sub-array length and is defined as $D = Np$, where p is the unit cell period, and N is the number of phase quantisation levels required to realise a 2π phase cycle. As a result, phase-gradient metasurfaces behave similarly to diffraction gratings and, under normal incidence, can be described using the following relation,

$$D \sin\theta = m\lambda, \tag{4.1}$$

where θ is the angle of the outgoing beam with respect to the normal direction, m is the diffraction order, and λ is the wavelength of the incoming wave. The number of supported diffraction orders is governed by the condition $|m\lambda/D| \leq 1$, which depends on the choice of the supercell period D. When the operating wavelength range satisfies $D/2 < \lambda < D$, only the zeroth and first diffraction orders ($m = 0, \pm 1$) can propagate, while higher orders are suppressed. This ensures predominantly single-order beam deflection. Since λ is a variable, for a fixed D and phase gradient function, the directionality of the wave is dependent on frequency, which is denoted as beam squint and forms the basis for frequency-dependent wave separation.

Levels of phase quantisation play an important role in the overall performance and suppressing higher diffraction orders. For beam deflection, it has been investigated that quantisation levels of four and above clearly provide the desired functionality, while more quantisation levels help to reduce aberrations (Headland *et al.*, 2018). In this

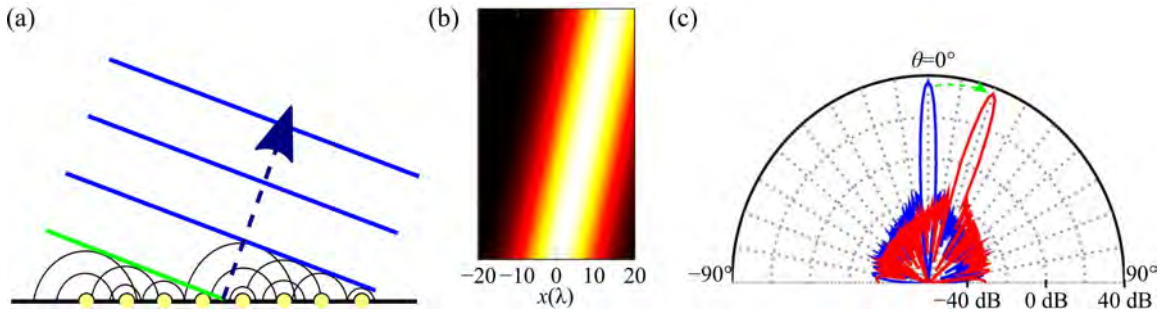

Figure 4.2. Phase gradient beam deflection. Illustration of angular beam deflection using phase control. (a) Huygens'-principle diagram for beam deflection. (b) Corresponding propagation beam deflection, and (c) far-field radiation pattern produced (red), showing a beam deflected from plane wave propagation (blue). Adopted from Headland *et al.* (2018).

design, the operating frequency range of 270–330 GHz corresponds to wavelengths from 1110 to 908 μm. Since the deflection angle follows the diffraction relation $\sin\theta = \lambda/D$, the spatial period D should be chosen close to the largest wavelength to maximise angular variation across the operating band. Since the supercell period, D, depends on the unit cell period, p, and the number of phase quantisation levels, N, subwavelength unit cells ($p < \lambda_{\text{min}}/2$) are maintained while keeping D close to the largest wavelength. Based on these constraints, eight phase quantisation levels are selected. This provides a practical balance between reduced phase aberrations and sufficient beam deflection variation across the operating band.

4.2.1 Unit cell design and results

Eight different unit cell designs are established such that the transmission magnitude of each cell is close to unity and the phase increment is approximately 45° between adjacent elements. The periodicity of each unit cell, p, is selected to be 154 μm, such that the periodicity is in the subwavelength scale to avoid diffraction. This leads to a super unit cell periodicity D of 1232 μm, which is slightly above the largest wavelength of the targeted operation frequency band. Figure 4.3(a) presents the tri-layer metasurface design strategy incorporating orthogonal gold wire-grids as the two outer layers with a middle resonator layer to introduce phase variation. The two outer metallic layers are separated from the middle resonator layer by 65 μm thick cyclic olefin copolymer (COC) substrates. The three metallic layers are shown in Figure 4.3(b)–(d).

The middle resonant layer converts the linear polarisation into an elliptical state due to the different phase responses from the orthogonal eigenmodes supported by the anisotropic structure. This elliptical state generates a cross-polarised output (Grady *et al.*, 2013). The orthogonal non-resonant wire grid on the other side of the trilayer structure only permits transmission of the cross-polarised waves and blocks the co-polarised waves. The initial non-resonant wire grid only allows the co-polarised waves to pass through while blocking any cross-polarised waves. Each time waves pass through the anisotropic middle layer, slight polarisation conversion occurs, and most waves passing through the final wire grid emerge as a cross-polarised wave. This ensures strong polarisation conversion of the transmitted waves, and through engineered substrate thickness, the co-polarised reflection can be minimised through destructive interference from the multiple reflections, thereby improving overall conversion efficiency. It should

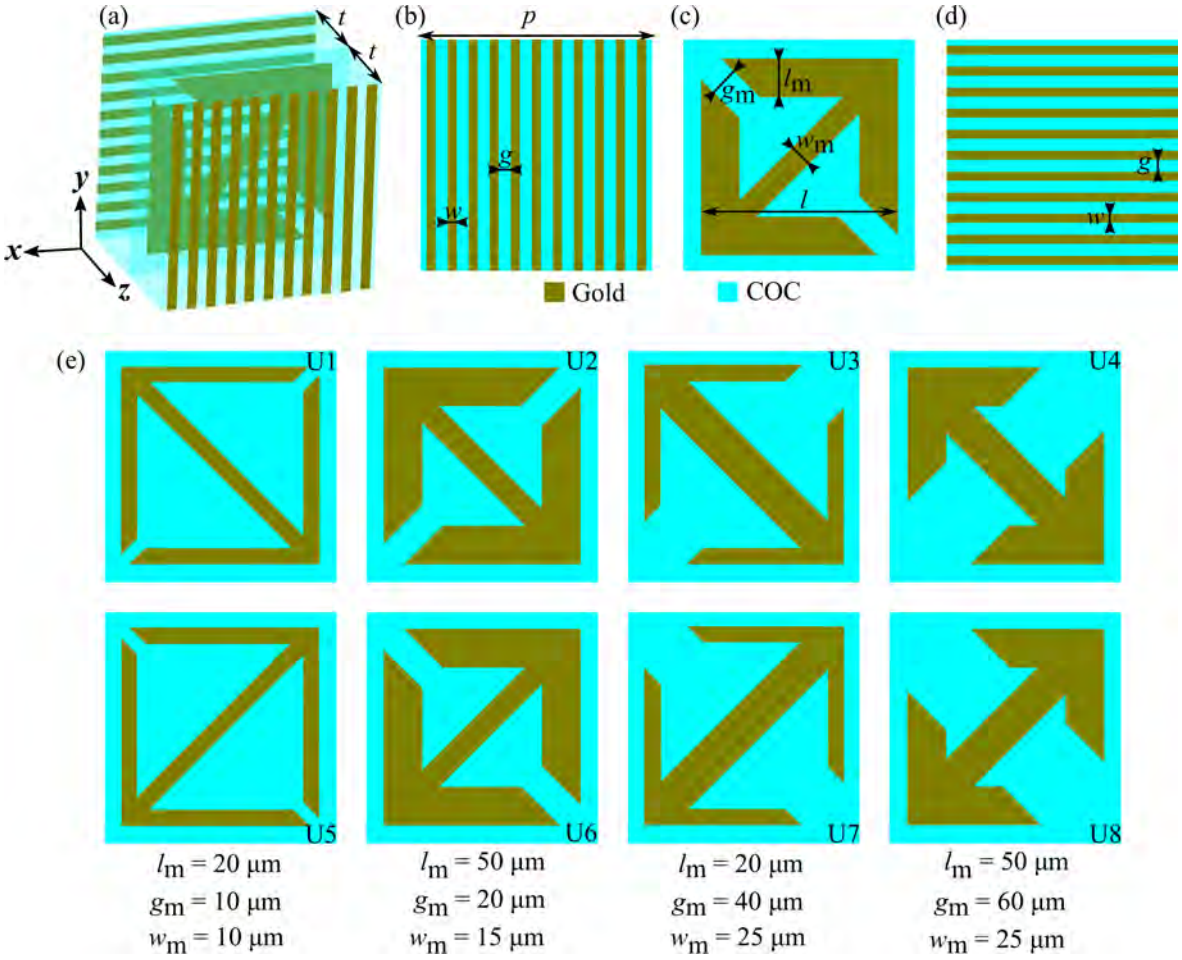

Figure 4.3. Unit cell design architecture. Schematic diagram of a unit cell. (a) Unit cell 3D view, (b) front wire-grid layer, (c) middle resonant layer, and (d) back wire-grid layer. The geometric parameters of the design are $t = 65$ μm, $w = 6$ μm, $g = 8$ μm, $l = 130$ μm, and $p = 154$ μm. The parameters l_m, w_m, and g_m are variable to control the output phase. (e) Designs and the parametric variations of the middle resonator used to control phase response. Metallic resonators are made of gold to minimise metal loss and the substrate is cyclic olefin copolymer (COC) with a relative permittivity $\epsilon_r = 2.34$ and loss tangent $\tan\delta = 0.0005$. U1–U8 denote the different middle resonant structure designs, where U5–U8 are the mirror images of U1–U4 about the vertical axis, respectively.

be noted that this condition is frequency-dependent, and operation at a different frequency would generally require re-optimisation of the substrate thickness, and mostly the periodicity.

The middle-layer resonators are selected to achieve specific phase shifts along with polarisation conversion. Different transmission phases can be achieved by varying the geometry. Here, eight different resonators are realised, as shown in Figure 4.3(e). The

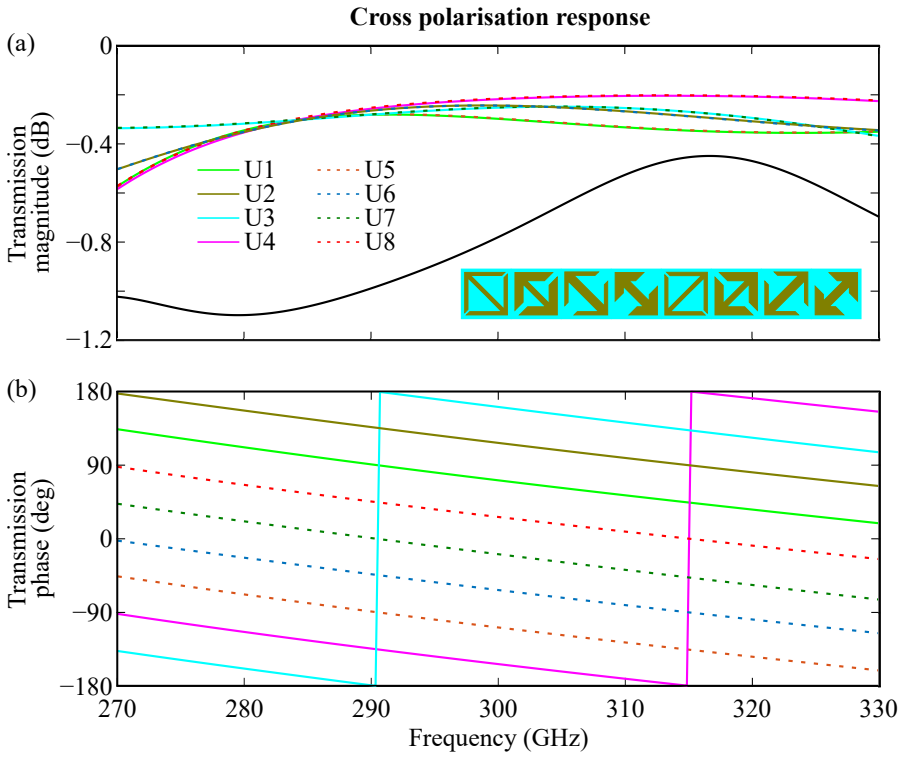

Figure 4.4. Unit cell transmission. Cross-polarised transmission of the eight individual elements. (a) Magnitude, and (b) phase. The labels U1–U8 refer to the unit cells illustrated in Figure 4.3(e). Unit cells with identical transmission magnitudes share the same geometrical parameters and are mirror symmetric about the vertical axis, resulting in a 180° transmission phase shift. The black solid curve in (a) shows the simulated first-order cross-polarised transmission magnitude of the super unit cell formed by arranging the eight elements horizontally to provide a full 2π phase coverage. The inset in (a) illustrates the arrangement of the eight unit cells within the super unit cell.

wire grids and the middle resonant layer are made of gold to minimise metal loss, and the COC substrate is selected due to its low-loss properties in the terahertz regime.

Each unit cell structure is designed through full-wave simulations in CST Microwave Studio under unit cell boundary conditions and plane-wave excitation. The cross-polarised transmission magnitudes and phases are presented in Figure 4.4. It can be seen that the transmission magnitudes of the eight individual elements are above -0.6 dB, indicating an efficiency of above 93% for the whole operation band. Furthermore, the phase response of the elements, as shown in Figure 4.4(b), shows a smooth linear-like phase gradient with 45° phase step among all elements. The eight elements with 45° phase increment enable covering the full 2π tunability range at a given frequency and thus allowing beam control functionality through array-level consideration.

4.2.2 Array-level design and results

The eight elements are then arranged horizontally to form a super unit cell that provides the full 2π phase coverage. The black solid curve in Figure 4.4(a) shows the simulated first-order cross-polarised transmission magnitude of the super unit cell, whose arrangement is illustrated in the inset. The transmission remains above approximately -1.2 dB across the 270–330 GHz operation band under normal incidence, confirming that the assembled super unit cell maintains high first-order diffraction efficiency after combining the individual elements. Unit-cell boundary conditions are employed, corresponding to an infinite periodic array of the super unit cell. The reported first-order cross-polarised transmission magnitude corresponds to the transmission into the first-order diffracted mode, thereby inherently accounting for the frequency-dependent beam steering angle. Although further optimisation of the super unit cell architecture is possible, the present design already achieves the required phase gradient and diffraction behaviour for efficient frequency-dependent beam steering. Additional optimisation may provide modest improvements in diffraction efficiency, transmission uniformity, and suppression of undesired diffraction orders. However, such improvements are not expected to substantially influence the overall spectrometer performance, which is primarily governed by factors such as the metasurface aperture, diffraction effects, and the imaging system. Consequently, further optimisation of the super unit cell was not pursued, as it would increase design and fabrication complexity while providing only limited benefits.

Having established the transmission performance of the super unit cell, the frequency-dependent beam deflection is investigated. To enable beam deflection, an infinite array of the super unit cell, shown in Figure 4.5(a), is considered. Each super unit cell comprises the eight individual elements arranged to form the necessary phase ramp to excite frequency-dependent beam deflection, or in other words, frequency-spreading, following the phenomenon discussed in Section 4.2. The frequency-dependent beam deflection over the 270 to 330 GHz range is presented in Figure 4.5(b). The simulated beam angle varies from 116° to 132° when referenced to the opposite normal, corresponding to an angular variation of 16° across the 270–330 GHz frequency range. When referenced to the surface normal in the beam-steering direction, these angles correspond to 64° to 48°. This behaviour closely follows the diffraction relation $\sin\theta = \lambda / D$, where $D = 1232$ µm. According to this relation, the predicted steering angles vary from 64° to 48° across 270–330 GHz, which agrees well with the simulated beam deflection.

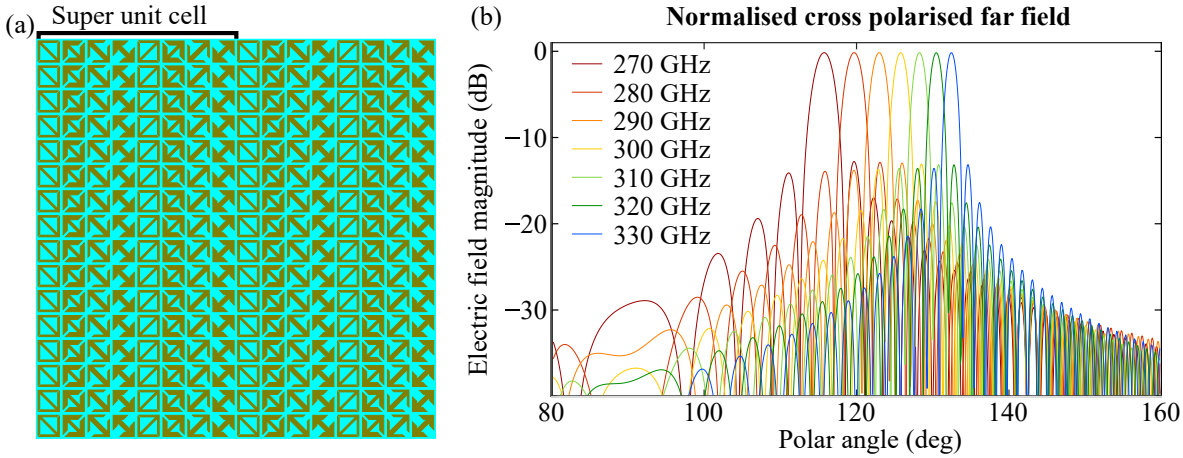

Figure 4.5. Metasurface design and response. Array-level implementation and response of phase-gradient beam deflection. (a) Metasurface design illustrating the arrangement of the middle resonant layer used to realise the phase gradient. Eight unit cells form a supercell covering the full 2π phase range. (b) Normalised cross-polarised far-field radiation patterns demonstrating frequency-dependent beam deflection across 270–330 GHz at 10 GHz intervals, with deflection angles of 116°, 120°, 123°, 126°, 128°, 131°, and 132° with respect to the opposite normal.

The use of eight-phase quantisation levels improves the approximation of a continuous phase gradient, reduces phase discretisation errors, and prevents beam broadening, thereby enhancing beam quality and ensuring that the main lobe does not overlap with neighbouring beams separated by a 10 GHz frequency interval. In addition to the dominant first-order diffracted beam, weaker secondary lobes are observed in the far-field patterns in Figure 4.5(b). These arise from residual higher diffraction orders, phase discretisation effects, and non-uniform mutual coupling between neighbouring unit cells, which is not captured in idealised periodic unit-cell simulations. Although the metasurface is designed to favour the first diffraction order, higher-order components are suppressed rather than completely eliminated. Nevertheless, these components remain significantly lower in magnitude compared to the main beam, indicating effective suppression and high diffraction efficiency. As evident from the normalised far-field patterns in Figure 4.5(b), the side-lobe peaks remain below approximately –13 dB relative to the main beam, corresponding to a main-lobe-to-side-lobe ratio of at least 13 dB across the operating frequency range.

As discussed, the objective of the frequency-spreading metasurface is to maximise the angular separation between different frequencies over the 270–330 GHz operation band under normal incidence. To achieve this, the super unit cell periodicity, D, is

selected to be only slightly larger than the wavelength corresponding to the lowest operation frequency, thereby maximising the first-order diffraction angle. However, a consequence of this design choice is an increased sensitivity to oblique incidence.

Under oblique incidence, the diffraction relation is modified to

$$\sin\theta_t = \frac{m\lambda}{D} + \sin\theta_i, \tag{4.2}$$

where $m = 1$ for the first-order diffraction, θ_t is the diffraction angle, and θ_i is the incidence angle. Since the ratio λ/D is intentionally chosen to be close to unity at the lower end of the operation band, the additional $\sin\theta_i$ term can cause the right-hand side of the equation to exceed unity even for relatively small incidence angles. Consequently, the first-order diffraction mode is no longer supported, resulting in the suppression of the desired frequency-spreading behaviour.

Therefore, the metasurface is intentionally designed and optimised for normal incidence over the 270–330 GHz operating band rather than for wide-angle operation. Although a larger angular tolerance could be achieved by increasing the super unit cell periodicity, for example by increasing the unit cell period or increasing the number of phase levels while maintaining the same unit cell dimensions, such modifications would reduce the achievable beam-steering range and consequently decrease the angular separation between adjacent frequencies. This would increase the overlap between neighbouring frequency channels and compromise the frequency discrimination capability of the proposed frequency-spreading metasurface.

4.3 Lens design

4.3.1 Zemax simulation and results

With the frequencies spread over a range of 16°, the spread beams are required to be spatially focused onto the camera sensor. The terahertz camera used here is the INO MICROXCAM-384i that has a 35 µm pitch and a sensor area of 384 × 288 pixel array, corresponding to a sensor area of 13.44 mm × 10.08 mm, and a diagonal length of 16.8 mm. A COC-based focusing lens is therefore designed to focus the spread frequencies in the diagonal direction to maximise frequency discrimination. The camera's $f/0.7$ lens functions as a fixed imaging optic that relays the spatial distribution onto the detector, with its effect accommodated through experimental alignment rather than explicit optical

modelling. COC is used here due to its low material loss with a relative permittivity of $\epsilon_r = 2.34$, loss tangent $\tan\delta = 0.0005$, and the availability of 3D printing (Busch *et al.*, 2016; Mavrona *et al.*, 2021; Maestrojuan *et al.*, 2015; Nielsen *et al.*, 2009). An aspheric biconvex lens is designed using a ray-tracing model in Ansys Zemax OpticStudio to minimise aberrations, especially at larger field angles, and to achieve a consistent spot size across the image plane. 3D printing simplifies the manufacturing of aspheric lenses that are generally difficult to manufacture using traditional methods. Despite that, to enable 3D printing of the biconvex lens as a single element, the surface curvature is minimised to satisfy the manufacturability constraints of the printing process and avoid unsupported overhangs.

The effective beam angles from the metasurface range from 64° to 48°, relative to the surface normal, representing frequencies from 270 to 330 GHz, as shown in Figure 4.5(b). To ensure reliable performance of the designed lens, especially near the band edges, an additional ±2° margin is introduced, thereby increasing the optimisation range to 66° to 46°. Apart from ensuring consistent focus quality throughout the usable spectral range, the margin also accounts for possible fabrication and alignment tolerances.

During the lens design, the object field mimicking the metasurface is intentionally tilted by −56° relative to the plane normal to the optical axis, and is slightly decentred using a coordinate break, thereby introducing an oblique incidence condition. This shifts the mean field angle to 0° within the lens reference frame and helps to reduce the physical footprint of the designed lens. The effective operational angular range shifts from 66°–46° to ±10° (with margin) relative to the optical axis of the lens. Overall, the tilting and decentring of the object plane helps to reduce the aperture and total lens diameter, making the system more compact without degrading field coverage and performance.

The optical layout shown in Figure 4.6(a) illustrates the tilting of the object plane along with the designed aspheric lens and associated ray-tracing to focus at the image plane. The biconvex aspheric lens is designed using two even aspheric surfaces to enable a sufficient degree of freedom to minimise aberrations. The lens curvature and thickness are optimised using the damped least squares optimisation algorithm. A maximum limit on lens curvature is considered based on the 3D printing constraints discussed in Section 4.3.2. The optimisation is performed based on merit function targets focused on minimising the RMS spot radius of each field and fitting most spots within the 16.8 mm focal plane while maintaining sufficient separation between spots.

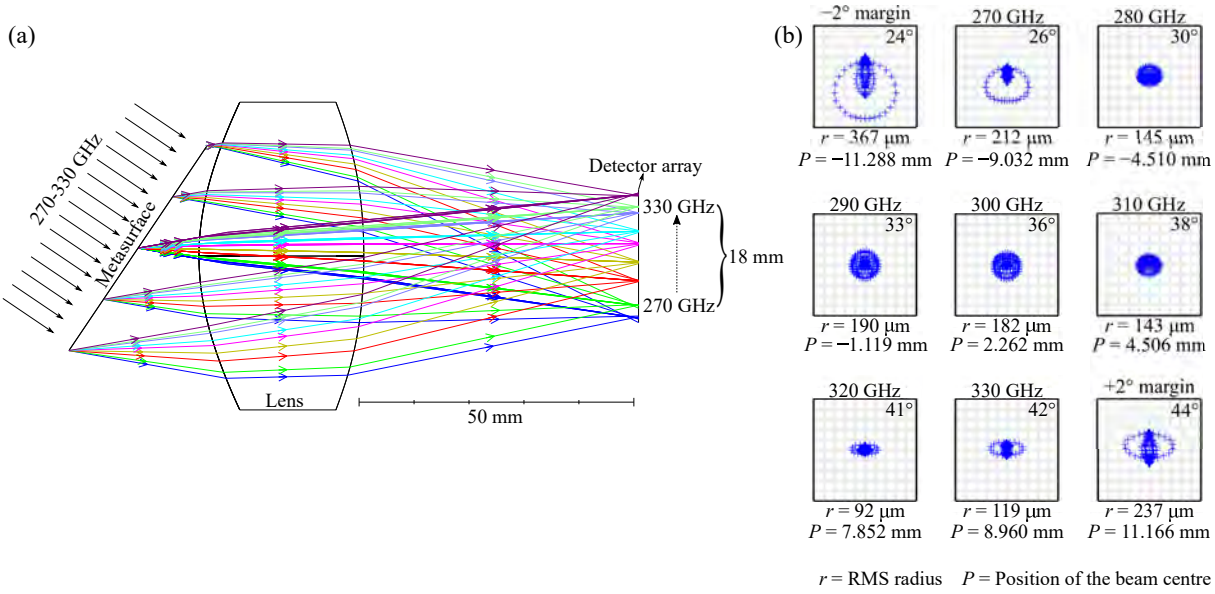

Figure 4.6. Focusing lens design and response. (a) Ray-tracing layout illustrating the input beam direction, object tilt and decentring, the optimised lens, and the corresponding beam focusing onto the image plane. (b) Corresponding ray-traced spot distributions on the image plane for incidence angles ranging from $\pm 10^\circ$ relative to the lens optical axis, including a $\pm 2^\circ$ margin to account for alignment tolerances, as indicated by the blue markers. These angles correspond to metasurface beam deflection angles of 64°–48° before tilt, representing frequencies from 270–330 GHz, as shown in Fig. 4.5(b). Including the $\pm 2^\circ$ margin, the angular range extends to 66°–46°. The RMS spot radius, r, and focal position on the image plane, P, are indicated. The RMS spot sizes are derived from geometric ray-tracing and do not include diffraction effects. The lens optimisation therefore aims to achieve tight geometric focusing while maintaining a focal position separation in mm-scale to accommodate diffraction-limited spot sizes at terahertz frequencies.

The resulting spot diagrams presented in Figure 4.6(b) show a confined focal distribution across all field angles. The RMS spot sizes are comparatively small and spread throughout the focal plane. This ensures that spatially distinguishable frequency-dependent beams are achieved at the focal plane. The spot profiles at the edge frequencies (270 GHz and 330 GHz), as well as the margin cases, exhibit ring-like intensity distributions surrounding the focal spot. This behaviour arises due to increased optical aberrations at larger incident angles, where the lens operates near the boundary of its optimised angular range. As a result, the wavefront is not perfectly corrected, leading to partial redistribution of energy and the formation of diffraction-like sidelobes. These lens-induced aberrations, such as coma and astigmatism, could be further reduced through

the use of more highly optimised aspheric optics or multi-element lens systems. However, highly aspheric lens profiles become increasingly challenging to realise accurately using single-element 3D printing, while multi-element optical systems introduce additional alignment requirements, increased system complexity, a larger footprint, and additional insertion losses. The margin cases can be disregarded, as they are introduced only to ensure robust performance across the 270–330 GHz operating range. Despite that, for the edge frequencies, the majority of the energy remains concentrated near the focal point, resulting in relatively small RMS spot radii despite the presence of these rings. This ring-like effect is not observed at the central frequencies (280–320 GHz), as they fall within the strongly optimised region for effective focusing. Although the available focal plane of 16.8 mm is smaller than the total focal spread of approximately 18 mm produced by the seven beams corresponding to 270–330 GHz at 10 GHz intervals, as shown in Figure 4.6(b), the system can still capture six consecutive beams simultaneously. Specifically, the beams corresponding to 280–330 GHz occupy positions from -4.51 mm to 8.96 mm on the focal plane, as illustrated in Figure 4.6(b), resulting in a total spatial spread of 13.47 mm, which fits within the available detector area. Achieving such a focusing lens design involves several challenges, including the initial non-zero mean beam angle, the singlet lens design, 3D printing compatibility, and the highly confined focal plane while ensuring sufficient inter-beam separation and reducing aberrations. Altogether, the system, including the metasurface and the lens, allows spatial separation of the beams from 270 to 330 GHz and enables simultaneous observation of most beams at the terahertz camera.

4.3.2 Fabrication and measurement

The optimised lens geometry obtained from Zemax is exported as a solid-CAD model for 3D printing. The lens is fabricated using COC with a refractive index $n_{\mathrm{COC}} = 1.521$ (Chung *et al.*, 2024). To facilitate stable fabrication, a COC holder is integrated with the lens as a single monolithic structure, as indicated in Figure 4.7(a). This provides a flat base surface for the printer bed and allows improved dimensional stability during the printing process.

The lens is printed vertically from the holder base and progresses upward to form the curved optical surface. Vertical printing is chosen as the singlet lens is biconvex. Therefore, a flat surface to begin printing is required for support. The surface curvatures of the lens surface are deliberately kept moderate to ensure printability and

prevent structural collapse during layer deposition. The fabrication is performed using a Prusa MK3S+ printer at 100% infill to maximise structural uniformity and dielectric consistency. However, even with the 100% infill, the deposition process may introduce sub-wavelength air voids within the printed volume, which at sub-millimetre wavelengths may primarily contribute to slight effective refractive index reduction, thus slightly affecting the overall performance of the lens. The printed lens is finally visually inspected and prepared for integration into the spectrometer assembly.

The performance of the 3D-printed COC lens is experimentally characterised using the setup shown in Figure 4.7(b) and (c). In this experiment, only the focusing lens is tested without the metasurface in order to independently evaluate its spatial focusing capability. Two input beam conditions are investigated. In the first case, a collimated input beam is used, where the output of the horn antenna is first collimated using a collimating lens, as shown in Figure 4.7(b). In the second case, a divergent input beam is used by omitting the collimating lens, as illustrated in Figure 4.7(c). These two cases represent the possible beam conditions that may arise when the metasurface is integrated with the lens.

A VDI WR-3.4 signal generator extension (SGX) module provides a continuous-wave terahertz signal to the transmitter horn antenna. To mimic the angular deflection that would be produced by the metasurface, the SGX and the collimating lens assembly are mechanically rotated using a rotating stage for the collimated case, while only the SGX is rotated for the divergent case. The rotation is relative to the reference plane of the lens, such that the incidence angle is varied from $\pm 8^\circ$ (without margin), representing the effective angular range seen by the lens after the metasurface alignment. For each case and angular position, the transmitted beam is focused by the 3D-printed biconvex lens and projected onto the terahertz camera. The resulting focal spots are recorded with the camera's $f/0.7$ lens to evaluate the intrinsic focusing behaviour and system-level imaging performance. Representative spot diagrams are presented in Figure 4.7(b) and (c), demonstrating consistent angular-to-spatial focusing across the tested range. The deflection angles for the representative spot diagrams -4°, -1°, 2°, 4°, and 7° correspond to frequencies 280 GHz, 290 GHz, 300 GHz, 310 GHz, and 320 GHz, respectively, after the tilting.

The focusing performance of the lens is evaluated by comparing the simulated and experimentally observed focal spot sizes. Although the ray-tracing spot diagrams in Figure 4.6(b) predict RMS spot radii ranging from 92 µm to 202 µm across the operational

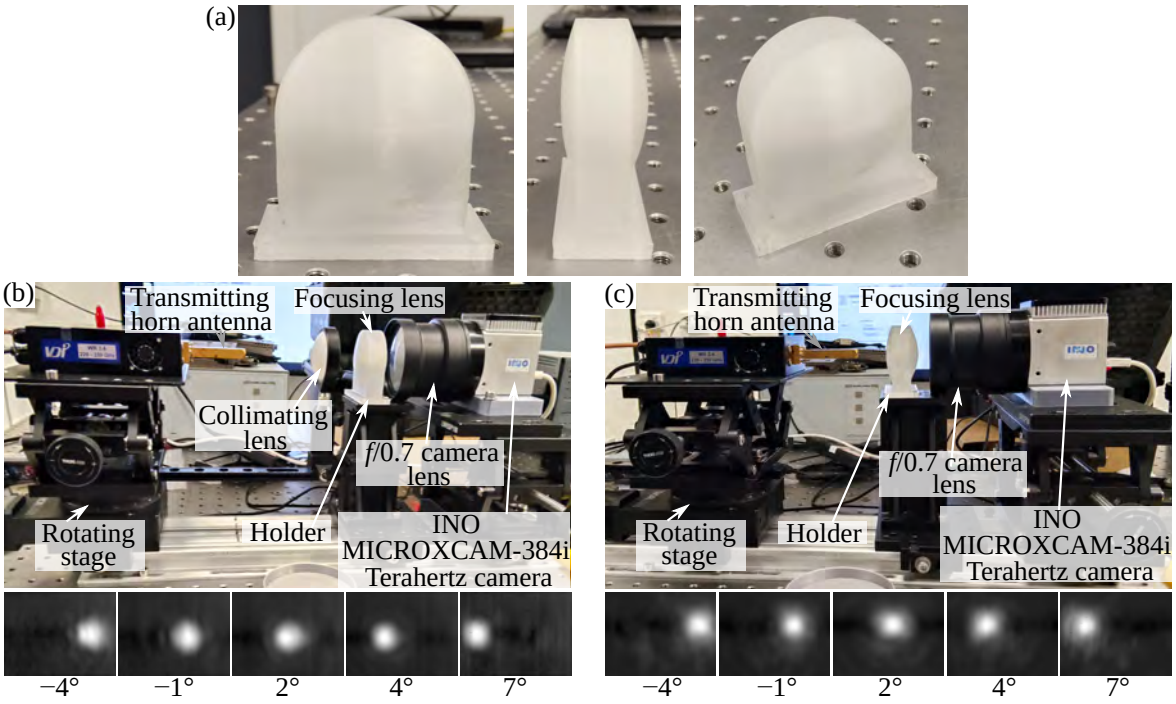

Figure 4.7. Lens design and characterisation. Design and experimental characterisation of the focusing lens. (a) 3D-printed aspheric bi-convex lens with integrated holder, including front, side, and perspective views. (b) Measurement setup and representative spatial focusing for the collimated input case using a collimating lens. (c) Measurement setup and representative spatial focusing for the divergent input case without a collimating lens. The measurement system consists of a WR-3.4 source, the fabricated lens, and an INO MICROXCAM-384i terahertz camera with an $f/0.7$ lens. The WR-3.4 source is fixed at 300 GHz and rotated to generate incident angles from -4° to 7°, emulating the angular beams expected from frequencies 280 GHz, 290 GHz, 300 GHz, 310 GHz, and 320 GHz, respectively. The resulting focal spots recorded by the INO MICROXCAM-384i terahertz camera are shown below each setup.

angular range, these values only represent the geometric imaging performance of the lens and therefore do not account for diffraction effects. In practice, diffraction plays a dominant role in the terahertz regime, where the achievable focal spot size is fundamentally constrained by the wavelength. For a wavelength of approximately 1 mm at 300 GHz, the diffraction-limited spot size is expected to be on the order of 1–2 mm. The experimentally observed focal spots shown in Figure 4.7 are consistent with this estimate, appearing slightly larger but remaining compact and approximately circular. The slight enlargement of the measured spots can be attributed to several practical factors, including the divergence of the horn antenna, the alignment tolerances in the experimental setup, and the fabrication imperfections in the 3D-printed COC

lens. Despite these factors, the focal spots remain significantly smaller than the spacing between neighbouring beam positions, allowing the frequency-dependent beams to be clearly distinguished on the detector. Consequently, the system is able to resolve frequency intervals as small as 10 GHz.

For demonstration, the horizontal axis is used to illustrate the spectral dispersion axis. However, in the practical implementation of the system, the phase-gradient metasurface and the designed aspheric lens will be integrated together within a circular housing, similar in form factor to the existing $f/0.7$ camera lens. This combined module will be mounted in front of the $f/0.7$ camera lens and rotated by 45 degrees to utilise the diagonal dimension of the image plane, thereby maximising the available spatial mapping area.

4.4 Conclusion

This chapter has presented a compact system to turn an incoherent terahertz camera into a spectrometer for frequencies ranging from 270 to 330 GHz. The system is based on angular dispersion and spatial mapping. Angular dispersion is achieved using a phase-gradient metasurface to introduce frequency-dependent beam deflection, i.e., to encode spectral information as angular variations. The phase-gradient metasurface consists of three metallic layers, where the middle layer consists of eight distinct unit cell designs arranged in an array to facilitate a phase gradient in one dimension. The two outer metallic layers are orthogonal wire grids used to enhance efficiency by polarisation control. The metasurface deflects beams from 270 to 330 GHz within an angular range of 64° to 48° from the normal of the metasurface. The frequency-dependent beam deflection is converted into measurable spatial separation using a compact refractive focusing lens. The lens is optimised to achieve stable focusing onto the 16.8 mm sensor area of the camera, with controlled aberrations across the defined angular range. The lens is fabricated using 3D printing, and the performance of the lens is experimentally validated, with angular scanning performed to emulate metasurface-induced deflection. The measured focal spot demonstrate consistent angular-to-spatial mapping within the available focal plane, validating the optical design methodology. Overall, the system is capable of transforming frequencies spanning 270–330 GHz into distinct spatial focal positions. Although the design consideration presented in this work is calculated for 270–330 GHz, the same design strategy applies to other frequencies

and is therefore scalable. The demonstrated architecture supports single-shot spectral acquisition without mechanical scanning and establishes the feasibility of a lightweight and manufacturable sub-terahertz spectrometer suitable for portable applications that can be easily integrated into a terahertz camera.

Chapter 5

Terahertz Frequency Analyser

(Original Content)

IN wireless communications, accurate frequency estimation is essential to support reliable demodulation, channel management, and spectrum surveillance. At terahertz frequencies, the higher carrier values and narrow channel spacing demand much finer frequency estimation, which requires high-resolution frequency discrimination. Conventional grating-based approaches are bulky and limited in resolution, making them unsuitable for compact terahertz systems. We present a 3D-printed pseudo-random dielectric metasurface that enables sub-gigahertz frequency discrimination in the 220–330 GHz band through spatially diverse near-field patterns. The design leverages frequency-dependent scattering to create unique intensity distributions captured by a terahertz camera. We demonstrate that these spatial signatures can be used for frequency discrimination by training a convolutional neural network (CNN) to identify the frequency from a single image. To substantiate the reliability of the metasurface response, we employ multiple beam configurations with varying incidence angles in our experimental setup. The results demonstrate high classification accuracy over the operational range, thus corroborating the metasurface as a viable passive frequency analyser for terahertz communications.

5.1 Introduction

Terahertz waves offer short-range high-speed wireless communications services that play the role of a critical driver of the 6G wireless communications system (Nagatsuma *et al.*, 2016; Shehata *et al.*, 2023; Akyildiz *et al.*, 2022). In particular, the 252 GHz to 450 GHz region, defined as the terahertz communications band by the most recent IEEE 802.15.3-2023 standard (IEEE 802 LAN/MAN Standards Committee, 2024) is capable of pushing data rates to around a few terabits per second (Song and Lee, 2021; Li *et al.*, 2023b). The enormous gigahertz-level bandwidth of terahertz waves supports tightly spaced communications channels (Xue *et al.*, 2024). However, to fully exploit the ultra-high data rates in such tight channels, high-resolution, precise frequency predictions are required to counter the severe effects of frequency offset, such as demodulation, desynchronisation, and inter-channel interference. Thus, carrier frequency estimation in terahertz communications is essential (Dovelos *et al.*, 2021).

A feasible passive approach to accurate and high-resolution frequency estimation is to design a structure with engineered fine-grained frequency diversity, such that small frequency shifts produce distinct and repeatable responses, thereby enabling high-resolution frequency discrimination. Conventional approaches for frequency discrimination, like focused or split-beam spectrometers featuring gratings, produce smooth and continuous phase variations. Thus, the diffraction patterns in small frequency shifts have high correlation, resulting in limited frequency resolution. Although gratings support predictable frequency responses, they require bulky optical components and precise alignment. Moreover, the diffraction-based operation is strongly dependent on the angle of incidence, thereby limiting robustness. The use of random phase distribution is motivated by the goal of maximising frequency diversity and minimising correlation between adjacent frequency patterns, thereby achieving higher resolution frequency discrimination than conventional methods. Frequency-diverse systems, including antennas and metasurfaces, provide a prospective avenue by facilitating predictable yet diverse frequency-to-pattern mappings, enabling expedited, compact, passive frequency estimation, and finer frequency discrimination (Imani *et al.*, 2020). This allows sub-gigahertz frequency discrimination with enhanced resolution. This technique eliminates the need for conventional dispersive components or mechanical scanning, reduces hardware complexity, and boosts flexibility in dynamic situations. Despite the potential of terahertz frequency-diverse devices, research on this topic is still in its infancy (Imani *et al.*, 2020; Li *et al.*, 2024b; Seidi *et al.*, 2025).

In this work, we present a 3D-printed frequency-diverse dielectric metasurface designed for passive terahertz frequency discrimination and estimation in the 220–330 GHz range. The 3D-printed pseudo-random metasurface offers several critical advantages for compact and practical terahertz applications. The design operates entirely in the near field, enabling a flat configuration where a terahertz camera can directly capture complex and frequency-dependent spatial patterns. These patterns exhibit high inter-frequency decorrelation, supporting fine frequency discrimination at sub-gigahertz resolution. The design is inherently robust to variations in angle of incidence and beam profile, making it suitable for dynamic or realistic, non-ideal environments, where multipath propagation is minimal in the terahertz regime (Do *et al.*, 2021). Furthermore, the metasurface is fabricated using high-resolution 3D printing of low-loss cyclic olefin copolymer (COC), which simplifies prototyping and supports scalable, cost-effective production. These advantages collectively position the pseudo-random metasurface as a promising candidate device for passive frequency analysis, channel condition classification, non-coherent carrier estimation, and spectrum awareness without active demodulation in terahertz communications systems.

5.2 Methodology

The metasurface is designed to produce optimal independent pseudo-random radiation patterns across frequencies from 220 to 330 GHz while reducing inter-frequency correlation through spatially diverse scattering. The structure consists of 3200 square pillars arranged in four concentric rings, each containing 800 square pillars of distinct lateral dimensions, 487 μm, 524 μm, 568 μm, and 619 μm, corresponding to half-wavelengths at 308 GHz, 286 GHz, 264 GHz, and 242 GHz, respectively, as shown in Figure 5.1(a) and (b). These dimensions are strategically selected to enhance frequency sensitivity by embedding structural features corresponding to different points across the spectrum. The concentric formation leverages near-field beam behaviour, where higher-frequency waves or shorter wavelengths tightly concentrate toward the centre. As such, pillars with smaller widths are placed in the inner rings, while pillars with larger widths are positioned in the outer rings. This stratification yields enhanced frequency-dependent scattering and spatial encoding that would not appear in the far field. Square pillars are chosen to comply with the Cartesian coordinate constraints of the 3D printer, which simplifies fabrication. A multiscale, layered configuration is used by randomising pillar heights from 250 μm to 10,000 μm in steps of 250 μm, as shown in Figure 5.1(c), to

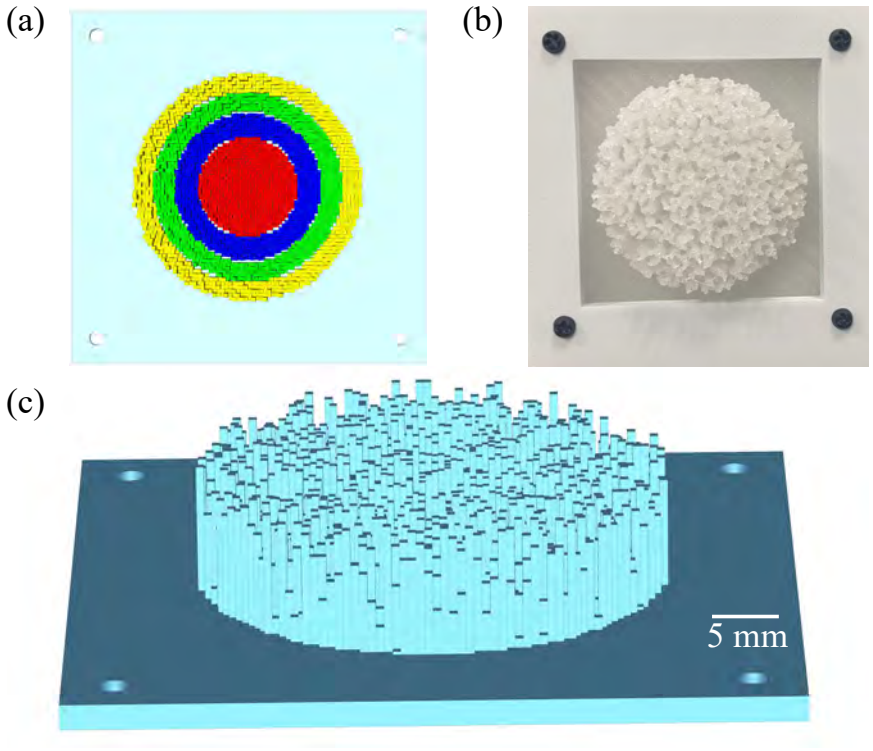

Figure 5.1. Design of the pseudo-random metasurface. 3D-printed pseudo-random metasurface, designed on a square platform with four screw holes for mounting onto the holder. (a) Top view CAD rendering highlighting four concentric zones with square pillars of widths 487 µm (red), 524 µm (blue), 568 µm (green), and 619 µm (yellow). Each zone contains 800 pillars with zone radius of 8.1 mm (red), 11.9 mm (blue), 15.2 mm (green), and 18.5 mm (yellow). (b) Fabricated metasurface printed in COC and secured on a square mounting platform. (c) 3D CAD perspective view showing randomised pillar height variation to achieve near-field spatial diversity. Note that the color codes in (a) are used solely to indicate different pillar widths and do not represent material differences.

introduce asymmetrical and complex scattering, producing unique near-field patterns for each frequency (Li *et al.*, 2024b). Due to the large physical dimensions, multiscale geometry, and 3200 pillars with varying heights, full-wave simulation of the complete metasurface across 220–330 GHz would require substantial computational resources and simulation time. Furthermore, the objective of the design is to generate frequency-dependent pseudo-random scattering patterns rather than a deterministic electromagnetic response. Therefore, the device is not simulated and is instead characterised experimentally.

The metasurface is fabricated, as shown in Figure 5.1(b), using high-resolution 3D printing of COC, a material chosen for its low-loss properties in the terahertz regime (Yi *et al.*,

2015). The structure is printed using a 0.25 mm nozzle at a nozzle temperature of 250°C and a heated bed temperature of 75°C. A layer height of 250 µm is employed, and the metasurface was fabricated vertically from the substrate upwards. Although the smallest pillar width of 487 µm is approximately twice the nozzle diameter, all pillar dimensions are sufficiently larger than the extrusion width to be reliably realised using multiple adjacent deposition tracks. Terahertz waves from 220 to 330 GHz are directed onto the metasurface, and the resulting transmitted patterns are captured using a MICROXCAM-384i terahertz camera from the Institut national d'optique (INO), equipped with an $f/0.7$ lens (Institut national d'optique , INO), as shown in Figure 5.2(a). These patterns are then used to train a machine-learning model and validate proper frequency estimation.

5.3 Experiment and results

5.3.1 Continuous-wave measurement

Figure 5.2(a) shows the experimental setup where a VDI WR-3.4 signal generator extension (SGX) module provides a continuous-wave terahertz signal through the transmitter horn antenna. A terahertz camera records the wave patterns transmitted by the metasurface. Representative examples of these frequency-dependent wave patterns are shown in Figures 5.2(b), (c), and (d). Three beam configurations are used, namely, collimated, converging, and diverging, with various angles of incidence and source-to-metasurface distances. Hereby, a single-lens setup is employed for collimation, a two-lens setup for convergence, and no lens for diverging beams. The terahertz source is swept from 220 GHz to 330 GHz with a resolution of 0.5 GHz, resulting in 221 images. For each frequency, five repetitions of wave pattern images are captured at four source-to-metasurface distances, five incidence angles within $\pm 10°$, and three beam configurations, totalling 66,300 images. The different source-to-metasurface distances and incidence angles are not fixed for each frequency but are varied within predefined ranges. This is done to introduce additional diversity into the measured wave patterns, resulting in a richer dataset with increased variation in the spatial scattering responses. All images are then processed by subtracting the raw images from the reference image of the camera to remove the background radiation and to enhance feature detection. These subtracted images are then normalised by linearly scaling their pixel intensities between 0 and 1 to allow consistent comparison across measurements. The normalised

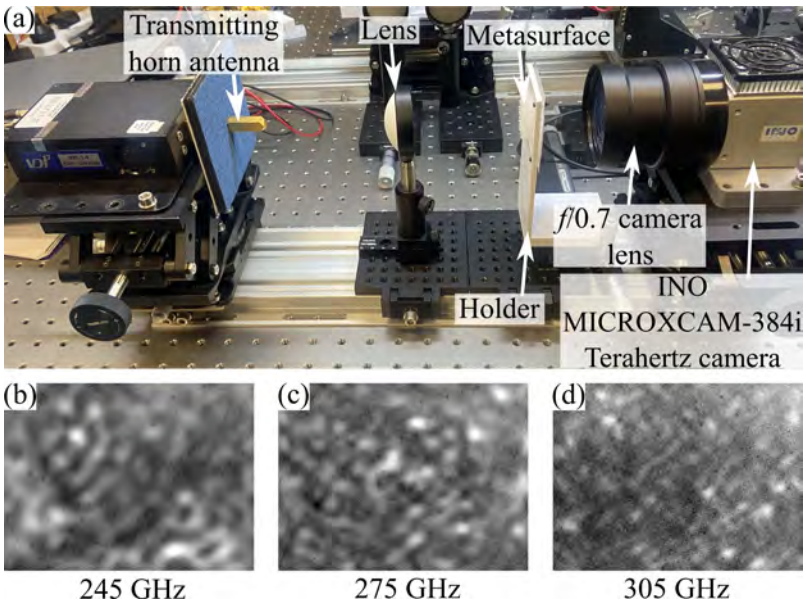

Figure 5.2. Experimental setup and representative wave patterns. Measurement setup and frequency-dependent near-field patterns. (a) Measurement setup with WR-3.4 source operating over 220–330 GHz, lens for collimation, pseudo-random metasurface on holder, and terahertz camera. (b), (c), and (d) Wave patterns at different frequencies 245 GHz, 275 GHz, and 305 GHz, respectively. These wave patterns correspond to a specific case: collimated wave input at a fixed distance and angle.

images, including all beam configurations, angles, and distances, are used to train a machine-learning model.

Although the experiments are limited to a laboratory setup, within this controlled setup, the metasurface is tested under a diverse range of beam and incidence configurations to emulate practical variability. Different beam configurations, along with different angles of incidence as well as varying distances between the source, metasurface, and camera, are used to vary the terahertz intensity and noise conditions. All these variations correspond to significant changes in wavefront curvature, illumination area, noise condition, and field distribution on the metasurface, thus partially representing dynamic and non-ideal environments. Furthermore, in terahertz communications systems, multipath propagation is very weak due to a highly directional beam profile and strong free-space path loss. Therefore, in this frequency range, the line-of-sight (LoS) is the predominant propagation mechanism (Do *et al.*, 2021).

5.3.2 Training and validation using continuous-wave data

The model selection is crucial to the overall performance of the analyser. With the collection of distinct frequency-diverse images, we formulate the frequency prediction problem as an image classification task, where the frequencies serve as labels for the captured images. The state-of-the-art YOLOv11 (You Only Look Once) (Khanam and Hussain, 2024) model is adopted for the classification task due to its enhanced feature extraction backbone architecture, which primarily serves the task of transforming the raw image input data into high-level features used for the classification task, while being computationally lightweight. In addition, YOLO architecture is highly effective as a pre-trained, open-source convolutional framework that can be readily adapted for image-based classification tasks. The Nano model variant is used to lower the computational cost and avoid overfitting. This variant comprises 84 layers, including convolutional, residual (He *et al.*, 2016), and partial attention layers (Wang *et al.*, 2020). Each layer type plays a critical role in feature extraction, pattern recognition, and enhancing model robustness against variations in image quality. With YOLOv11 as the backbone image encoder, we further fine-tune this pre-trained model on our collected experimental data.

In order to efficiently train and validate the model, an 80–20 data split is adopted, where 80% of the data is used for training and the remaining 20% for validation. The model is trained for 50 epochs with a batch size of 16 and an input image size of 224×224 pixels. Here, an epoch represents one complete pass through the entire training dataset, while the batch size denotes the number of images processed before the model parameters are updated. The selected batch size provides a balance between computational efficiency and stable optimisation, whereas 50 epochs allow the model to sufficiently learn the underlying features without introducing excessive overfitting. We employ an initial learning rate of 0.01, which controls the magnitude of the parameter updates during optimisation, and a weight decay of 0.0005 to regularise the model and reduce overfitting. Data augmentation, including random horizontal flips, scaling, translation, and random erasing, is employed to further diversify the training dataset and improve the model's ability to predict unseen data points.

To analyse the classification performance of the model, a confusion matrix across the spectrum, presented in Figure 5.3(a), illustrates the distribution of predicted versus true frequencies, where the shade of blue indicates accuracy, and each block corresponds to a 0.5 GHz interval. The diagonal elements indicate correct predictions, and off-diagonal

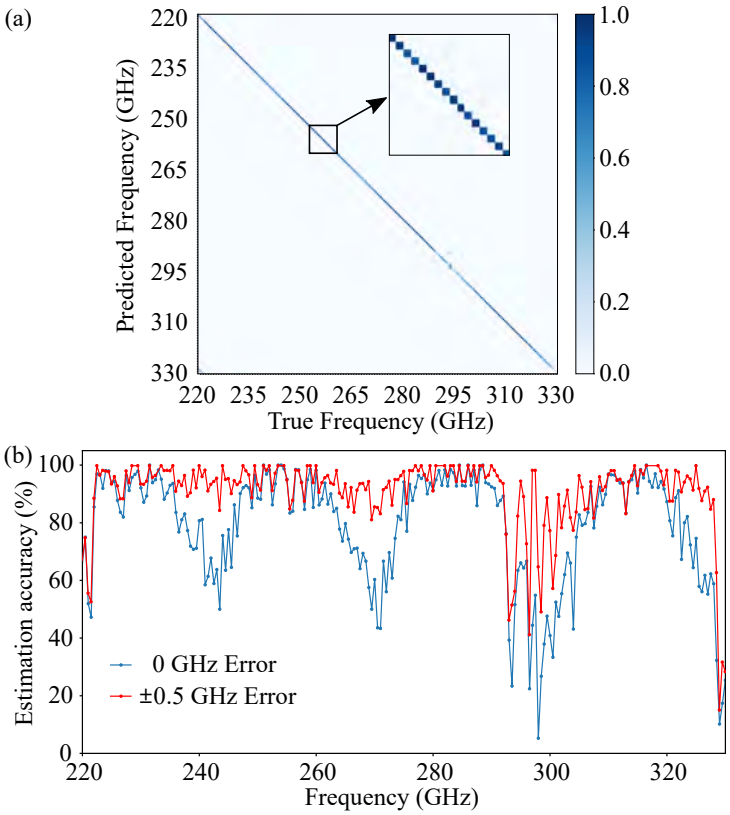

Figure 5.3. Metasurface and CNN performance. Frequency estimation performance of the pseudo-random metasurface across the 220-330 GHz band. (a) Confusion matrix of predicted versus true frequencies. (b) Estimation accuracy at 0.5 GHz frequency resolution, with 0 GHz error (blue) indicating exact predictions and ± 0.5 GHz error (red) showing predictions within 1 GHz tolerance.

elements correspond to misclassifications. A strong diagonal line of darker blue shades on the confusion matrix confirms high performance over a large portion of the spectrum, indicating the strong frequency estimation capability of the metasurface. However, a closer inspection of the diagonal reveals slight thickening of the diagonal line at around 238–246 GHz and 262–275 GHz, pointing to slight misclassification around these frequency ranges. Additionally, strong misclassification is observed around 290–300 GHz, as the diagonal pattern in that range is evidently broken.

To further study the misclassification pattern specifically around the above-mentioned frequencies, a per-frequency accuracy across the 220–330 GHz band is shown in Figure 5.3(b). The 0-GHz error estimation accuracy (shown in blue) corresponds to the model's prediction across the frequency range with zero absolute error within a resolution of 0.5 GHz, where the estimation accuracy exceeds 80% with peaks close to 100% in several sub-bands. Several dips in accuracy are observed around 242 GHz,

265 GHz, and 290 GHz, consistent with the slight off-diagonal behaviour observed in the confusion matrix. These dips align with the pillar dimensions chosen to correspond to half-wavelengths at these frequencies. The errors can be attributed to the reduced spatial diversity due to structural resonances at these frequencies, leading to partially correlated near-field patterns and curtailed classification accuracy. However, the thickening of the diagonal line around 242 GHz and 265 GHz in the confusion matrix is slight, indicating that a high accuracy can be achieved with slightly enhanced tolerance.

The ± 0.5 GHz error estimation accuracy shown in red in Figure 5.3(b) demonstrates an estimation accuracy within 1 GHz tolerance, which demonstrates high estimation accuracy constantly exceeding 80% throughout the spectrum except for a large dip from 290–300 GHz. This large dip is primarily caused by the reduced sensitivity of the terahertz camera and its lens in this particular spectral region, as confirmed by a separate calibration test. The calibration test is performed without the metasurface, using only the WR-3.4 horn to project the terahertz wave onto the terahertz camera equipped with the $f/0.7$ lens, to isolate and assess the native response of the detection system, i.e., the camera and lens. The calibration tests discussed in Appendix B reveal nearly identical spatial patterns between 290 GHz and 300 GHz, closely resembling the reference image of the camera, corroborating that the observed accuracy drop originates from the detector's reduced responsivity rather than from the metasurface or the CNN model. Examining the accuracy within an absolute error tolerance of ± 0.5 GHz reveals that the previously observed dips in accuracy across the 238–246 GHz and 262–275 GHz sub-bands are recovered.

Figure 5.4 visualises representative qualitative estimation performance, showcasing a set of measured patterns at selected known frequencies as the labels and their corresponding predicted frequency labels produced by the CNN model. The close correspondence between the measured and predicted frequencies illustrates the model's ability to learn frequency-dependent spatial features, demonstrating the effectiveness of the spatial encoding strategy. Moreover, as shown in Figure 5.4, out of the 16 representative test frequencies, only one prediction is incorrect, indicating strong frequency discrimination. Note that this incorrectly predicted frequency lies in the 290–300 GHz region, where the terahertz camera experiences reduced sensitivity. This indicates that the misclassification occurs mainly from the detector, and not from the metasurface design or the CNN model. A more stable camera response in this region would lead to higher accuracy.

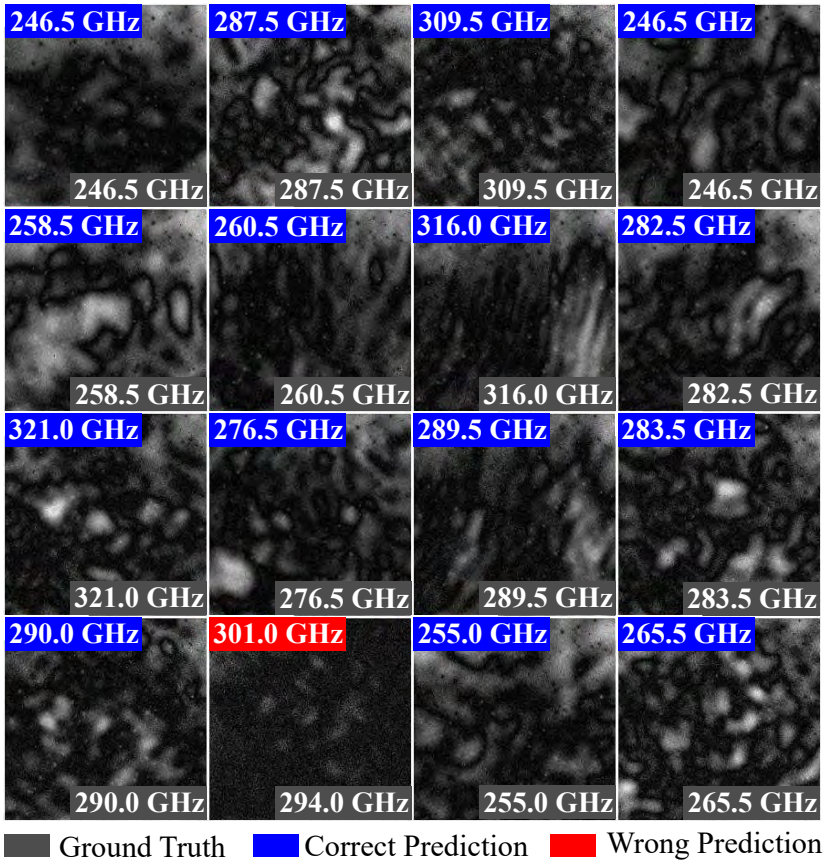

Figure 5.4. Representative pattern images under continuous wave. The true frequencies are shown below each image, while the predictions by the CNN model are displayed above. Correct prediction is highlighted in blue, and wrong prediction is highlighted in red.

5.3.3 Finite-bandwidth measurement

In communications, signals possess a finite bandwidth, in which the observed spatial pattern represents the superposition of all frequency components within that band. As the bandwidth increases, the resulting pattern becomes more complex, making accurate estimation progressively more challenging. Nonetheless, typically, the carrier amplitude is much stronger than the modulation sidebands, making frequency prediction with the proposed approach feasible.

To investigate our design and model's applicability under a finite-bandwidth signal, we design an experiment where the input has a controlled finite bandwidth, and the corresponding patterns are recorded by the camera. The measurement setup is almost identical to the previous setups discussed, except that an arbitrary waveform generator (AWG) is used alongside the signal generator to produce the desired bandwidth. The outputs of the signal generator and AWG are fed to an RF mixer, after which the RF

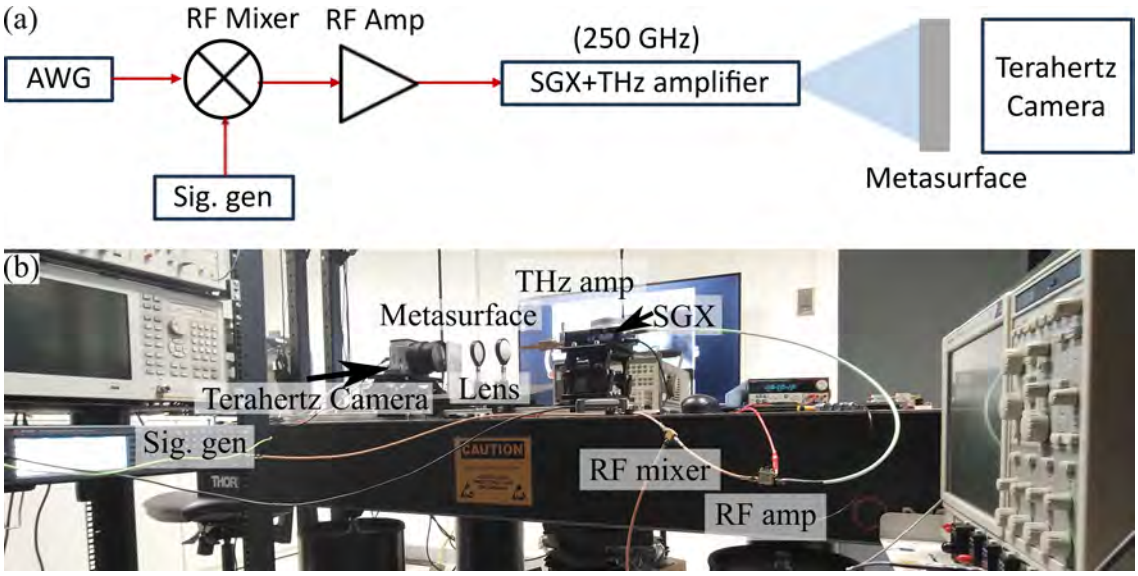

Figure 5.5. Finite-bandwidth measurement concept. (a) Block diagram of the finite-bandwidth terahertz measurement setup. (b) Measurement setup following the block diagram in (a). A two lens setup for convergent beam is shown as an example.

signal is amplified using an RF amplifier and supplied to the frequency multiplier. A terahertz amplifier is used to amplify the terahertz wave to compensate for power loss. The measurement setup is shown in Figure 5.5(a) and (b). Due to the frequency limitation of the RF amplifier and the terahertz amplifier (W.R-4.3), the tested frequencies are limited to below 250 GHz. We use all three beam configurations and apply variations in intensity and incidence angle to record the corresponding patterns under different bandwidths. The images for those cases are used as validation data for the model that was originally trained using unmodulated signals.

5.3.4 Validation using finite-bandwidth data

The accuracy as a function of error tolerance provides further insight into the robustness of the proposed system under finite-bandwidth excitation. The accuracy for the 2 GHz and 4 GHz bandwidth cases is shown in Figure 5.6. Here, the error tolerance defines the allowable deviation between the predicted and true frequencies for a prediction to be considered correct. For a bandwidth of 2 GHz, which is close to the smallest channel bandwidth of 2.16 GHz defined by the IEEE 802.15.3d standard for terahertz communications (IEEE 802 LAN/MAN Standards Committee, 2017), an accuracy of around 73% is achieved within an error margin of ± 1 GHz, indicating that channels

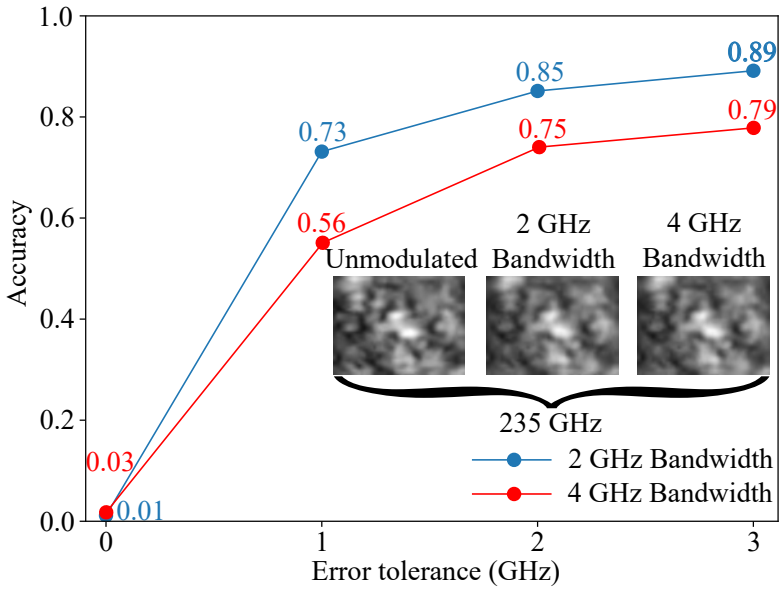

Figure 5.6. Accuracy under finite-bandwidth wave. Frequency estimation accuracy with respect to error tolerance for modulated signals with 2 GHz bandwidth (blue), and 4 GHz bandwidth (red). Insets show representative near-field patterns at 235 GHz for unmodulated, 2 GHz, and 4 GHz bandwidth signals.

1–32 defined in the IEEE standard can be predicted with 73% accuracy. Based on the channel bandwidth, an error tolerance of ± 1 GHz for the 2 GHz case and ± 2 GHz for the 4 GHz case ensures that the predicted frequency remains within the correct channel. At these tolerances, the channel-level prediction accuracy is approximately 73% and 75% for the 2 GHz and 4 GHz bandwidth cases, respectively, as observed in Figure 5.6.

The figure shows that the narrower signal bandwidth consistently achieves higher accuracy. This behaviour arises because broader input spectra contain a larger range of frequency components, producing increased overlap between the corresponding spatial patterns, as illustrated in the inset of Figure 5.6. The resulting reduction in pattern distinctiveness makes frequency estimation more challenging and consequently reduces prediction accuracy. Furthermore, the accuracy exhibits a rapid increase at low error tolerances, followed by a gradual saturation, indicating that most prediction errors are confined within a limited frequency deviation range. These results highlight an inherent trade-off between frequency resolution and accuracy, while a smaller error tolerance enables finer spectral resolution, it results in lower accuracy due to pattern ambiguity, whereas a larger tolerance improves accuracy at the expense of reduced resolution.

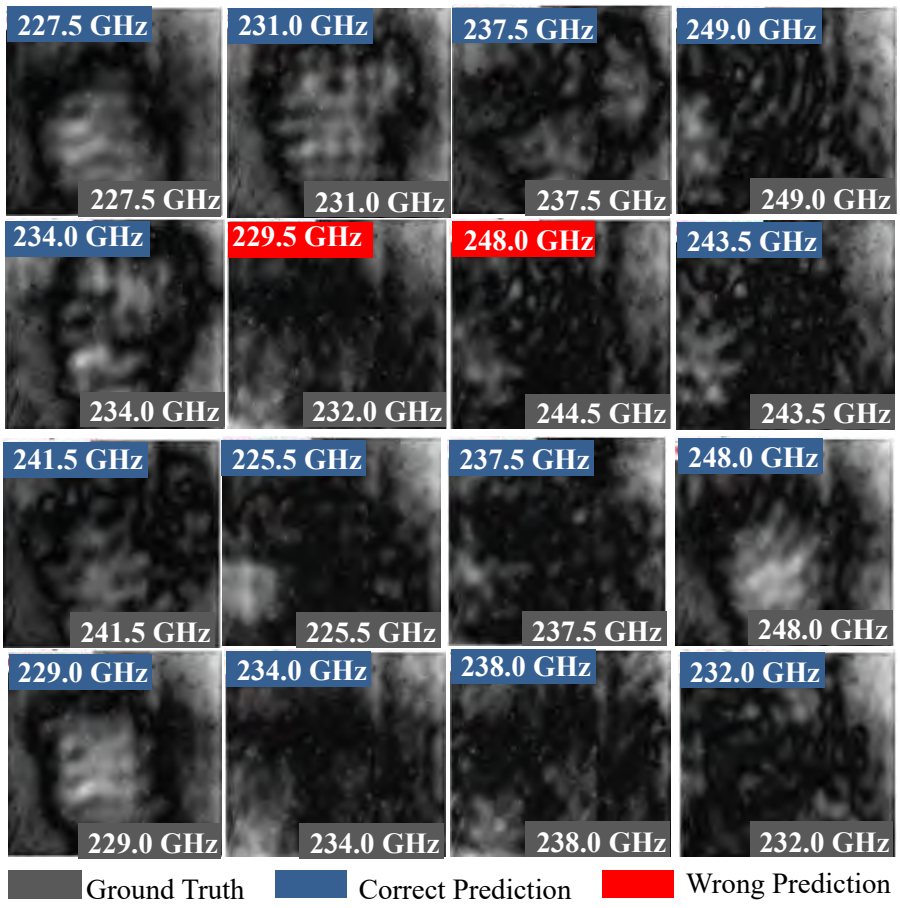

Figure 5.7. Representative pattern images under 2 GHz bandwidth signals. The true frequencies are shown below each image, while the predictions by the CNN model are displayed above. Correct prediction is highlighted in blue, and wrong prediction is highlighted in red.

Representative samples of true and predicted frequencies at a 2 GHz bandwidth are shown in Figure 5.7. The figure visualises qualitative estimation performance by presenting a set of measured near-field patterns at known frequencies alongside their corresponding predicted frequency labels produced by the model. Out of the 16 representative samples shown, only 2 predictions are incorrect, indicating strong frequency discrimination under finite-bandwidth excitation. The misclassified cases primarily occur when the measured patterns exhibit reduced contrast or share similarities with neighbouring frequency responses. This behaviour arises from finite-bandwidth effects, where the superposition of frequency components leads to partial overlap of spatial features, increasing ambiguity in the prediction. Notably, the incorrect predictions remain close to the true frequency, suggesting that the errors are largely confined to neighbouring channels rather than random misclassification. Although the exact prediction accuracy for the 2 GHz bandwidth case in Figure 5.6 is low, Figure 5.7 shows

that 14 out of 16 predictions are accurately predicted. This discrepancy arises because Figure 5.6 reflects performance over the full dataset with varying conditions, whereas Figure 5.7 presents selected representative examples.

5.4 Conclusion

This chapter has demonstrated a compact, frequency-diverse metasurface that transforms a terahertz camera into a passive frequency analyser over the 220–330 GHz range. By generating distinct near-field spatial patterns, the metasurface enables near-accurate frequency recognition using a YOLO-based image classification model. Its concentric design improves the angular robustness, and its low-loss, 3D-printable pseudo-random design makes it suitable for accurate frequency prediction under diverse illumination conditions. The estimation accuracy can be further improved by the use of larger YOLOv11 models that offer enhanced depth and feature extraction capability, however, at the cost of increased computational resources. Overall, the metasurface acts as a compact, passive frequency analyser ideal for terahertz applications, with potential uses in terahertz communications to facilitate carrier estimation, channel monitoring, and passive spectrum surveillance for security applications. The system is designed to provide frequency awareness in terahertz systems by identifying carrier or channel frequencies in real time without electrical mixing or local oscillators, to complement coherent front-end receivers, particularly where conventional electronic frequency analysers are difficult to deploy. Future work will focus on improving the prediction accuracy across wider operational bandwidths, and exploring the use of the pseudo-random frequency-dependent scattering patterns for various other applications such as optical token, cryptography, physical unclonable functions.

Chapter 6

Thesis Summary

THIS Chapter concludes this doctoral thesis by summarising the research topic and the original contributions. Chapter 1 provides an introduction to the research topic and outlines the background knowledge, relevant literature, and motivation pertaining to this thesis. The original contributions in relation to terahertz wave engineering incorporating metasurfaces are detailed in Chapters 2 to 5. Finally, this Chapter is concluded by providing an outlook for future research on metasurface-based terahertz wave manipulation, detection, and analysis.

6.1 Thesis conclusion

This doctoral thesis is centred on the development of metasurfaces for terahertz wave technologies. The aim of this thesis is to realise compact and passive devices for terahertz wave manipulation, detection, and analysis, while being significantly low-profile and cost-effective. The proposed devices are designed such that they can be readily integrated into existing terahertz systems to replace or complement current devices and enhance overall performance. This Section provides a brief summary of the original contributions of the thesis.

Wave manipulation This part contains Chapter 2, and it presents a study on a transmissive reconfigurable polarisation converter. A novel dual resonant plate design is proposed, and a reconfigurable polarisation converter based on mechanical separation between the plates has been constructed and experimentally characterised to verify the functionality of the proposed metasurface device.

Wave detection This part includes Chapter 3, and it introduces a compact method for terahertz wave detection at room temperature and pressure, while significantly reducing transduction losses. An antenna-coupled monolithic detector approach is utilised to design the device. The device has been fabricated and experimentally measured, confirming its functionality.

Wave analysis This part comprises Chapters 4 and 5, and it discusses methods to utilise compact metasurfaces for wave analysis. Chapter 4 adopts the quantised phase-gradient beam deflection transmitarray technique, along with a 3D-printed focusing lens, in an integrated packaging to transform a terahertz camera into a spectrometer. This system has been designed and investigated using numerical simulation. Chapter 5 leverages the idea of a frequency-diverse system integrated with a machine-learning model to design an instantaneous frequency estimation system. This system has been experimentally validated to enable frequency estimation.

6.2 Outlook

The compact and practical approaches for terahertz wave engineering using metasurfaces presented in this thesis pave a crucial pathway in advancing terahertz applications. Yet, to accelerate the deployment of the myriad applications of terahertz waves require more similar techniques and research. Building upon the approaches utilised in this

thesis, several overarching research areas need to be looked into. As a complement to the thesis, this Section discusses a few of those research areas.

Multiphysics co-design for application-oriented optimisation Most devices presented in this thesis are solely based on the electromagnetic aspect. However, in real-world applications, several other factors may play a significant role and need to be addressed. Such factors include surrounding noise, temperature, and other environmental conditions. Future research may further exploit multiphysics co-design strategies to jointly optimise these domains for various conditions. This can be achieved through a comprehensive evaluation of noise, stability, long-term drift, and environmental sensitivity to validate performance under realistic operating conditions.

Bandwidth enhancement All works demonstrated in this thesis are primarily constrained for use within the WR-3.4 band, which holds great relevance in terahertz communications, detection, and imaging. However, enhancing the bandwidth would further improve applicability in wideband sensing and spectroscopic systems. Bandwidth can be enhanced through engineered multi-resonant or broadband designs, which demand for further research efforts.

Dynamic functionality The metasurface-based devices presented in this thesis, except for the device in Chapter 2, are entirely passive, thereby limiting them to static functionality once fabricated. Dynamically reconfigurable terahertz devices are gaining interest for adaptive applications in communications and sensing. Many avenues to achieve reconfigurability include mechanical, electrical, or thermal tuning that enables real-time functional reconfiguration, while maintaining high efficiency and performance. Such avenues are worth further investigation.

Wave analysis and applications The wave engineering techniques demonstrated in this thesis also provide opportunities for a wide range of terahertz applications. Precise control of terahertz wave amplitude, phase, polarisation, and propagation may enable compact systems for computational imaging, spectroscopy, high-speed wireless communications, and non-destructive testing. Furthermore, combining metasurface-based wave manipulation with machine learning and computational sensing techniques may facilitate intelligent terahertz systems capable of real-time detection, classification, and environmental monitoring. Continued research in these areas could further broaden the practical impact of terahertz technologies and enable emerging functionalities in holography, cryptography, and other advanced terahertz systems.

6.3 Concluding remarks

In conclusion, this thesis has successfully achieved its main aim of developing and demonstrating compact and passive metasurfaces for terahertz wave manipulation, detection, and analysis, especially for the WR-3.4 band. The devices were designed by applying physics-based modelling approach, followed by numerical simulation, fabrication, and experimental validation. The functional devices demonstrated in this thesis include a reconfigurable wave manipulation structure, a room-temperature terahertz detector, and metasurface-enabled frequency analysis and spectrometer devices. The key contributions of this thesis are to provide compact, passive, and scalable architectures that can effectively address key challenges associated with terahertz technology. Overall, the outcomes of the works in this thesis contribute to the advancement of the myriad applications of the terahertz spectrum, and provide a pathway toward integrated, high-performance terahertz communications, sensing, and imaging systems.

Appendix A

Bolometer Material Selection

A comparison of the electrical, thermal, and mechanical properties of candidate absorber materials is presented in Table A.1. The material selection is guided by several key requirements of the proposed LDV-compatible monolithic MEMS terahertz bolometer such as efficient dissipative terahertz absorption and Joule heating, high thermomechanical sensitivity, mechanical robustness, sufficient elastic compliance for measurable vibration amplitudes, fabrication compatibility, and adequate optical reflectivity for LDV readout. The material properties relevant to these key design requirements are discussed below.

Thermal conductivity

Thermal conductivity determines the balance between temperature rise and thermal response speed. Very high thermal conductivity rapidly dissipates absorbed heat, reducing temperature rise and consequently lowering thermomechanical responsivity. Conversely, extremely low thermal conductivity improves thermal isolation but may significantly increase thermal time constants.

For this work, materials with thermal conductivity between 20–150 $W{\cdot}m^{-1}{\cdot}K^{-1}$ are considered usable, with 40–80 $W{\cdot}m^{-1}{\cdot}K^{-1}$ providing the most favourable compromise between thermal confinement and response speed. Gold (318 $W{\cdot}m^{-1}{\cdot}K^{-1}$) and aluminium (237 $W{\cdot}m^{-1}{\cdot}K^{-1}$) dissipate heat too efficiently, limiting temperature rise. NbN (10–20 $W{\cdot}m^{-1}{\cdot}K^{-1}$) and VO_2 (4–6 $W{\cdot}m^{-1}{\cdot}K^{-1}$) offer excellent thermal confinement

Table A.1. Comparison of candidate absorber materials. Comparison of electrical, thermal, and mechanical properties of candidate absorber materials considered for the proposed terahertz bolometer.

Material	Resistivity ($\mu\Omega \cdot$ cm)	Thermal Conductivity ($W \cdot m^{-1} \cdot K^{-1}$)	Young's Modulus (GPa)	Thermal Expansion ($\times 10^{-6}\ K^{-1}$)	Density ($g \cdot cm^{-3}$)
Nb	15–25	54	105	7.2	8.5
NbN	100–300	10–20	250–350	2–5	8.4
TiN	20–100	20–30	250–500	7–9	5.4
NiCr	100–150	11–15	∼200	13–16	8.4
Ni	∼7	∼90	∼200	∼13	8.9
Au	2.4	318	70–80	14	19.3
Al	2.7	237	∼70	23	2.7
Pt	∼10	∼70	160–170	8.8	21.4
Doped Si	10^4–10^6	100–150	130–190	2.6	2.33
Poly-Si	10^3–10^5	20–100	140–170	2.6–3	2.33
VO_2 (metallic state)	100–1000	4–6	∼140	∼5	4.6

but may lead to slower thermal response. Niobium, with a thermal conductivity of approximately 54 $W \cdot m^{-1} \cdot K^{-1}$, lies within the optimum range.

Electrical resistivity

Electrical resistivity influences the balance between resonant current generation and Joule heating. Extremely low resistivity materials exhibit strong induced currents but dissipate relatively little power as heat, while excessively high resistivity reduces current flow and weakens electromagnetic coupling.

For resonant metallic absorbers operating in the terahertz regime, a moderate resistivity range of approximately 10–100 $\mu\Omega \cdot$ cm is desirable. Gold and aluminium possess very low resistivities and therefore provide limited intrinsic dissipative loss. Doped silicon, polysilicon, and VO_2 exhibit excessively high resistivities for efficient metallic resonator operation. Niobium (15–25 $\mu\Omega \cdot$ cm) and TiN (20–100 $\mu\Omega \cdot$ cm) fall within the preferred range, while NbN and NiCr are positioned toward the higher end.

Young's modulus

Young's modulus governs the mechanical stiffness of the suspended structure. A high modulus improves structural stability and resistance to deformation but reduces thermally induced displacement and vibration amplitude. A low modulus increases vibration amplitude but may compromise structural integrity.

For MEMS bolometers employing resonance-frequency-based readout, a modulus between approximately 80–150 GPa provides an excellent compromise between robustness and thermomechanical sensitivity. NbN and TiN exhibit very high stiffness (>250 GPa), which may suppress thermally induced mechanical responses. Gold and aluminium possess relatively low stiffness (∼70 GPa), which may reduce mechanical stability. Niobium, with a modulus of approximately 105 GPa, lies close to the centre of the preferred range.

Thermal expansion coefficient

The thermal expansion coefficient directly influences thermally induced stress generation and resonance frequency shifts. Larger coefficients generally increase thermomechanical responsivity; however, excessively large values can lead to increased residual stress, warping, drift, or reliability issues.

A coefficient between approximately 5–10 $\times$ 10^{-6} K^{-1} is considered desirable. Doped silicon and polysilicon exhibit relatively low thermal expansion coefficients (∼2.6–3 $\times$ 10^{-6} K^{-1}), limiting thermomechanical actuation. Aluminium exhibits a very large value (∼23$\times$$10^{-6}$ K^{-1}), which may introduce excessive thermal stress. Niobium (7.2 $\times$ 10^{-6} K^{-1}), TiN (7–9 $\times$ 10^{-6} K^{-1}), and platinum (8.8 $\times$ 10^{-6} K^{-1}) fall within the preferred range.

Density

Density influences inertial mass loading and resonance frequency. Higher-density materials increase structural mass, lowering resonance frequency and potentially reducing sensitivity. Extremely low-density materials may exhibit reduced mechanical robustness.

Materials with densities between approximately 3–10 $g \cdot cm^{-3}$ provide a reasonable compromise. Gold (19.3 $g \cdot cm^{-3}$) and platinum (21.4 $g \cdot cm^{-3}$) introduce significant mass loading, while aluminium (2.7 $g \cdot cm^{-3}$) lies below the preferred range. Niobium (8.5 $g \cdot cm^{-3}$), TiN (5.4 $g \cdot cm^{-3}$), NbN (8.4 $g \cdot cm^{-3}$), and VO_2 (4.6 $g \cdot cm^{-3}$) fall within the desirable range.

Overall material selection

Considering all electrical, thermal, and mechanical requirements simultaneously, several materials can be excluded. Gold and aluminium possess excessively high thermal conductivity and extremely low resistivity, resulting in poor thermal confinement and limited Joule heating. Doped silicon, polysilicon, and VO_2 exhibit excessively high resistivity for efficient metallic resonator operation. NbN and TiN provide favourable thermal and electrical characteristics but possess very high Young's moduli, leading to significantly stiffer structures and reduced thermomechanical sensitivity. Platinum suffers from excessive density and mass loading.

Among the remaining candidates, both nickel and niobium provide a balanced combination of resistivity, thermal conductivity, thermal expansion coefficient, and density. However, niobium offers a more favourable Young's modulus of approximately 105 GPa, which lies within the optimum range for achieving both mechanical robustness and thermomechanical sensitivity. In addition, niobium exhibits excellent fabrication maturity in MEMS processing and sufficient optical reflectivity for LDV measurements. Consequently, niobium was selected as the absorber material for the proposed terahertz bolometer, providing the most balanced compromise between terahertz absorption, thermal response, mechanical performance, and readout sensitivity.

Appendix B

Calibration of INO MICROXCAM-384i Terahertz Camera

As discussed in Section 5.3.2, the significant accuracy drop in the 290–300 GHz range and nearby frequencies, as shown in Figure 5.3(b), is primarily due to the reduced sensitivity of the terahertz camera within this specific spectral region. This is confirmed using a separate calibration test, by illuminating terahertz waves directly onto the terahertz camera through the $f/0.7$ lens, without the presence of the metasurface. A total of 221 reference images are captured from 220–330 GHz at 0.5 GHz intervals. A representative subset of 100 images, sampled from 225 GHz to 324 GHz at 1 GHz intervals, is shown in Figure B.1, which clearly illustrates that the images around 290–300 GHz are nearly identical and closely resemble the camera's dark/reference frame, confirming the system's reduced sensitivity in that range.

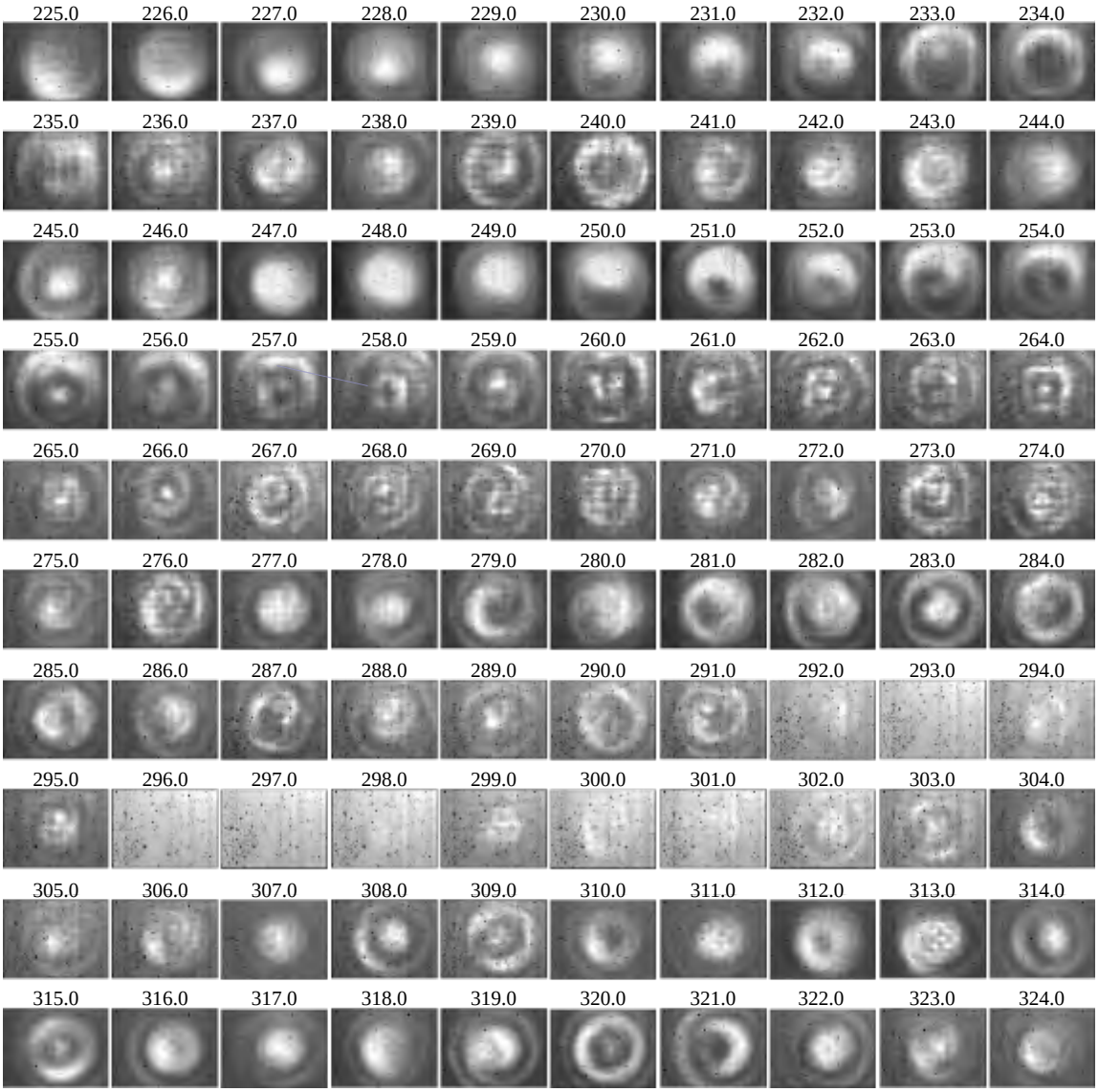

Figure B.1. Terahertz camera calibration. Raw intensity images captured using the WR-3.4 source and the terahertz camera equipped with an $f/0.7$ lens, without the metasurface, to characterise the native response of the detection system.

Bibliography

ABBOTT-D., AND ZHANG-X.-C. (2007). Special issue on T-ray imaging, sensing, and retection, *Proceedings of the IEEE*, **95**(8), pp. 1509–1513.

AKO-R. T., LEE-W. S., BHASKARAN-M., SRIRAM-S., AND WITHAYACHUMNANKUL-W. (2019). Broadband and wide-angle reflective linear polarization converter for terahertz waves, *APL Photonics*, **4**(9), art. no. 096104.

AKO-R. T., LEE-W. S. L., ATAKARAMIANS-S., BHASKARAN-M., SRIRAM-S., AND WITHAYACHUMNANKUL-W. (2020a). Ultra-wideband tri-layer transmissive linear polarization converter for terahertz waves, *APL Photonics*, **5**(4), art. no. 046101.

AKO-R. T., UPADHYAY-A., WITHAYACHUMNANKUL-W., BHASKARAN-M., AND SRIRAM-S. (2020b). Dielectrics for terahertz metasurfaces: Material selection and fabrication techniques, *Advanced Optical Materials*, **8**(3), art. no. 1900750.

AKYILDIZ-I. F., HAN-C., HU-Z., NIE-S., AND JORNET-J. M. (2022). Terahertz band communication: An old problem revisited and research directions for the next decade, *IEEE Transactions on Communications*, **70**(6), pp. 4250–4285.

AL-NAIB-I., AND WITHAYACHUMNANKUL-W. (2017). Recent progress in terahertz metasurfaces, *Journal of Infrared, Millimeter, and Terahertz Waves*, **38**(9), pp. 1067–1084.

ARABHAVI-A. M., CIABATTINI-F., HAMZELOUI-S., FLÜCKIGER-R., SARANOVAC-T., HAN-D., MARTI-D., BONOMO-G., CHAUDHARY-R., OSTINELLI-O., AND BOLOGNESI-C. R. (2022). InP/GaAsSb double heterojunction bipolar transistor emitter-fin technology with $f_{\max} = 1.2$ THz, *IEEE Transactions on Electron Devices*, **69**(4), pp. 2122–2129.

ARBABI-A., ARBABI-E., HORIE-Y., KAMALI-S. M., AND FARAON-A. (2017). Planar metasurface retroreflector, *Nature Photonics*, **11**(7), pp. 415–420.

ASADA-M., AND SUZUKI-S. (2021). Terahertz emitter using resonant-tunneling diode and applications, *Sensors*, **21**(4), art. no. 1384.

BANERJEE-D., VON SPIEGEL-W., THOMSON-M. D., SCHABEL-S., AND ROSKOS-H. G. (2008). Diagnosing water content in paper by terahertz radiation, *Optics Express*, **16**(12), pp. 9060–9066.

BAXTER-J. B., AND GUGLIETTA-G. W. (2011). Terahertz spectroscopy, *Analytical Chemistry*, **83**(12), pp. 4342–4368.

BELACEL-C., TODOROV-Y., BARBIERI-S., GACEMI-D., FAVERO-I., AND SIRTORI-C. (2017). Optomechanical terahertz detection with single meta-atom resonator, *Nature Communications*, **8**(1), art. no. 1578.

BHATTACHARYA-S., AND LI-S.-S. (2019). A fully differential SOI-MEMS thermal piezoresistive ring oscillator in liquid environment intended for mass sensing, *IEEE Sensors Journal*, **19**(17), pp. 7261–7268.

BIELECKI-Z., MIKOLAJCZYK-J., AND WOJTAS-J. (2024). A review of thermal detectors of THz radiation operated at room temperature, *Sensors*, **24**(21), art. no. 6784.

BOWLING-L., WANG-A., PHILIPS-N., RIFFE-W., MATEJCZYK-D., SKELTON-J., HOPKINS-P., FITZ-GERALD-J., AND AGNEW-S. R. (2024). Thermophysical modeling of niobium alloys informs materials selection and design for high-temperature applications, *Materials & Design*, **248**, art. no. 113456.

BOŽANIĆ-M., AND SINHA-S. (2019). Emerging transistor technologies capable of terahertz amplification: A way to re-engineer terahertz radar sensors, *Sensors*, **19**(11), art. no. 2454.

BURFORD-N. M., AND EL-SHENAWEE-M. O. (2017). Review of terahertz photoconductive antenna technology, *Optical Engineering*, **56**(1), art. no. 010901.

BUSCH-S. F., WEIDENBACH-M., BALZER-J. C., AND KOCH-M. (2016). THz optics 3D printed with TOPAS, *Journal of Infrared, Millimeter, and Terahertz Waves*, **37**(4), pp. 303–307.

BYCHOK-A., ZORENKO-O., SOBOLIEV-D., AND VOLKOV-Y. (2024). Research on ways to create THz pulse generators based on silicon IMPATT diodes, *Radioelectronics and Communications Systems*, **67**(3), pp. 149–156.

CHANG-C.-C., ZHAO-Z., LI-D., TAYLOR-A. J., FAN-S., AND CHEN-H.-T. (2019). Broadband linear-to-circular polarization conversion enabled by birefringent off-resonance reflective metasurfaces, *Physical Review Letters*, **123**(23), art. no. 237401.

CHENG-X., LI-C., FANG-B., HONG-Z., JIN-Y., AND JING-X. (2024). Metasurface-based wireless communication technology and its applications, *Journal of Applied Physics*, **135**(12), art. no. 120702.

CHENG-Y., GONG-R., AND WU-L. (2017). Ultra-broadband linear polarization conversion via diode-like asymmetric transmission with composite metamaterial for terahertz waves, *Plasmonics*, **12**, pp. 1113–1120.

CHENG-Y., QIAO-L., ZHU-D., WANG-Y., AND ZHAO-Z. (2021). Passive polarimetric imaging of millimeter and terahertz waves for personnel security screening, *Optics Letters*, **46**(6), pp. 1233–1236.

CHENG-Y., WANG-Y., NIU-Y., AND ZHAO-Z. (2020). Concealed object enhancement using multi-polarization information for passive millimeter and terahertz wave security screening, *Optics Express*, **28**(5), pp. 6350–6366.

CHENG-Y. Z., WITHAYACHUMNANKUL-W., UPADHYAY-A., HEADLAND-D., NIE-Y., GONG-R. Z., BHASKARAN-M., SRIRAM-S., AND ABBOTT-D. (2014). Ultrabroadband reflective polarization convertor for terahertz waves, *Applied Physics Letters*, **105**(18), art. no. 181111.

CHEN-H.-T., PADILLA-W. J., ZIDE-J. M., GOSSARD-A. C., TAYLOR-A. J., AND AVERITT-R. D. (2006). Active terahertz metamaterial devices, *Nature*, **444**(7119), pp. 597–600.

CHEN-S., BI-J.-D., DING-G., WANG-S., AND LUO-X.-Y. (2023). Design of polarization-insensitive polarization converter based on frequency selective surface, *Optics Communications*, **530**, art. no. 129127.

CHEN-Z., GONG-Y., DONG-H., NOTAKE-T., AND MINAMIDE-H. (2013). Terahertz achromatic quarter wave plate: Design, fabrication, and characterization, *Optics Communications*, **311**, pp. 1–5.

CHEN-Z., LI-Z., IQBAL-M. A., ARIF-N., XING-C., QI-L., AND ZENG-Y.-J. (2025). Research advances and perspectives on terahertz detection based on 2D materials, *Advanced Physics Research*, **4**(2), art. no. 2400094.

CHEON-H., YANG-H., AND SON-J. (2017). Toward clinical cancer imaging using terahertz spectroscopy, *IEEE Journal of Selected Topics in Quantum Electronics*, **23**(4), pp. 1–9.

CHEREDNICHENKO-S., HAMMAR-A., BEVILACQUA-S., DRAKINSKIY-V., STAKE-J., AND KALABUKHOV-A. (2011). A room temperature bolometer for terahertz coherent and incoherent detection, *IEEE Transactions on Terahertz Science and Technology*, **1**(2), pp. 395–402.

CHU-C.-C., DEY-S., LIU-T.-Y., CHEN-C.-C., AND LI-S.-S. (2017). Thermal-piezoresistive SOI-MEMS oscillators based on a fully differential mechanically coupled resonator array for mass sensing applications, *Journal of Microelectromechanical Systems*, **27**(1), pp. 59–72.

CHUNG-B., HEADLAND-D., AND WITHAYACHUMNANKUL-W. (2024). Terahertz imaging with 3D-printed Risley-prism and telecentric objective, *IEEE Transactions on Terahertz Science and Technology*, **14**(4), pp. 446–454.

CISCO. (2017). Cisco Visual Networking Index: Forecast and Methodology, 2016–2021, *CISCO*.

CLARK-J. R., HSU-W.-T., ABDELMONEUM-M. A., AND NGUYEN-C.-C. (2005). High-Q UHF micromechanical radial-contour mode disk resonators, *Journal of Microelectromechanical Systems*, **14**(6), pp. 1298–1310.

CONG-L., CAO-W., ZHANG-X., TIAN-Z., GU-J., SINGH-R., HAN-J., AND ZHANG-W. (2013). A perfect metamaterial polarization rotator, *Applied Physics Letters*, **103**(17), art. no. 171107.

CONG-L., XU-N., GU-J., SINGH-R., HAN-J., AND ZHANG-W. (2014). Highly flexible broadband terahertz metamaterial quarter-wave plate, *Laser & Photonics Reviews*, **8**(4), pp. 626–632.

CUNNINGHAM-P. D., VALDES-N. N., VALLEJO-F. A., HAYDEN-L. M., POLISHAK-B., ZHOU-X.-H., LUO-J., JEN-A. K.-Y., WILLIAMS-J. C., AND TWIEG-R. J. (2011). Broadband terahertz characterization of the refractive index and absorption of some important polymeric and organic electro-optic materials, *Journal of Applied Physics*, **109**(4), art. no. 043505.

DEGL'INNOCENTI-R., LIN-H., AND NAVARRO-CÍA-M. (2022). Recent progress in terahertz metamaterial modulators, *Nanophotonics*, **11**(8), pp. 1485–1514.

DIAZ-ALBARRAN-L., LUGO-HERNANDEZ-E., RAMIREZ-GARCIA-E., ENCISO-AGUILAR-M., VALDEZ-PEREZ-D., CERECEDA-COMPANY-P., GRANADOS-D., AND

COSTA-KRÄMER-J. (2018). Development and characterization of cyclic olefin copolymer thin films and their dielectric characteristics as CPW substrate by means of Terahertz Time Domain Spectroscopy, *Microelectronic Engineering*, **191**, pp. 84–90.

DO-H., CHO-S., PARK-J., SONG-H.-J., LEE-N., AND LOZANO-A. (2021). Terahertz line-of-sight MIMO communication: Theory and practical challenges, *IEEE Communications Magazine*, **59**(3), pp. 104–109.

DOVELOS-K., MATTHAIOU-M., NGO-H. Q., AND BELLALTA-B. (2021). Channel estimation and hybrid combining for wideband terahertz massive MIMO systems, *IEEE Journal on Selected Areas in Communications*, **39**(6), pp. 1604–1620.

EISELE-H., AND HADDAD-G. I. (1998). Two-terminal millimeter-wave sources, *IEEE Transactions on Microwave Theory and Techniques*, **46**(6), pp. 739–746.

EULER-M., FUSCO-V., CAHILL-R., AND DICKIE-R. (2010). 325 GHz single layer sub-millimeter wave FSS based split slot ring linear to circular polarization convertor, *IEEE Transactions on Antennas and Propagation*, **58**(7), pp. 2457–2459.

FAN-S., JEONG-K., WALLACE-V. P., AND AMAN-Z. (2019). Use of terahertz waves to monitor moisture content in high-pressure natural gas pipelines, *Energy & Fuels*, **33**(9), pp. 8026–8031.

FEDERICI-J. F., SCHULKIN-B., HUANG-F., GARY-D., BARAT-R., OLIVEIRA-F., AND ZIMDARS-D. (2005). THz imaging and sensing for security applications—explosives, weapons and drugs, *Semiconductor Science and Technology*, **20**(7), pp. S266–S280.

FISCHER-B., HOFFMANN-M., HELM-H., MODJESCH-G., AND JEPSEN-P. U. (2005). Chemical recognition in terahertz time-domain spectroscopy and imaging, *Semiconductor Science and Technology*, **20**(7), art. no. S246.

FROBERGER-K., WALTER-B., LAVANCIER-M., PERETTI-R., DUCOURNAU-G., LAMPIN-J.-F., FAUCHER-M., AND BARBIERI-S. (2022). SOI-based micro-mechanical terahertz detector operating at room-temperature and atmospheric pressure, *Applied Physics Letters*, **120**(26), art. no. 261103.

FU-X., YANG-F., LIU-C., WU-X., AND CUI-T. J. (2020). Terahertz beam steering technologies: From phased arrays to field-programmable metasurfaces, *Advanced Optical Materials*, **8**(3), art. no. 1900628.

GEORGE-D. K., AND MARKELZ-A. G. (2013). *Terahertz Spectroscopy of Liquids and Biomolecules*, Springer Berlin Heidelberg, Berlin, Heidelberg, pp. 229–250.

GOKHALE-V. J., AND RAIS-ZADEH-M. (2013). Uncooled infrared detectors using gallium nitride on silicon micromechanical resonators, *Journal of Microelectromechanical Systems*, **23**(4), pp. 803–810.

GOU-J., ZHANG-T., WANG-J., AND JIANG-Y. (2017). Spiral antenna-coupled microbridge structures for THz application, *Nanoscale Research Letters*, **12**, art. no. 91.

GRADY-N. K., HEYES-J. E., CHOWDHURY-D. R., ZENG-Y., REITEN-M. T., AZAD-A. K., TAYLOR-A. J., DALVIT-D. A., AND CHEN-H.-T. (2013). Terahertz metamaterials for linear polarization conversion and anomalous refraction, *Science*, **340**(6138), pp. 1304–1307.

HAN-Z., OHNO-S., TOKIZANE-Y., NAWATA-K., NOTAKE-T., TAKIDA-Y., AND MINAMIDE-H. (2018). Off-resonance and in-resonance metamaterial design for a high-transmission terahertz-wave quarter-wave plate, *Optics Letters*, **43**(12), pp. 2977–2980.

HASHIMSHONY-D., GELTNER-I., COHEN-G., AVITZOUR-Y., ZIGLER-A., AND SMITH-C. (2001). Characterization of the electrical properties and thickness of thin epitaxial semiconductor layers by THz reflection spectroscopy, *Journal of Applied Physics*, **90**(11), pp. 5778–5781.

HEADLAND-D., MONNAI-Y., ABBOTT-D., FUMEAUX-C., AND WITHAYACHUMNANKUL-W. (2018). Tutorial: Terahertz beamforming, from concepts to realizations, *APL Photonics*, **3**(5), art. no. 051101.

HEADLAND-D., ZATTA-R., HILLGER-P., AND PFEIFFER-U. R. (2020). Terahertz spectroscope using CMOS camera and dispersive optics, *IEEE Transactions on Terahertz Science and Technology*, **10**(5), pp. 513–523.

HE-K., ZHANG-X., REN-S., AND SUN-J. (2016). Deep residual learning for image recognition, *Proceedings of the IEEE Conference on Computer Vision and Pattern Recognition*, pp. 770–778.

HERNANDEZ-CARDOSO-G., ROJAS-LANDEROS-S., ALFARO-GOMEZ-M., HERNANDEZ-SERRANO-A., SALAS-GUTIERREZ-I., LEMUS-BEDOLLA-E., CASTILLO-GUZMAN-A., LOPEZ-LEMUS-H., AND CASTRO-CAMUS-E. (2017). Terahertz imaging for early

screening of diabetic foot syndrome: A proof of concept, *Scientific Reports*, **7**, art. no. 42124.

HONG-X., FENG-S., GUO-H., AND LI-C. (2019). A beam deflector with dielectric metasurfaces in the terahertz region, *Laser Physics*, **30**(1), art. no. 016204.

HSU-W.-T., CLARK-J. R., AND NGUYEN-C.-C. (2001). A sub-micron capacitive gap process for multiple-metal-electrode lateral micromechanical resonators, *Technical Digest. MEMS 2001. 14th IEEE International Conference on Micro Electro Mechanical Systems*, IEEE, pp. 349–352.

HUANG-X., YANG-H., YU-S., WANG-J., LI-M., AND YE-Q. (2013). Triple-band polarization-insensitive wide-angle ultra-thin planar spiral metamaterial absorber, *Journal of Applied Physics*, **113**(21), art. no. 213516.

IEEE 802 LAN/MAN STANDARDS COMMITTEE. (2017). IEEE Standard for High Data Rate Wireless Multi-Media Networks–Amendment 2: 100 Gb/s Wireless Switched Point-to-Point Physical Layer, *IEEE Std 802.15.3d-2017 (Amendment to IEEE Std 802.15.3-2016 as amended by IEEE Std 802.15.3e-2017)*, pp. 1–55.

IEEE 802 LAN/MAN STANDARDS COMMITTEE. (2024). IEEE Standard for Wireless Multimedia Networks, *IEEE Std 802.15.3-2023 (Revision of IEEE Std 802.15.3-2016)*, pp. 1–684.

IMANI-M. F., GOLLUB-J. N., YURDUSEVEN-O., DIEBOLD-A. V., BOYARSKY-M., FROMENTEZE-T., PULIDO-MANCERA-L., SLEASMAN-T., AND SMITH-D. R. (2020). Review of metasurface antennas for computational microwave imaging, *IEEE Transactions on Antennas and Propagation*, **68**(3), pp. 1860–1875.

INSTITUT NATIONAL D'OPTIQUE (INO). (2023). MICROXCAM-384i Terahertz Camera Datasheet.

ISHIBASHI-T., AND ITO-H. (2021). Uni-traveling carrier photodiodes: Development and prospects, *IEEE Journal of Selected Topics in Quantum Electronics*, **28**(2: Optical Detectors), pp. 1–6.

ITO-H., NAKAJIMA-F., OHNO-T., FURUTA-T., NAGATSUMA-T., AND ISHIBASHI-T. (2008). InP-based planar-antenna-integrated Schottky-barrier diode for millimeter- and sub-millimeter-wave detection, *Japanese Journal of Applied Physics*, **47**(8R), art. no. 6256.

JACKSON-J. B., BOWEN-J., WALKER-G., LABAUNE-J., MOUROU-G., MENU-M., AND FUKUNAGA-K. (2011). A survey of terahertz applications in cultural heritage conservation science, *IEEE Transactions on Terahertz Science and Technology*, **1**(1), pp. 220–231.

JEPSEN-P. U., COOKE-D. G., AND KOCH-M. (2011). Terahertz spectroscopy and imaging–modern techniques and applications, *Laser & Photonics Reviews*, **5**(1), pp. 124–166.

JIA-R., GAO-Y., XU-Q., FENG-X., WANG-Q., GU-J., TIAN-Z., OUYANG-C., HAN-J., AND ZHANG-W. (2021). Achromatic dielectric metasurface with linear phase gradient in the terahertz domain, *Advanced Optical Materials*, **9**(2), art. no. 2001403.

JI-W., CHANG-J., MIRZAEI-B., RIDDER-M., JELLEMA-W., KAO-T.-Y., LEE-A., GAO-J. R., URBACH-H. P., AND ADAM-A. J. (2025). Compact metasurface terahertz spectrometer, *Laser & Photonics Reviews*, **19**(3), art. no. 2401290.

JI-Y.-Y., FAN-F., WANG-X.-H., AND CHANG-S.-J. (2018). Broadband controllable terahertz quarter-wave plate based on graphene gratings with liquid crystals, *Optics Express*, **26**(10), pp. 12852–12862.

JORNET-J. M., ELAYAN-H., NAGATSUMA-T., JUNTTI-M., PINTO-E. T., KÜRNER-T., GUERBOUKHA-H., MITTLEMAN-D. M., AND KNIGHTLY-E. (2024). Mobile terahertz communication and sensing systems: A future look, *IEEE Vehicular Technology Magazine*, **19**(4), pp. 20–35.

KHALID-A., DUNN-G. M., MACPHERSON-R. F., THOMS-S., MACINTYRE-D., LI-C., STEER-M. J., PAPAGEORGIOU-V., THAYNE-I. G., KUBALL-M., OXLEY-C. H., MONTES BAJO-M., STEPHEN-A., GLOVER-J., AND CUMMING-D. R. S. (2014). Terahertz oscillations in an $In_{0.53}Ga_{0.47}As$ submicron planar Gunn diode, *Journal of Applied Physics*, **115**(11), art. no. 114502.

KHANAM-R., AND HUSSAIN-M. (2024). YOLOv11: An overview of the key architectural enhancements, *arXiv preprint arXiv:2410.17725*.

KOENIG-S., LOPEZ-DIAZ-D., ANTES-J., BOES-F., HENNEBERGER-R., LEUTHER-A., TESSMANN-A., SCHMOGROW-R., HILLERKUSS-D., PALMER-R., ZWICK-T., KOOS-C., FREUDE-W., AMBACHER-O., LEUTHOLD-J., AND KALLFASS-I. (2013). Wireless sub-THz communication system with high data rate, *Nature Photonics*, **7**(12), pp. 977–981.

KO-J. H., YOO-Y. J., LEE-Y., JEONG-H.-H., AND SONG-Y. M. (2022). A review of tunable photonics: Optically active materials and applications from visible to terahertz, *IScience*, **25**(8), art. no. 104727.

LEE-W. S., AKO-R. T., LOW-M. X., BHASKARAN-M., SRIRAM-S., FUMEAUX-C., AND WITHAYACHUMNANKUL-W. (2018). Dielectric-resonator metasurfaces for broadband terahertz quarter-and half-wave mirrors, *Optics Express*, **26**(11), pp. 14392–14406.

LEE-W. S. L. (2018). *Terahertz Metasurfaces for Wideband Polarisation Control*, PhD thesis, The University of Adelaide.

LI-C., ZHANG-Y., AND HIRAKAWA-K. (2023a). Terahertz detectors using microelectromechanical system resonators, *Sensors*, **23**(13), art. no. 5938.

LI-J., CHEN-J., YAN-D., FAN-F., CHEN-K., ZHONG-K., WANG-Y., TIAN-Z., AND XU-D. (2024a). A review: Active tunable terahertz metamaterials, *Advanced Photonics Research*, **5**(7), art. no. 2300351.

LI-M. S., ABDULLAH-M., HE-J., WANG-K., FUMEAUX-C., AND WITHAYACHUMNANKUL-W. (2024b). Frequency-diverse antenna with convolutional neural networks for direction-of-arrival estimation in terahertz communications, *IEEE Transactions on Terahertz Science and Technology*, **14**(3), pp. 354–363.

LI-M. S., AKO-R. T., SRIRAM-S., FUMEAUX-C., AND WITHAYACHUMNANKUL-W. (2023b). Terahertz planar cavity antenna based on effective medium for wireless communications, *IEEE Transactions on Terahertz Science and Technology*, **14**(2), pp. 248–257.

LIN-C.-M., CHEN-Y.-Y., FELMETSGER-V. V., SENESKY-D. G., AND PISANO-A. P. (2012). AlN/3C–SiC composite plate enabling high-frequency and high-Q micromechanical resonators, *Advanced Materials*, **24**(20), pp. 2722–2727.

LI-R., LI-C., LI-H., WU-S., AND FANG-G. (2018). Study of automatic detection of concealed targets in passive terahertz images for intelligent security screening, *IEEE Transactions on Terahertz Science and Technology*, **9**(2), pp. 165–176.

LIU-J., CHOMET-B., BEOLETTO-P., GACEMI-D., PANTZAS-K., BEAUDOIN-G., SAGNES-I., VASANELLI-A., SIRTORI-C., AND TODOROV-Y. (2022). Ultrafast detection of terahertz radiation with miniaturized optomechanical resonator driven by dielectric driving force, *ACS Photonics*, **9**(5), pp. 1541–1546.

LIU-Y., FLAVIIS-F. D., AND ALEXOPOULOS-N. G. (2008). A thin X-band microwave absorber using a center shorted spiral medium, *IEEE Antennas and Wireless Propagation Letters*, **8**, pp. 271–274.

LIU-Y.-Q., DAI-W., SUN-J., ZHANG-Y.-Y., AND DU-C.-H. (2025). An ultrahigh numerical aperture microwave metalens with ultrathin thickness, *IEEE Antennas and Wireless Propagation Letters*, **24**(9), pp. 3064–3068.

LI-X., SHEN-Z., TAN-Q., AND HU-W. (2021). High efficient metadevices for terahertz beam shaping, *Frontiers in Physics*, **9**, art. no. 659747.

LUO-Z., TANG-R., XIE-G., REN-Y., LIU-D., ZHOU-K., MIAO-W., ZHANG-W., AND SHI-S. (2026). Terahertz spectroscopy with compact apochromatic metasurface optics, *Applied Physics Letters*, **128**(1), art. no. 011701.

LV-X., AKO-R. T., BHASKARAN-M., SRIRAM-S., FUMEAUX-C., AND WITHAYACHUMNANKUL-W. (2022). Frequency-selective-surface-based mechanically reconfigurable terahertz bandpass filter, *IEEE Transactions on Terahertz Science and Technology*, **12**(3), pp. 257–266.

MACPHERSON-E., GALLERANO-G. P., PARK-G.-S., HINTZSCHE-H., AND WILMINK-G. J. (2013). Guest editorial: Terahertz imaging and spectroscopy for biology and biomedicine, *IEEE Journal of Biomedical and Health Informatics*, **17**(4), pp. 765–767.

MAEKAWA-T., KANAYA-H., SUZUKI-S., AND ASADA-M. (2016). Oscillation up to 1.92 THz in resonant tunneling diode by reduced conduction loss, *Applied Physics Express*, **9**(2), art. no. 024101.

MAESTROJUAN-I., PALACIOS-I., EDERRA-I., AND GONZALO-R. (2015). USE of COC substrates for millimeter-wave devices, *Microwave and Optical Technology Letters*, **57**(2), pp. 371–377.

MAHMOUD-A. M., AND ENGHETA-N. (2014). Wave–matter interactions in epsilon-and-mu-near-zero structures, *Nature Communications*, **5**(1), art. no. 5638.

MASSON-J.-B., AND GALLOT-G. (2006). Terahertz achromatic quarter-wave plate, *Optics Letters*, **31**(2), pp. 265–267.

MAVRONA-E., GRAF-J., HACK-E., AND ZOLLIKER-P. (2021). Optimized 3D printing of THz waveguides with cyclic olefin copolymer, *Optical Materials Express*, **11**(8), pp. 2495–2504.

MCMASTER-W. H. (1954). Polarization and the Stokes parameters, *American Journal of Physics*, **22**(6), pp. 351–362.

MEI-X., YOSHIDA-W., LANGE-M., LEE-J., ZHOU-J., LIU-P.-H., LEONG-K., ZAMORA-A., PADILLA-J., SARKOZY-S., LAI-R., AND DEAL-W. (2015). First demonstration of amplification at 1 THz using 25-nm InP high electron mobility transistor process, *IEEE Electron Device Letters*, **36**(4), pp. 327–329.

MENLO SYSTEMS. (2020). Fibre-coupled terahertz time-domain spectroscopy system (THz-TDS) TERA K15, https://www.menlosystems.com/products/thz-time-domain-solutions/terak15-terahertz-spectrometer/.

MILES-R. E., ZHANG-X.-C., EISELE-H., AND KROTKUS-A. (2007). *Terahertz Frequency Detection and Identification of Materials and Objects*, Springer Science & Business Media.

MITTLEMAN-D. M. (2018). Twenty years of terahertz imaging, *Optics Express*, **26**(8), pp. 9417–9431.

MOTAHARIFAR-E., PIERCE-R., ISLAM-R., HENDERSON-R., HSU-J., AND LEE-M. (2018). Broadband terahertz refraction index dispersion and loss of polymeric dielectric substrate and packaging materials, *Journal of Infrared, Millimeter, and Terahertz Waves*, **39**, pp. 93–104.

MURALT-P., LEDERMANN-N., PABOROWSKI-J., BARZEGAR-A., GENTIL-S., BELGACEM-B., PETITGRAND-S., BOSSEBOEUF-A., AND SETTER-N. (2005). Piezoelectric micromachined ultrasonic transducers based on PZT thin films, *IEEE Transactions on Ultrasonics, Ferroelectrics, and Frequency Control*, **52**(12), pp. 2276–2288.

NAFTALY-M., AND MILES-R. E. (2007). Terahertz time-domain spectroscopy for material characterization, *Proceedings of the IEEE*, **95**(8), pp. 1658–1665.

NAGATSUMA-T., DUCOURNAU-G., AND RENAUD-C. C. (2016). Advances in terahertz communications accelerated by photonics, *Nature Photonics*, **10**(6), pp. 371–379.

NAGATSUMA-T., SONG-H.-J., FUJIMOTO-Y., MIYAKE-K., HIRATA-A., AJITO-K., WAKATSUKI-A., FURUTA-T., KUKUTSU-N., AND KADO-Y. (2009). Giga-bit wireless link using 300–400 GHz bands, *2009 International Topical Meeting on Microwave Photonics*, IEEE, pp. 1–4.

NAING-T. L., ROCHELEAU-T. O., ALON-E., AND NGUYEN-C. T.-C. (2020). Low-power MEMS-based pierce oscillator using a 61-MHz capacitive-gap disk resonator, *IEEE Transactions on Ultrasonics, Ferroelectrics, and Frequency Control*, **67**(7), pp. 1377–1391.

NIELSEN-K., RASMUSSEN-H. K., ADAM-A. J., PLANKEN-P. C., BANG-O., AND JEPSEN-P. U. (2009). Bendable, low-loss topas fibers for the terahertz frequency range, *Optics Express*, **17**(10), pp. 8592–8601.

NIU-Y., WANG-Y., WU-W., WEN-J., CHENG-Y., CHEN-M., JIANG-S., WU-D., AND ZHAO-Z. (2020). Efficient room-temperature terahertz detection via bolometric and photothermoelectric effects in $EuBiTe_3$ crystal, *Optical Materials Express*, **10**(4), pp. 952–961.

NOUMAN-M. T., HWANG-J. H., AND JANG-J.-H. (2016). Ultrathin terahertz quarter-wave plate based on split ring resonator and wire grating hybrid metasurface, *Scientific Reports*, **6**(1), art. no. 39062.

PAN-X., CAI-Z., CHEN-Z., DING-Y., ZHENG-Z., AND DING-F. (2025). Recent progress in mechanically reconfigurable metasurfaces, *APL Photonics*, **10**(8), art. no. 080901.

PAVANELLO-F., GARET-F., KUPPAM-M.-B., PEYTAVIT-E., VANWOLLEGHEM-M., VAURETTE-F., COUTAZ-J.-L., AND LAMPIN-J.-F. (2013). Broadband ultra-low-loss mesh filters on flexible cyclic olefin copolymer films for terahertz applications, *Applied Physics Letters*, **102**(11), art. no. 111114.

PENDRY-J. B., HOLDEN-A. J., ROBBINS-D. J., AND STEWART-W. J. (1999). Magnetism from conductors and enhanced nonlinear phenomena, *IEEE Transactions on Microwave Theory and Techniques*, **47**(11), pp. 2075–2084.

PENDRY-J. B., HOLDEN-A., ROBBINS-D., AND STEWART-W. (1998). Low frequency plasmons in thin-wire structures, *Journal of Physics: Condensed Matter*, **10**(22), art. no. 4785.

PENG-Y., LIU-J., FU-J., LUO-Y., ZHAO-X., AND WEI-X. (2025). Emerging thermal detectors based on low-dimensional materials: Strategies and progress, *Nanomaterials*, **15**(6), art. no. 459.

PFEIFFER-C., AND GRBIC-A. (2014). Bianisotropic metasurfaces for optimal polarization control: Analysis and synthesis, *Physical Review Applied*, **2**(4), art. no. 044011.

PICKWELL-E., AND WALLACE-V. (2006). Biomedical applications of terahertz technology, *Journal of Physics D: Applied Physics*, **39**(17), art. no. R301.

PILLER-M., LUHMANN-N., CHIEN-M.-H., AND SCHMID-S. (2019). Nanoelectromechanical infrared detector, *Optical Sensing, Imaging, and Photon Counting: From X-Rays to THz 2019*, Vol. 11088, SPIE, pp. 9–15.

PLUSQUELLIC-D. F., SIEGRIST-K., HEILWEIL-E. J., AND ESENTURK-O. (2007). Applications of terahertz spectroscopy in biosystems, *ChemPhysChem*, **8**(17), pp. 2412–2431.

QUADER-S., ABDULLAH-M., HE-E., FUMEAUX-C., AND WITHAYACHUMNANKUL-W. (2025). 3D-printed frequency-diverse metasurface for camera-based terahertz frequency analyzer, *IEEE Microwave and Wireless Technology Letters*, **35**(12), pp. 2105–2108.

QUADER-S., AKO-R. T., SRIRAM-S., FUMEAUX-C., AND WITHAYACHUMNANKUL-W. (2024a). Mechanically reconfigurable polarization converter for terahertz waves, *IEEE Transactions on Terahertz Science and Technology*, **14**(4), pp. 502–509.

QUADER-S., AKRAM-M. R., XIAO-F., AND ZHU-W. (2020a). Graphene based ultra-broadband terahertz metamaterial absorber with dual-band tunability, *Journal of Optics*, **22**(9), art. no. 095104.

QUADER-S., FUMEAUX-C., AND WITHAYACHUMNANKUL-W. (2024b). Antenna-coupled micro-electromechanical bolometer for terahertz detection, *2024 IEEE Asia-Pacific Microwave Conference (APMC)*, IEEE, Bali, Indonesia, pp. 802–804.

QUADER-S., FUMEAUX-C., AND WITHAYACHUMNANKUL-W. (2026). Antenna-coupled terahertz electromechanical bolometer, *APL Engineering Physics*, **1**(1), art. no. 016104.

QUADER-S., LV-X., YOU-X., AKO-R. T., BHASKARAN-M., SRIRAM-S., FUMEAUX-C., AND WITHAYACHUMNANKUL-W. (2024c). Mechanically reconfigurable terahertz quasi-optical components for spectral filtering and polarization control, *2024 IEEE Microwaves, Antennas, and Propagation Conference (MAPCON)*, IEEE, pp. 1–4.

QUADER-S., ZHANG-J., AKRAM-M. R., AND ZHU-W. (2020b). Graphene-based high-efficiency broadband tunable linear-to-circular polarization converter for terahertz waves, *IEEE Journal of Selected Topics in Quantum Electronics*, **26**(5), pp. 1–8.

RAHAFROOZ-A., AND POURKAMALI-S. (2012). Thermal-piezoresistive energy pumps in micromechanical resonant structures, *IEEE Transactions on Electron Devices*, **59**(12), pp. 3587–3593.

RAHM-M., LI-J.-S., AND PADILLA-W. J. (2013). THz wave modulators: A brief review on different modulation techniques, *Journal of Infrared, Millimeter, and Terahertz Waves*, **34**(1), pp. 1–27.

REESE-M., SANTAVICCA-D., PROBER-D., TRUE-A., AND SCHMUTTENMAER-C. (2007). Niobium direct detectors for fast and sensitive terahertz spectroscopy, *Review of Scientific Instruments*, **78**(8), art. no. 086111.

RISACHER-C., GÜSTEN-R., STUTZKI-J., HÜBERS-H.-W., BELL-A., BUCHBENDER-C., BÜCHEL-D., CSENGERI-T., GRAF-U., HEYMINCK-S., HIGGINS-R. D., HONINGH-C. E., JACOBS-K., KLEIN-B., OKADA-Y., PARIKKA-A., PÜTZ-P., REYES-N., RICKEN-O., RIQUELME-D., SIMON-R., AND WIESEMEYER-H. (2016). The upGREAT 1.9 THz multi-pixel high resolution spectrometer for the SOFIA Observatory, *Astronomy & Astrophysics*, **595**, art. no. A34.

ROGALSKI-A., AND SIZOV-F. (2011). Terahertz detectors and focal plane arrays, *Opto-electronics Review*, **19**(3), pp. 346–404.

SADEGHI-P., TANZER-M., LUHMANN-N., PILLER-M., CHIEN-M.-H., AND SCHMID-S. (2020). Thermal transport and frequency response of localized modes on low-stress nanomechanical silicon nitride drums featuring a phononic-band-gap structure, *Physical Review Applied*, **14**(2), art. no. 024068.

SAIFULLAH-Y., HE-Y., BOAG-A., YANG-G.-M., AND XU-F. (2022). Recent progress in reconfigurable and intelligent metasurfaces: A comprehensive review of tuning mechanisms, hardware designs, and applications, *Advanced Science*, **9**(33), art. no. 2203747.

SCHELLER-M. (2011). Real-time terahertz material characterization by numerical three-dimensional optimization, *Optics Express*, **19**(11), pp. 10647–10655.

SCHURIG-D., MOCK-J. J., JUSTICE-B., CUMMER-S. A., PENDRY-J. B., STARR-A. F., AND SMITH-D. R. (2006). Metamaterial electromagnetic cloak at microwave frequencies, *Science*, **314**(5801), pp. 977–980.

SEDRA-A. S., SEDRA-D. E. A. S., SMITH-K. C., AND SMITH-K. C. (1998). *Microelectronic Circuits*, New York: Oxford University Press.

SEIDI-M.-R., GOHARI-M. M., MADANNEJAD-A., SHAH-U., AND OBERHAMMER-J. (2025). Silicon-micromachined wideband sub-THz frequency-diverse antenna, *IEEE Transactions on Terahertz Science and Technology*, **15**(3), pp. 456–463.

SHEHATA-M., WANG-K., AND WITHAYACHUMNANKUL-W. (2023). Carrierless amplitude and phase modulation for terahertz communications, *IEEE Journal of Selected Topics in Quantum Electronics*, **29**(5: Terahertz Photonics), pp. 1–14.

SHELBY-R. A., SMITH-D. R., AND SCHULTZ-S. (2001). Experimental verification of a negative index of refraction, *Science*, **292**(5514), pp. 77–79.

SHEN-Y.-C. (2011). Terahertz pulsed spectroscopy and imaging for pharmaceutical applications: A review, *International Journal of Pharmaceutics*, **417**(1-2), pp. 48–60.

SHEN-Y. C., LO-T., TADAY-P. F., COLE-B. E., TRIBE-W. R., AND KEMP-M. C. (2005). Detection and identification of explosives using terahertz pulsed spectroscopic imaging, *Applied Physics Letters*, **86**(24), art. no. 241116.

SHI-J., WANG-Y., CHEN-T., XU-D., ZHAO-H., CHEN-L., YAN-C., TANG-L., HE-Y., FENG-H., AND YAO-J. (2018). Automatic evaluation of traumatic brain injury based on terahertz imaging with machine learning, *Optics Express*, **26**(5), pp. 6371–6381.

SHIN-H. J., KIM-S.-H., PARK-K., LIM-M.-C., CHOI-S.-W., AND OK-G. (2017). Free-standing guided-mode resonance humidity sensor in terahertz, *Sensors and Actuators A: Physical*, **268**, pp. 27 – 31.

SHIRI-Y., GUERBOUKHA-H., AND MITTLEMAN-D. M. (2023). Terahertz beam steering with curved metasurfaces, *Journal of Infrared, Millimeter, and Terahertz Waves*, **44**(5), pp. 397–406.

SIEGEL-P. H. (2002). Terahertz technology, *IEEE Transactions on Microwave Theory and Techniques*, **50**(3), pp. 910–928.

SINGH-R., CAO-W., AL-NAIB-I., CONG-L., WITHAYACHUMNANKUL-W., AND ZHANG-W. (2014). Ultrasensitive terahertz sensing with high-Q Fano resonances in metasurfaces, *Applied Physics Letters*, **105**(17), art. no. 171101.

SIZOV-F., AND ROGALSKI-A. (2010). THz detectors, *Progress in Quantum Electronics*, **34**(5), pp. 278–347.

SMITH-D. R., AND KROLL-N. (2000). Negative refractive index in left-handed materials, *Physical Review Letters*, **85**(14), art. no. 2933.

SONG-H.-J., AJITO-K., MURAMOTO-Y., WAKATSUKI-A., NAGATSUMA-T., AND KUKUTSU-N. (2012). 24 Gbit/s data transmission in 300 GHz band for future terahertz communications, *Electronics Letters*, **48**(15), pp. 953–954.

SONG-H.-J., AND LEE-N. (2021). Terahertz communications: Challenges in the next decade, *IEEE Transactions on Terahertz Science and Technology*, **12**(2), pp. 105–117.

SONG-H.-J., AND NAGATSUMA-T. (2011). Present and future of terahertz communications, *IEEE Transactions on Terahertz Science and Technology*, **1**(1), pp. 256–263.

SONG-H.-J., KIM-J.-Y., AJITO-K., KUKUTSU-N., AND YAITA-M. (2014). 50-Gb/s direct conversion QPSK modulator and demodulator MMICs for terahertz communications at 300 GHz, *IEEE Transactions on Microwave Theory and Techniques*, **62**(3), pp. 600–609.

STEPHEN LI-M., TANYI AKO-R., SRIRAM-S., FUMEAUX-C., AND WITHAYACHUMNANKUL-W. (2023). Terahertz metasurface for near-field beam conversion, *Optics Letters*, **48**(8), pp. 2202–2205.

SUN-J., AND ZHOU-J. (2025). Metamaterials: The art in materials science, *Engineering*, **44**, pp. 145–161.

SU-X., OUYANG-C., XU-N., CAO-W., WEI-X., SONG-G., GU-J., TIAN-Z., O'HARA-J. F., HAN-J., AND ZHANG-W. (2015). Active metasurface terahertz deflector with phase discontinuities, *Optics Express*, **23**(21), pp. 27152–27158.

TAMAYAMA-Y., YASUI-K., NAKANISHI-T., AND KITANO-M. (2014). A linear-to-circular polarization converter with half transmission and half reflection using a single-layered metamaterial, *Applied Physics Letters*, **105**(2), art. no. 021110.

TANIGUCHI-A., BAKX-T. J. L. C., BASELMANS-J. J. A., HUITING-R., KARATSU-K., LLOMBART-N., RYBAK-M., TAKEKOSHI-T., TAMURA-Y., AKAMATSU-H., BRACKENHOFF-S., BUENO-J., BUIJTENDORP-B. T., DABIRONEZARE-S. O., DOING-A.-K., FUJII-Y., FUJITA-K., GOUWEROK-M., HÄHNLE-S., ISHIDA-T., ISHII-S.,

KAWABE-R., KITAYAMA-T., KOHNO-K., KOUCHI-A., MAEKAWA-J., MATSUDA-K., MURUGESAN-V., NAKATSUBO-S., OSHIMA-T., PASCUAL LAGUNA-A., THOEN-D. J., VAN DER WERF-P. P., YATES-S. J. C., AND ENDO-A. (2022). DESHIMA 2.0: development of an integrated superconducting spectrometer for science-grade astronomical observations, *Journal of Low Temperature Physics*, **209**(3), pp. 278–286.

TAO-H., LANDY-N. I., BINGHAM-C. M., ZHANG-X., AVERITT-R. D., AND PADILLA-W. J. (2008). A metamaterial absorber for the terahertz regime: Design, fabrication and characterization, *Optics Express*, **16**(10), pp. 7181–7188.

TONOUCHI-M. (2007). Cutting-edge terahertz technology, *Nature Photonics*, **1**(2), pp. 97–105.

TZYDYNZHAPOV-G., GUSIKHIN-P., MURAVEV-V., DREMIN-A., NEFYODOV-Y., AND KUKUSHKIN-I. (2020). New real-time sub-terahertz security body scanner, *Journal of Infrared, Millimeter, and Terahertz Waves*, pp. 1–10.

VATANSEVER-F., AND HAMBLIN-M. R. (2012). Far infrared radiation (FIR): Its biological effects and medical applications, *Photonics & Lasers in Medicine*, **1**(4), pp. 255–266.

VICARELLI-L., TREDICUCCI-A., AND PITANTI-A. (2022). Micromechanical bolometers for subterahertz detection at room temperature, *ACS Photonics*, **9**(2), pp. 360–367.

WALKER-G. C., BOWEN-J. W., MATTHEWS-W., ROYCHOWDHURY-S., LABAUNE-J., MOUROU-G., MENU-M., HODDER-I., AND JACKSON-J. B. (2013). Sub-surface terahertz imaging through uneven surfaces: visualizing Neolithic wall paintings in Çatalhöyük, *Optics Express*, **21**(7), pp. 8126–8134.

WALLACE-V. P., MACPHERSON-E., FITZGERALD-A. J., LO-T., PROVENZANO-E., PINDER-S., AND PURUSHOTHAM-A. (2006). Terahertz pulsed imaging and spectroscopy of breast tumors, *Optical Methods in the Life Sciences*, Vol. 6386, SPIE, pp. 178–185.

WALLACE-V. P., MACPHERSON-E., ZEITLER-J. A., AND REID-C. (2008). Three-dimensional imaging of optically opaque materials using nonionizing terahertz radiation, *Journal of the Optical Society of America A*, **25**(12), pp. 3120–3133.

WANG-D., GU-Y., GONG-Y., QIU-C.-W., AND HONG-M. (2015a). An ultrathin terahertz quarter-wave plate using planar babinet-inverted metasurface, *Optics Express*, **23**(9), pp. 11114–11122.

WANG-Q., ZHANG-X., XU-Y., TIAN-Z., GU-J., YUE-W., ZHANG-S., HAN-J., AND ZHANG-W. (2015b). A broadband metasurface-based terahertz flat-lens array, *Advanced Optical Materials*, **3**(6), pp. 779–785.

WANG-S., LI-B. Z., KHABSA-M., FANG-H., AND MA-H. (2020). Linformer: Self-attention with linear complexity, *arXiv:2006.04768*.

WANG-Z., HAN-Y., XU-N., CHEN-L., LI-C., WU-L., AND ZHANG-W. (2018). Characterization of thin metal films using terahertz spectroscopy, *IEEE Transactions on Terahertz Science and Technology*, **8**(2), pp. 161–164.

WIESAUER-K., AND JÖRDENS-C. (2013). Recent advances in birefringence studies at THz frequencies, *Journal of Infrared, Millimeter, and Terahertz Waves*, **34**, pp. 663–681.

WIETZKE-S., JANSEN-C., KRUMBHOLZ-N., PETERS-O., VIEWEG-N., JÖRDENS-C., SCHELLER-M., ROMEIKE-D., JUNG-T., REUTER-M., CHATTERJEE-S., KOCH-M., PHYSIK-F., BAUDRIT-B., ZENTGRAF-T., HOCHREIN-T., AND BASTIAN-M. (2010). Terahertz spectroscopy: A powerful tool for the characterization of plastic materials, *2010 10th IEEE International Conference on Solid Dielectrics*, IEEE, pp. 1–4.

WILLIAMS-B. S. (2007). Terahertz quantum-cascade lasers, *Nature Photonics*, **1**(9), pp. 517–525.

WILLIAMS-G. P. (2005). Filling the THz gap—high power sources and applications, *Reports on Progress in Physics*, **69**(2), pp. 301–326.

WILTSE-J. C. (1984). History of millimeter and submillimeter waves, *IEEE Transactions on Microwave Theory and Techniques*, **32**(9), pp. 1118–1127.

WITHAYACHUMNANKUL-W. (2010). *Engineering Aspects of Terahertz Time-Domain Spectroscopy*, PhD thesis, The University of Adelaide, School of Electrical and Electronic Engineering.

WITHAYACHUMNANKUL-W., YAMADA-R., FUJITA-M., AND NAGATSUMA-T. (2018). All-dielectric rod antenna array for terahertz communications, *APL Photonics*, **3**(5), art. no. 051707.

WU-L., XU-D., WANG-Y., ZHANG-Y., WANG-H., LIAO-B., GONG-S., CHEN-T., WU-N., FENG-H., AND YAO-J. (2020). Horizontal-scanning attenuated total reflection terahertz imaging for biological tissues, *Neurophotonics*, **7**(2), pp. 1 – 10.

WU-Y.-M., DING-X., AND WANG-B.-Z. (2018). A dual-band broadband metamaterial absorber with wide-angle absorption and polarization insensitivity, *2018 International Conference on Microwave and Millimeter Wave Technology (ICMMT)*, pp. 1–3.

XU-C., REN-Z., WEI-J., AND LEE-C. (2022). Reconfigurable terahertz metamaterials: From fundamental principles to advanced 6G applications, *IScience*, **25**(2), art. no. 103799.

XUE-Q., JI-C., MA-S., GUO-J., XU-Y., CHEN-Q., AND ZHANG-W. (2024). A survey of beam management for mmWave and THz communications towards 6G, *IEEE Communications Surveys & Tutorials*, **26**(3), pp. 1520–1559.

YAKOVLEV-E. V., ZAYTSEV-K. I., DOLGANOVA-I. N., AND YURCHENKO-S. O. (2015). Non-destructive evaluation of polymer composite materials at the manufacturing stage using terahertz pulsed spectroscopy, *IEEE Transactions on Terahertz Science and Technology*, **5**(5), pp. 810–816.

YANG-X., ZHAO-X., YANG-K., LIU-Y., LIU-Y., FU-W., AND LUO-Y. (2016). Biomedical applications of terahertz spectroscopy and imaging, *Trends in Biotechnology*, **34**(10), pp. 810 – 824.

YEN-T.-J., PADILLA-W., FANG-N., VIER-D. C., SMITH-D. R., PENDRY-J., BASOV-D., AND ZHANG-X. (2004). Terahertz magnetic response from artificial materials, *Science*, **303**(5663), pp. 1494–1496.

YI-H., QU-S.-W., NG-K.-B., CHAN-C. H., AND BAI-X. (2015). 3-D printed millimeter-wave and terahertz lenses with fixed and frequency scanned beam, *IEEE Transactions on Antennas and Propagation*, **64**(2), pp. 442–449.

YOU-X., AKO-R. T., LEE-W. S., BHASKARAN-M., SRIRAM-S., FUMEAUX-C., AND WITHAYACHUMNANKUL-W. (2021). Terahertz transmissive half-wave metasurface with enhanced bandwidth, *Optics Letters*, **46**(17), pp. 4164–4167.

YOU-X., AKO-R. T., LEE-W. S. L., BHASKARAN-M., SRIRAM-S., FUMEAUX-C., AND WITHAYACHUMNANKUL-W. (2020). Broadband terahertz transmissive quarter-wave metasurface, *APL Photonics*, **5**(9), art. no. 096108.

YOU-X., AKO-R. T., SRIRAM-S., AND WITHAYACHUMNANKUL-W. (2025). 3D terahertz confocal imaging with chromatic metasurface, *Laser & Photonics Reviews*, **19**(7), art. no. 2401011.

YOU-X., FUMEAUX-C., AND WITHAYACHUMNANKUL-W. (2022). Tutorial on broadband transmissive metasurfaces for wavefront and polarization control of terahertz waves, *Journal of Applied Physics*, **131**(6), art. no. 061101.

YUN-J., OH-S. J., SONG-K., YOON-D., SON-H. Y., CHOI-Y., HUH-Y., AND RIEH-J. (2017). Terahertz reflection-mode biological imaging based on InP HBT source and detector, *IEEE Transactions on Terahertz Science and Technology*, **7**(3), pp. 274–283.

ZEITLER-J. A., TADAY-P. F., NEWNHAM-D. A., PEPPER-M., GORDON-K. C., AND RADES-T. (2007). Terahertz pulsed spectroscopy and imaging in the pharmaceutical setting-a review, *Journal of Pharmacy and Pharmacology*, **59**(2), pp. 209–223.

ZHANG-C., YALAVARTHI-E. K., GIROUX-M., CUI-W., STEPHAN-M., MALEKI-A., WECK-A., MÉNARD-J.-M., AND ST-GELAIS-R. (2024). High detectivity terahertz radiation sensing using frequency-noise-optimized nanomechanical resonators, *APL Photonics*, **9**(12), art. no. 0238977.

ZHANG-X., MYERS-E., SADER-J., AND ROUKES-M. (2013). Nanomechanical torsional resonators for frequency-shift infrared thermal sensing, *Nano Letters*, **13**(4), pp. 1528–1534.

ZHANG-Y., EBATA-K., IIMORI-M., LIU-Q., ZHAO-Z., TAKEUCHI-R., LI-H., MAENAKA-K., AND HIRAKAWA-K. (2025a). Uncooled, broadband terahertz bolometers using SOI MEMS beam resonators with piezoresistive readout, *Microsystems & Nanoengineering*, **11**(1), art. no. 132.

ZHANG-Y., HOSONO-S., NAGAI-N., SONG-S.-H., AND HIRAKAWA-K. (2019). Fast and sensitive bolometric terahertz detection at room temperature through thermomechanical transduction, *Journal of Applied Physics*, **125**(15), art. no. 151602.

ZHANG-Y., WATANABE-Y., HOSONO-S., NAGAI-N., AND HIRAKAWA-K. (2016). Room temperature, very sensitive thermometer using a doubly clamped microelectromechanical beam resonator, *Applied Physics Letters*, **108**(16), art. no. 163503.

ZHANG-Z., DONG-W., FANG-Z., CHEN-R., LIU-J., DENG-S., AND CHEN-M. (2025b). Terahertz metasurface with polarization conversion and Gaussian beam shaping, *Applied Optics*, **64**(22), pp. 6235–6241.

ZHAO-G., MORS-M. T., WENCKEBACH-T., AND PLANKEN-P. C. (2002). Terahertz dielectric properties of polystyrene foam, *Journal of the Optical Society of America B*, **19**(6), pp. 1476–1479.

ZHAO-H., WANG-Y., CHEN-L., SHI-J., MA-K., TANG-L., XU-D., YAO-J., FENG-H., AND CHEN-T. (2018). High-sensitivity terahertz imaging of traumatic brain injury in a rat model, *Journal of Biomedical Optics*, **23**(3), pp. 1 – 7.

ZHELUDEV-N. I., AND KIVSHAR-Y. S. (2012). From metamaterials to metadevices, *Nature Materials*, **11**(11), pp. 917–924.

ZHENG-G., MÜHLENBERND-H., KENNEY-M., LI-G., ZENTGRAF-T., AND ZHANG-S. (2015). Metasurface holograms reaching 80% efficiency, *Nature Nanotechnology*, **10**(4), pp. 308–312.

ZHU-A. Y., CHEN-W.-T., KHORASANINEJAD-M., OH-J., ZAIDI-A., MISHRA-I., DEVLIN-R. C., AND CAPASSO-F. (2017). Ultra-compact visible chiral spectrometer with meta-lenses, *APL Photonics*, **2**(3), art. no. 06103.

ZHU-H., WANG-K., LIU-G., WANG-G., MOU-J., ZHANG-W., AND WEI-G. (2022). A terahertz optomechanical detector based on metasurface and bi-material microcantilevers, *Micromachines*, **13**(5), art. no. 805.

ZI-J., LI-Y., FENG-X., XU-Q., LIU-H., ZHANG-X.-X., HAN-J., AND ZHANG-W. (2020). Dual-functional terahertz waveplate based on all-dielectric metamaterial, *Physical Review Applied*, **13**(3), art. no. 034042.

ZI-J., XU-Q., WANG-Q., TIAN-C., LI-Y., ZHANG-X., HAN-J., AND ZHANG-W. (2018). Antireflection-assisted all-dielectric terahertz metamaterial polarization converter, *Applied Physics Letters*, **113**(10), art. no. 101104.

ZUO-C., SINHA-N., AND PIAZZA-G. (2010). Very high frequency channel-select MEMS filters based on self-coupled piezoelectric AlN contour-mode resonators, *Sensors and Actuators A: Physical*, **160**(1-2), pp. 132–140.